A Study of Impurity Screening in Alcator C-Mod Plasmas

by

Ying Wang

Submitted to the Department of Physics
in partial fulfillment of the requirements for the degree of

Doctor of Philosophy

at the

MASSACHUSETTS INSTITUTE OF TECHNOLOGY

June 1996

Author . . . .
Department of Physics
May 10, 1996

Certified by . . . .
Earl Marmar
Senior Research Scientist
Thesis Supervisor

Accepted by . . . .
George Koster
Chairman, Departmental Committee on Graduate Students

A Study of Impurity Screening in Alcator C-Mod Plasmas

by

Ying Wang

Submitted to the Department of Physics
on May 10, 1996, in partial fulfillment of the
requirements for the degree of
Doctor of Philosophy

Abstract

Experiments were carried out to study the impurity screening in Alcator C-Mod. Argon was injected during these experiments and the argon density in the plasma was measured by observation of the helium-like argon spectrum using a high energy resolution x-ray spectrometer array (HIREX). The argon screening efficiency $p \equiv \frac{number\ of\ Ar\ atoms\ in\ the\ plasma}{number\ of\ Ar\ atoms\ injected}$ was found to be independent of the divertor target plate strike point locations, the outer gap and the heating mode for the L-mode/Ohmic diverted plasmas, and to be no more than weakly dependent of the plasma elongation κ for the limited plasmas. $p \propto \bar{n}_e$ for the diverted plasmas in Alcator C-Mod. p was significantly higher for limited plasmas than for diverted plasmas, due to the higher edge T_e and n_e of the diverted plasmas. During the H-mode, high impurity content was found in the core plasma, mainly due to the long impurity particle confinement time rather than the reduced impurity screening ability of the SOL.

A spatially constant diffusion coefficient and a moderate (3 m/s at the edge) inward convection velocity were used to model most of the ohmic and L-mode plasmas. But the impurity diffusion coefficient was found to be spatially variant for at least some ohmic cases. During pellet injections, a large convection velocity was found. Scandium was injected during long H-mode. Brightness profile and time history of both He-like Sc and Li-like Sc were simulated using the MIST code. It was found that the confinement improves substantially during the H-mode. D was found to drop by a factor of 2 in the inner part of the plasma and by an order of magnitude to the neoclassical level in the outer part. A large inward convection flux was also found to exist at the edge. The transport studies results suggest that the edge transport parameters change substantially during the H-mode compared to the L-mode while the central transport parameters remain at the L-mode level. This shows the importance of the edge processes to the H-mode.

Thesis Supervisor: Earl Marmar
Title: Senior Research Scientist

Acknowledgments

I would like to thank all the people involved in the completion of this thesis. Above everything, I would like to thank my advisors John and Earl for their infinite patience and invaluable help and guidance. I would like to thank my thesis reader Professor Porkolab for his invaluable support that enabled me to see the light at the end of the tunnel. And I would like to thank Garry, Brian, Francesca, JT, Bob Granetz and Martin for being so helpful whenever I have questions. Steve Horne is particularly helpful with my Linux questions. Although those questions had nothing to do with the plasma physics, they did make my resume look better.

I would like to thank my fellow graduate students, whose presence made this group a fun, albeit sometimes less scientific, place to be. I especially thank those senior students who offered much needed help on "where is the copier", "how to use this computer?" or "how do I set lower priority for my process so no one yells at me?", etc. I would like to thank Sam, Jody, Lin, Dan, Mike Graf, Artur, Dave, Maxim, Mike Koltonyuk, Paul, Peter, Jim Weaver, Darren, Jeff, Cindy, Dirk and Gerry for their friendship and help.

I also would like to thank all the scientists in the C-Mod group for graciously allowing argon to be injected during many of the runs. What would I do without the data from those piggy-backed runs?

I thank my parents, who raised and shaped me and who lent me helping hands whenever I need help.

I whole-heartedly thank my love, Ni Yan, for her understanding and support during the darkest days of my life. It was she who rekindled my hope and desire. Without her there would never be this thesis. Well, even if there would, it would be a thesis filled with much much more misery.

Contents

List of Figures

List of Tables

Chapter 1

Introduction

1.1 Thermonuclear Fusion and the Tokamak Concept

1.1.1 Thermonuclear Fusion

Nuclear fusion is the process that combines light nuclei into heavier ones and releases energy. The most common fusion reactions occur in the centers of the stars, where hydrogen is burned into helium and enormous amount of energy (the Sun releases roughly 4×10^{26} *Joule* per second) are released in the form of radiation. Almost all the energy used by mankind can be traced back to the fusion energy produced by the Sun in the past. Naturally the most important goal inspiring modern plasma physics is to explore the commercial use of nuclear fusion energy produced on Earth.

The most useful reactions for the commercial applications of nuclear fusion mainly involves two isotopes of hydrogen: deuterium (D) and tritium (T). These reactions can be expressed as :

$$D + D \rightarrow^3 He + n + 3.2 MeV , \tag{1.1}$$

$$D + D \rightarrow T + p + 4.0 MeV , \tag{1.2}$$

$$D + T \rightarrow^4 He + n + 17.6 MeV . \tag{1.3}$$
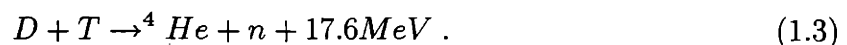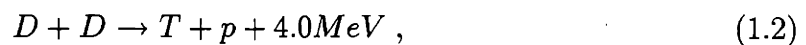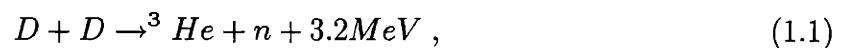
The cross sections for these fusion reactions are appreciable only for incident energies above 5 keV. Accelerated beams of deuterons bombarding targets will not produce significant levels of fusion reactions because most of the deuterons will lose their energy by scattering before undergoing any nuclear reactions. So far the only feasible way to achieve nuclear fusion is to create a plasma with thermal energy in the 10 keV range. The problems of heating and confining such a high temperature plasma are the main topics of controlled thermonuclear fusion research.

1.1.2 Tokamaks

Controlled thermonuclear fusion is of great interest because it offers a virtually inexhaustible source of energy. The prospect of generating economically significant amounts of power from controlled thermonuclear fusion has been and will continue to be the driving force behind plasma fusion research.

A systematic study of controlled thermonuclear fusion started after the Second World War, encouraged by the successful invention of the hydrogen bomb, which utilized uncontrolled thermonuclear fusion. Soviet scientists pioneered the development with the introduction of the tokamak concept. A tokamak is a toroidal containment device which features a strong toroidal magnetic field combined with the magnetic field generated by a large current flowing in the plasma. Since the 1950s, dozens of tokamaks of various sizes and complexity were built around the world.

The goal of tokamak research, and to a larger extent, the entire magnetically confined fusion research, is to discover magnetic geometries that are capable of stably confining a sufficiently high density of plasma at a sufficiently high temperature for a sufficiently long time to produce net thermonuclear power. In its most elementary form the power balance in a magnetic fusion reactor is described in terms of the Lawson parameter $n_e \tau_E$ with n_e the plasma number density and τ_E the energy confinement time. (Ref. [1]) The condition to to achieve breakeven (i.e. thermonuclear neutron power $\geq$ applied input power) is:

$$n_e \tau_E \geq 6 \times 10^{19}\ m^{-3}s\ .$$

(1.4)

1.1.3 Alcator C-Mod Tokamak

Alcator C-Mod follows a high-field high-density compact tokamak approach to plasma confinement. The name Alcator is derived from the Italian *Alto Campo Torus* meaning "high field torus", which indicates the design philosophy of the Alcator series of tokamaks. Alcator C-Mod is the third of the Alcator series of tokamaks, located in the Massachusetts Institute of Technology. Its predecessors, Alcator A and Alcator C, going into operation in 1974 and 1978 respectively, had proven that this high-field high-density approach is extremely successful in obtaining high temperature, well confined plasmas in machines of modest size and cost. In fact, Alcator C was the first magnetic confinement device to exceed the minimum value of the Lawson parameter required for energy breakeven. See Ref. [2].

Despite their successful and productive performances, Alcator A and Alcator C were traditional in design. They had circular cross-section plasmas with edges defined by a solid limiter and the level of auxiliary heating was modest, less than the normal ohmic heating power. Alcator C-Mod was originally conceived as a modification of Alcator C. It soon became clear, however, that the most effective way to achieve the aim of the experiment was to build an almost entirely new machine, while utilizing the extensive ancillary equipment available from the Alcator C program. Alcator C-Mod went into operation in 1992. It represents a major improvement over its two predecessors in both expected performance and operational flexibility. Its capability to produce highly elongated single or double null diverted plasmas offers opportunities to explore an entirely new operation mode not available in the two older Alcator machines. Divertor studies therefore represent a major research area in the Alcator C-Mod program. One of the important tasks of divertor research is to understand the impurity behavior under diverted operating condition.

Another significant improvement of Alcator C-Mod is its large auxiliary heating power. Alcator C-Mod utilizes two RF (Radio Frequency) generating units to deliver up to 4 MW of Ion Cyclotron Range of Frequency (ICRF) heating wave at 80 MHz through two antennas closely positioned to the plasma edge. Two more RF generating units are available. In the future, Alcator C-Mod offers the possibility of investigating

	Alcator A	Alcator C	Alcator C-Mod
Operating period	1974-1981	1978-1986	1992-
Major Radius (m)	0.54	0.64	0.67
Minor Radius (m)	0.1	0.16	0.22
Toroidal Field B_T (T)	8	13	5.3 (9)
Plasma Current I_p (MA)	0.4	0.8	1.2 (3)
Line average density ($10^{20}m^{-3}$)	0.1-5.0	0.1-10	0.8-4.0
Central electron temperature(keV)	2	2.5	4 (6)
Elongation κ	1.0	1.0	1.0-1.8
Flat-top duration (s)	0.5	0.5	1 (7)
Plasma cross-section	limited	limited	diverted

Table 1.1: The basic plasma design parameters of Alcator series tokamaks. Values in parentheses are for future operation.

ICRF power of up to 8 MW. This represents a significant extension of capabilities over Alcator C and A, in which only a few hundred kilowatts of ICRF power were available. The use of high auxiliary power in Alcator C-Mod requires some important questions to be answered, among which is the effect on the impurity transport or impurity source rates. It was observed in Alcator C that even small amount of RF power led to serious impurity problems. See Ref. [3]. If the results obtained there were to be extrapolated to the anticipated power planned for Alcator C-Mod , the level of impurity radiation would be prohibitive.

Table 1.1 lists the basic plasma design parameters of Alcator series of tokamaks. Figure 1-1 shows a cross section of Alcator C-Mod tokamak. Figure 1-2 shows the set of poloidal field coils used in Alcator C-Mod .

1.2 Impurities in Tokamak Plasmas

Plasma impurities play an important role in tokamaks for a number of reasons. Their presence can affect the plasma in various ways, some of which are detrimental to plasma performance and some are not.

Since the goal of fusion research is to achieve economically significant amounts of fusion power, it is of vital importance that the Lawson parameter $n_e \tau_E$ be maximized. The problem of maximizing $n_e \tau_E$ can be roughly separated into two relatively

independent parts. First, the maximum energy confinement time τ_E is determined by the microscopic behavior of the plasma: collisions and microinstabilities. In experiments, the achievable τ_E is also affected by energy lose mechanisms. Impurities play important roles in dissipating the plasma energy. Medium to high-z impurities like Mo produce strong line emission and bremsstrahlung radiation [4] from the core plasma, and therefore reduce the energy confinement time.

Second, the maximum density n_e is determined by macroscopic equilibria and stability limits set by the magnetic geometry. Low-z impurities like C and O form a radiation layer at the outer part of the plasma, which both radiates away energy and destabilizes the magnetic equilibrium, (Ref. [5] – [7]), and therefore limits the n_e achievable.

Radiation from the core plasma by medium to high-z impurities also reduces the electron temperature and reduces the possibility of fusion reactions. A fuel dilution effect caused by the existence of impurities also reduces the possibility of fusion reactions. There is a pressure limit and hence an electron density limit for a plasma with a given magnetic field due to MHD instabilities (Ref. [8]). Given the fact that the tokamak plasma is quasi-neutral and that each impurity atom contributes many more electrons than does each fuel atom, significant amounts of impurities in the core plasma would severely limit the fuel ion density achievable.

The problem that the impurities pose to tokamak operation necessitates the understanding of the behavior of various impurities, which is set by three factors; (a) the sources, (b) the sinks and (c) the transport mechanisms linking the two.

(a) **Source.** The source of the impurities is generally located at the edge of the plasma, arising from plasma-surface interactions, mostly sputtering from the limiter or the divertor plates. But for the purpose of studying impurity behavior, various impurities are also injected through pellet injection, laser ablation or gas puffing. Depending on the initial velocity of the injected particles, the impurity source is not always located at the edge of the plasma. Pellet injection, for example, may create a impurity source well within the core plasma. The impurity source can be considered

an edge effect for the main technique used in the studies in this thesis, gas puffing.

(b) **Sink.** Non-recycling impurities eventually return to the limiter or divertor plate and deposit on it. Even for recycling impurities, as in the case of argon, some of the atoms adhere to the machine surface. The rest of the recycling impurity ions neutralized on the machine surface don't stay on the wall. Instead they re-enter the plasma.

(c) **Transport** Transport mechanisms connect the impurity source and sink. They can be further divided into two parts; 1) impurity penetration processes through the Scrape-Off Layer (SOL) and edge plasma; 2) impurity diffusion processes throughout the rest of the plasma. The latter is relatively simple and has been well studied and documented. Impurity transport in the core plasma can be approximated by;

$$\Gamma = -D \nabla n + nV , \qquad (1.5)$$

where Γ is the impurity flux; D is the anomalous diffusion coefficient of the impurity; V is the convection velocity; n is the impurity density;

D has been measured by impurity injection experiments. It is found that D is the same for many impurity species with close atomic numbers. For most ohmic and L-mode plasmas, D can be approximated as a constant throughout the entire plasma, i.e. $\frac{\partial D(r)}{\partial r} \simeq 0$. See Ref. [9].

1.3   Topics of This Thesis

Much of the emphasis of this thesis is put on the study of impurity screening under various plasma conditions. Experiments dedicated to the comparison of impurity screening in diverted and limited plasma were carried out and the results for two types of impurities, argon and scandium, are presented in Section 4.2. These results prove the divertor's advantage over the limiter in reducing impurity penetration. In this section, a simple model is developed attempting to calculate theoretically the impurity density from measurable plasma parameters. Calculation of argon penetration

efficiency using this model is presented in this section. Some analysis for crosschecking the model offers qualitative support for it and are presented in Appendix D.

Argon was injected during many experiments dedicated to purposes other than impurity studies. The data from those experiments were also analyzed and presented in Chapter 4. The analysis shows that the argon penetration for the ohmic diverted plasma is nearly independent of the divertor strike point location, the outer gap and the ICRF heating. The argon penetration for the limited plasmas is also no more than weakly dependant on the plasma elongation κ, though the same conclusion cannot be drawn for the diverted plasma due to lack of experimental data. Based on the knowledge that the argon penetration is nearly independent of the parameters mentioned above, efforts were made to produce a scaling for the argon penetration as a function of the average electron density, which is the only parameter with significant influence on argon penetration of the diverted plasmas. The scaling is discussed in Section 4.7. H-mode impurity screening is also discussed in this chapter.

In the MIST (Multiple Ionization State Transport) code that is used to calculate the density profiles of ions in different charge states, the impurity diffusion coefficient is normally approximated as a constant throughout the plasma for ohmic plasmas. However, evidence suggests this may not be the case. Instead, D decreases in the outer region in at least some cases. The evidence will be presented in Chapter 5. One of the cases studied in this chapter involves pellet injection. The convective velocity is found to increase dramatically and the argon density is found to peak strongly shortly after the pellet injection.

It was first observed on the ASDEX divertor tokamak (Ref. [10]) that when sufficiently high auxiliary heating power was applied, the energy confinement time τ_E suddenly increased from the low value usually characteristic of auxiliary heated tokamaks (L-mode). During this so-called "H-mode", the particle confinement time also increase substantially, resulting impurity accumulation which may adversely affect the plasma. Therefore it is of interest to study the impurity behaviors in the H-mode plasmas. Several H-mode impurity studies were carried out on Alcator C-Mod. The MIST code was used to simulate the brightness profiles and the brightness time his-

tories of the injected impurity signals in order to find the transport coefficients that produce the best fits. The results will be presented in Chapter 5. The transport coefficients were then used to study the argon screening of the H-mode plasmas. The results will be presented in Chapter 4.

In Chapter 6, future direction of the impurity screening research is discussed. A summary of this thesis is also presented.

The appendices provide information on details of the atomic physics, instrumental calibrations and test of the impurity penetration model.
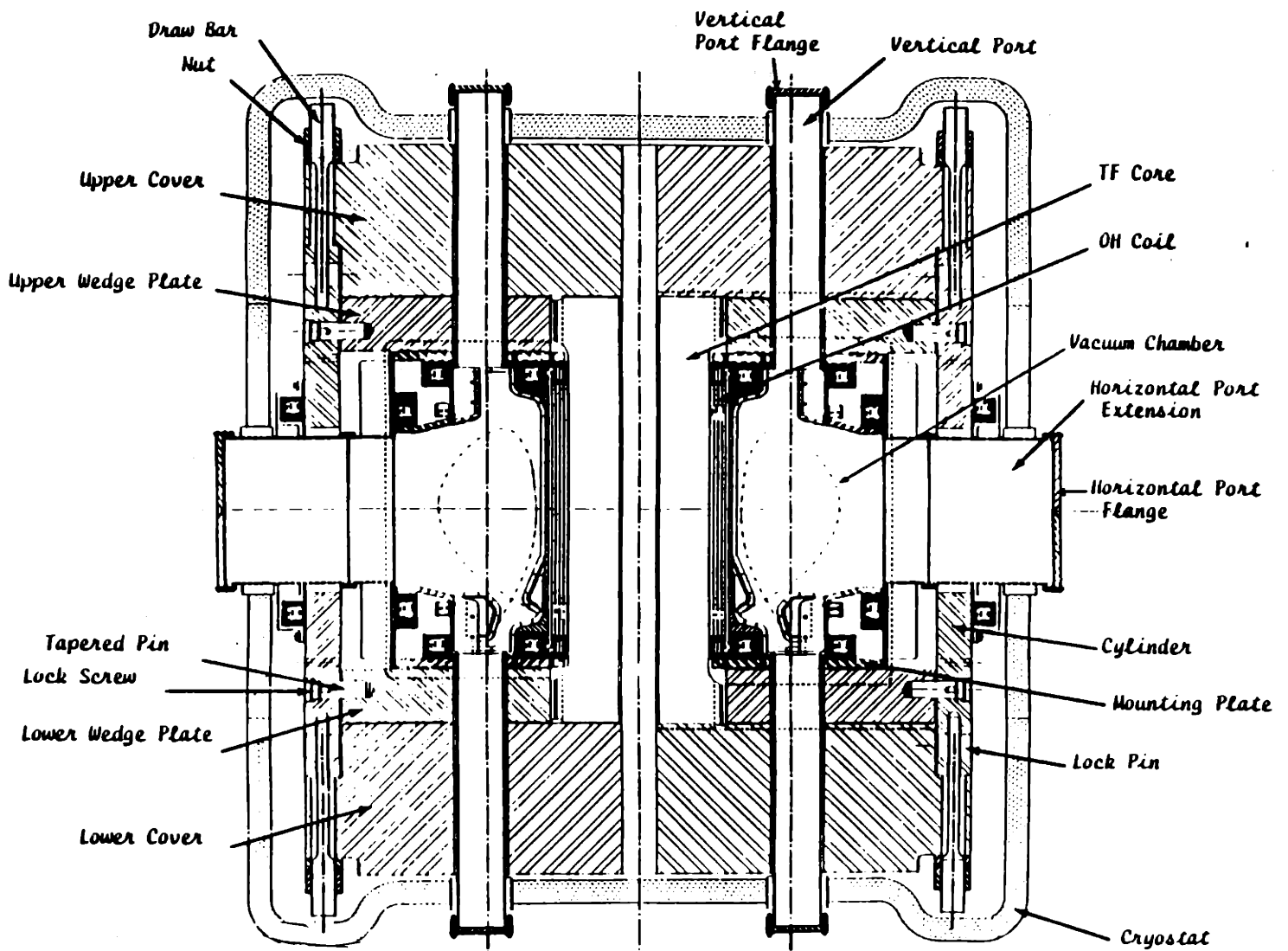
Figure 1-1: Cross-section of Alcator C-Mod tokamak. The magnetic geometry of a typical shaped plasma is also shown.
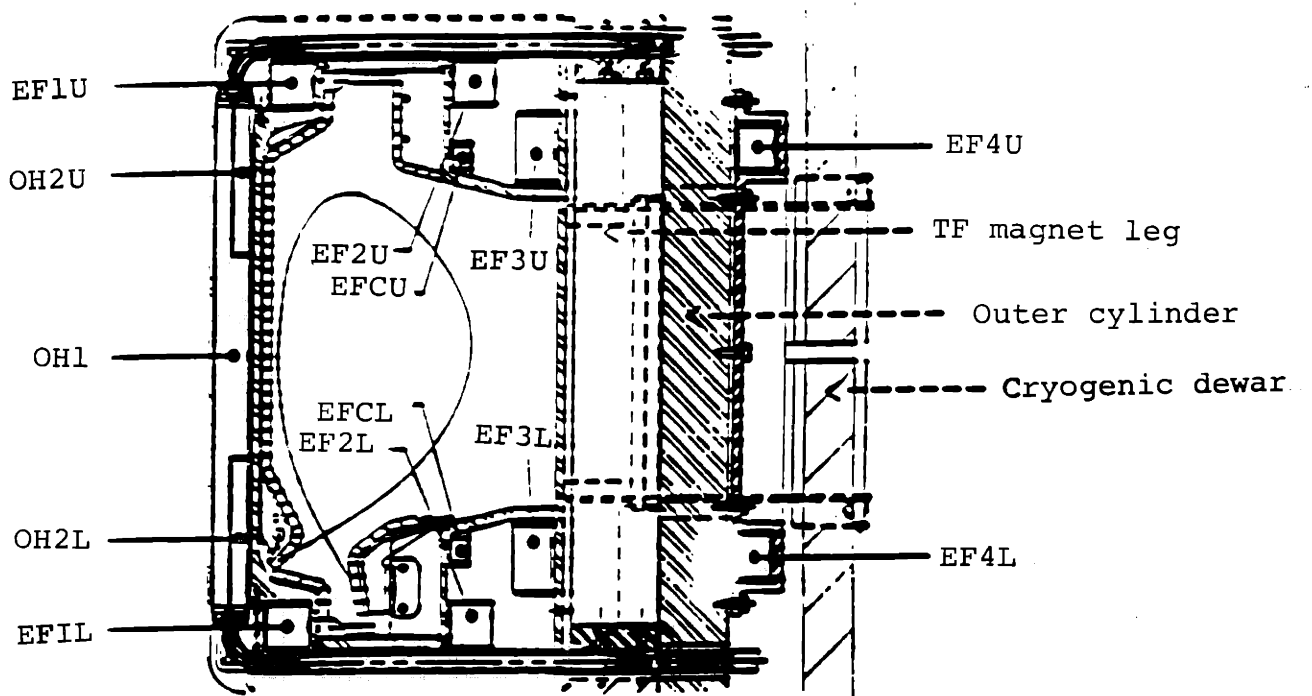
Figure 1-2: The set of poloidal field coils used in Alcator C-Mod tokamak. The details of the highly shaped divertor are also shown.

Chapter 2

Plasma Diagnostics and Experiment

2.1   Plasma Diagnostics

Various diagnostics are used to observe the tokamak plasma. Though based on a variety of physical effects, the diagnostics can be generally divided into three categories: magnetic measurements, radiation measurements and particle measurements. For the purpose of this thesis, raw data are provided by radiation measurements. Plasma parameters measured using other techniques, however, are essential to the interpretation of the radiation data.

2.1.1   Magnetic Diagnostics

The position and shape of the plasma in Alcator C-Mod are diagnosed by an extensive array of magnetic diagnostics which measure the magnetic field, magnetic flux and the plasma current at a number of discrete locations around the vacuum vessel. See Ref. [11]. The measurements are used to reconstruct the shape of the magnetic surfaces both inside and outside of the plasma. The EFIT code (Ref. [12]) is used for the reconstruction. It provides important knowledge of the magnetic geometry of the plasma.

2.1.2 Electron Temperature and Density Measurements

Electron Temperature Measurements

When electrons with high thermal energy gyrate around the magnetic field lines, they emit cyclotron emissions which is characterized by their thermal temperature. For a thermal plasma, the shape of the emission profile correspond to the shape of the temperature profile along the line of sight. On Alcator C-Mod, electron cyclotron emission (ECE Ref. [13]) diagnostic measures the radiation emission at various frequencies. The electron temperature profile can be obtained utilizing the known magnetic geometry.

Electron Density Measurements

A 10 channel Two-Color Interferometer (TCI, [14]) system is used to obtain the electron density profile used in the data analysis throughout this thesis. Each channel of the TCI provides a line-integrated measurement of the electron density along a vertical chord through the plasma. The chordal measurements are inverted using standard matrix inversion techniques to yield the electron density profile.

Fast Scanning Langmuir Probe

TCI and ECE measures electron density and temperature mainly in the core plasma. To obtain the electron density and electron temperature outside of the LCFS, a Langmuir probe array is used in Alcator C-Mod experiments. It consists a fast scanning reciprocating probe with four Langmuir probes imbedded on its tip (Ref. [15]) and 16 flush-mount Langmuir probes. The Fast Scanning Probe (FSP) provides the electron density and temperature profiles outside of the LCFS. Figure 2-1 shows the location of the Fast Scanning Probe.

2.1.3 High Energy-Resolution X-Ray Spectrometer Array

Spectrometer
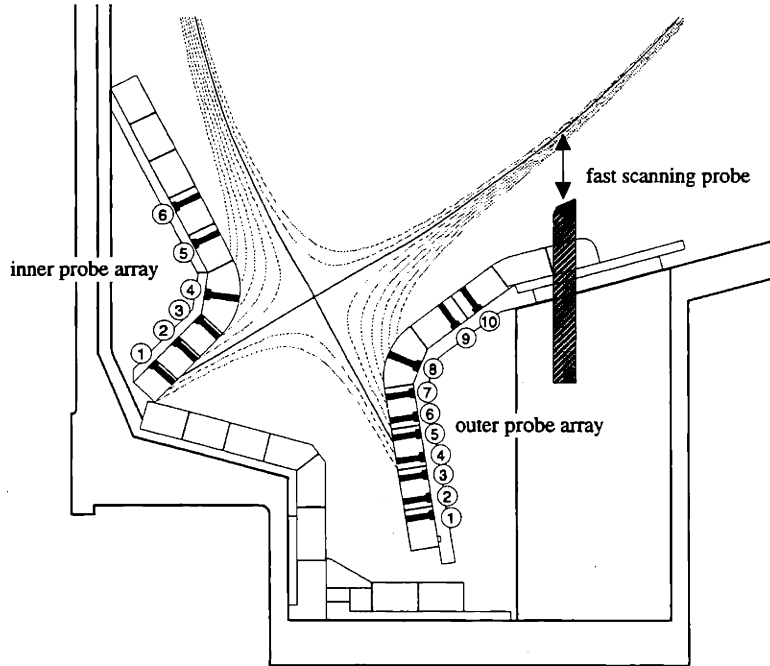
Figure 2-1: The location of the Fast Scanning Probe (FSP). Also shown are the locations of the flush-mount Langmuir probes, marked by the encircled numbers. A diverted plasma magnetic geometry is superimposed.

A five chord high resolution (resolving power 4000) x-ray spectrometer array (HIREX) is used in the Alcator C-Mod experiment, mainly for measurement of T_i but with a wide range of other applications. (Ref. [16]) For the purpose of this thesis, some of the spectrometers were viewing helium-like argon spectra so the argon density can be deduced. In order to obtain spatial profiles of the measured quantities, each spectrometer is independently scannable. The range of the five spectrometers combined covers the entire plasma region. (Figure 2-2 illustrates the scanning range of each of the spectrometers.) To achieve the required scanning ability, von Hamos geometry is used to reduce the size of the spectrometer. (Ref. [17].)

Argon ($z = 18$) is the impurity of choice for several reasons. It is chemically inert and the level is easy to control with a pulsed gas valve. For the central electron temperature of Alcator C-Mod plasmas (2 - 5 keV), the predominant charge states of argon are fully stripped, hydrogen-like and helium-like, all of which have relatively simple spectra for $\Delta n = 1$ transitions to the ground state, with the exception of the fully stripped ions, which produce no spectrum. Argon recycles from the first wall
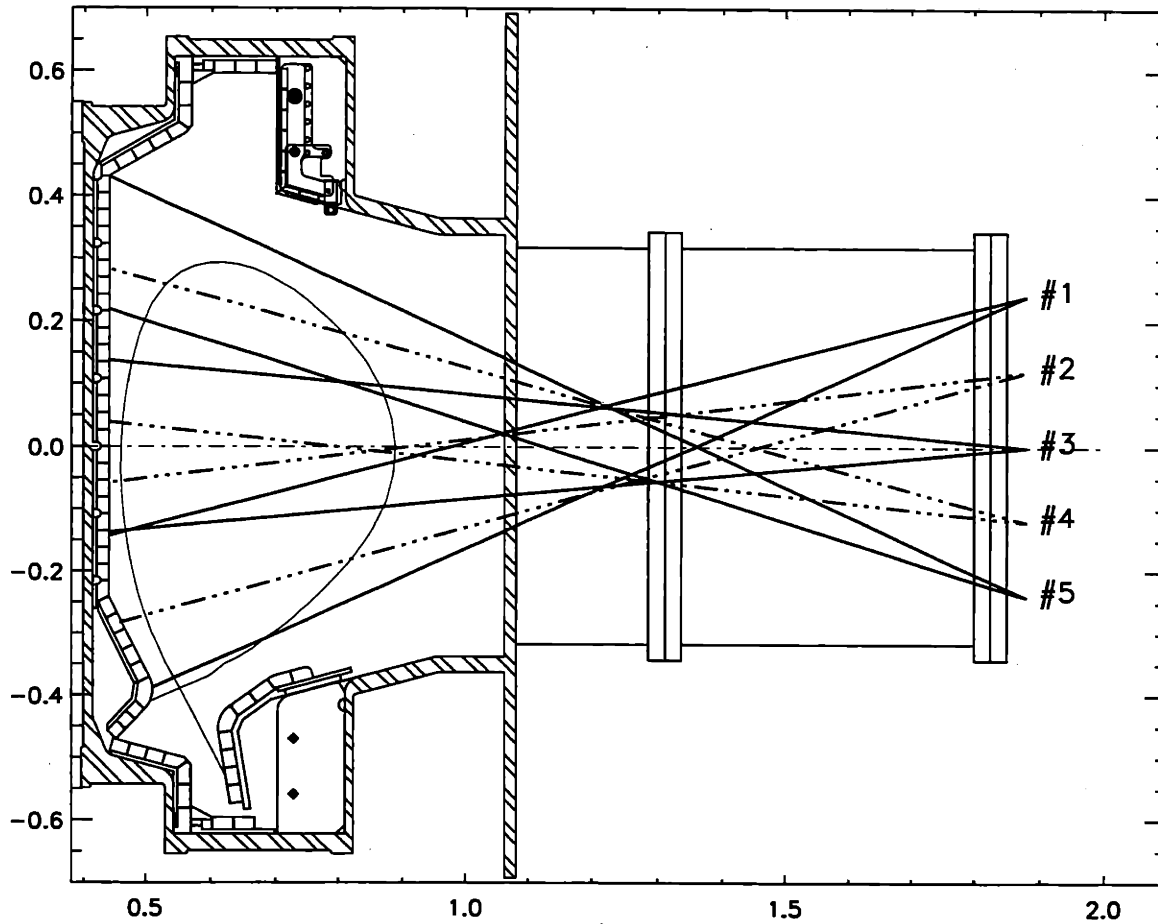
Figure 2-2: Scanning range of the X-ray spectrometer array (HIREX). An elongated diverted plasma is also shown here.

surfaces so the argon level can reach a steady state in the plasma. Also argon's atomic mass is small enough so there is adequate Doppler broadening for the ion temperature measurements to be carried out in the high resolution spectrometers.

In order to cover not only $\Delta n = 1$ hydrogen-like and helium-like argon transitions, but also high n transitions and spectra of other elements, the spectrometers have to cover a wider wavelength range (2.8 Å to 4.0 Å). Given the condition that the Bragg angle is desired to be between 20° and 40° for achieving good resolution and for convenience, the Bragg Law $n\lambda = 2d \sin \theta$ then requires that 6.22Å$< 2d <$8.18Å. The quartz $10\bar{1}1$ crystal (2d=6.687Å) fits this range and therefore is selected.

Each individual spectrometer consists of a variable width entrance slit covered with a 25μm beryllium window and a position sensitive proportional counter detector with a 75μm beryllium cover. The entrances are positioned as close as possible to viewing windows covered with 50μm beryllium foils on a flange on B-port, one of the ten equally-spaced horizontal ports in Alcator C-Mod. The detectors are filled with 60% Kr and 40% ethane at slightly above atmospheric pressure. The charges produced by collisions of x-ray photons and Kr atoms travel on a multiwire anode plane to induce image pulses on a delay line cathode plane. Those pulses travel at much lower speed than the speed of light so that the positional information along the delay line can be obtained by comparing the arrival time of the pulses at either end of the detector. See Ref. [18]

Each spectrometer consists of an entrance arm with the entrance slit and the crystal on a rotary mount which has a built-in home position for reference angle, and an exit arm to which the detector mounts. The exit arm is connected to the entrance arm by a bellows and is driven by a lead screw and a pivot mechanism which forces it to pivot at the center of the crystal axis. See Figure E-1 for a picture of the spectrometer. Also see Figure E-2 for a more detailed view of the wavelength scanning mechanism. The position of the exit arm is read from a linear variable resistor, which is attached to the exit arm, and the position is in turn converted to wavelength. Each spectrometer is mounted on a plate which pivots at the entrance slit. Actuators are used to change the plates' vertical positions so that the spectrometers can look

at various lines of sight. See Figure 2-2 for the scanning range of each individual spectrometer. The vertical positions are also read using linear variable resistors. Stepper motors provide power for both the vertical and wavelength movements. The spectrometers are evacuated by a single mechanical pump, with independent valves controlling the pumping of each individual spectrometer.

The wavelength and vertical position calibration procedures are described in Appendix A.

Electronics

High voltage is supplied to each detector at typically around 2KV. The detector has an inherent 200 ohm impedance so each one has to be connected to a 200 ohm - 50 ohm impedance matching transformer. Two fast amplifiers (each with a fixed gain of −200) and an inverter are used to amplify the signal. An attenuator is used in conjunction with the amplifiers because two amplifiers give too much gain while one gives not enough. The amplified pulses are −2V to −5V with a 2 ns rise time and a 10 ns decay time. It's very important to determine the arrival times of the pulses since the positional information along the detector is carried by them. Ideally the time the pulses reach a certain threshold can be used as the arrival time if the pulses are of the same line shape. However, for pulses with different line shapes, it takes different amount of time for the pulses to cross a certain threshold after they arrive and thus gives an incorrect arrival time measurement. To solve this problem, the amplified pulses are fed into a Constant-Fraction Discriminator (CFD). The CFD takes negative input signals and splits each input signal so that a portion of the signal is delayed and subtracted from a fraction of the undelayed signal. The resulting bipolar constant-fraction signal has a baseline crossover that is virtually independent of the input signal height. The zero crossing point is detected and used to provide precisely timed logic pulses which are subsequently sent into a Time-Digital Converter (TDC). Signal from one end of the detector is arbitrarily set to trigger the start of the TDC while the other signal , which is used to stop the TDC, undergoes 100 ns delay to ensure it wouldn't arrive before the start signal. 100 ns is adequate because

the total travel time for a pulse along the whole length of the delay line is 75 ns. The time difference between the start and stop is then dumped to a histogramming memory. The CFD also sends a logic signal to a scaler to record the time history of the total counting rate. Figure 2-3 is a diagram of the data acquisition electronics setup for a spectrometer.

The spectra are typically collected every 50 ms during a discharge and each individual spectrum has 1024 channels. The duration of each collection is mainly constrained by the amount of memory available. The more spectra are collected, the more memory is needed if the wavelength range is maintained for each spectrum. Also the shorter the collection duration, the fewer the counts per channel. For a typical discharge, 50 ms collection time provides around 50 counts per channel for the highest line for the spectrometer #5 if it's looking at around 17 cm away from the plasma center. This is about the lower limit for achieving decent statistics. So, even though HIREX is capable of collecting spectra at far less than a 50ms interval, 32 spectra at 50 ms each is a good compromise.

The detectors and cables are all shielded from radio frequency (RF) EM waves by a metal housings.

2.1.4 VUV Spectrometer

At typical operating temperatures $(2 \rightarrow 5\ eV)$ in Alcator C-Mod, much of the line emission from impurities in the plasma occurs in the VUV region of the spectrum. A high resolution, time-resolving absolutely calibrated spectrometer is used in Alcator C-Mod to monitor the wavelength region from about $50\mathring{A}$ to $1100\mathring{A}$. This device, referred to as the McPherson spectrometer after the company that supplied the basic instrument, is used as the baseline diagnostic for the characterization of impurities in the tokamak. The McPherson spectrometer is configured as a time-resolving spectrograph with finite bandwidth through the use of a microchannel plate image intensifier and a Reticon (Ref. [19]) photodiode array detector.

In Figure 2-4 a spectrum taken by the McPherson spectrometer in the wavelength range of lithium-like scandium line emission, and the brightness time history of the
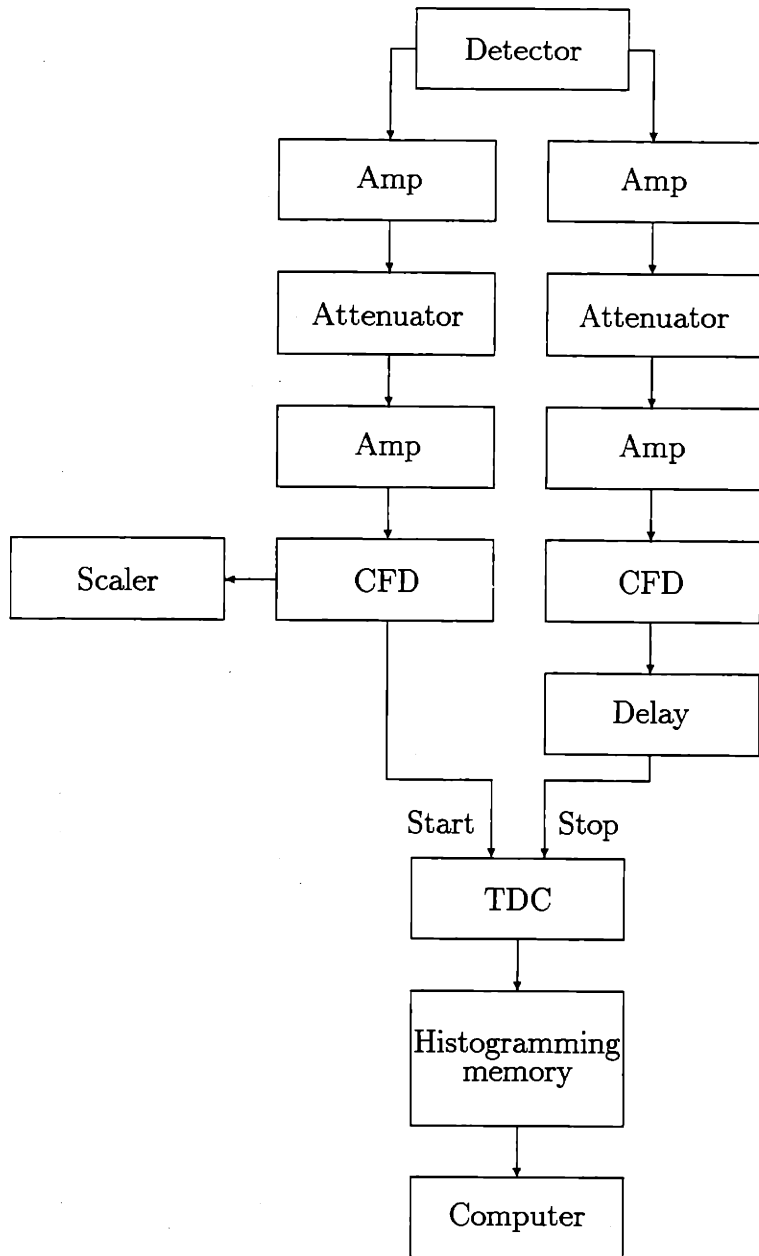
Figure 2-3: Data aquisition electronics setup on HIREX

lithium-like scandium line, is shown. The scandium is injected by a laser ablation technique, which is discussed further in Section 2.2.3.
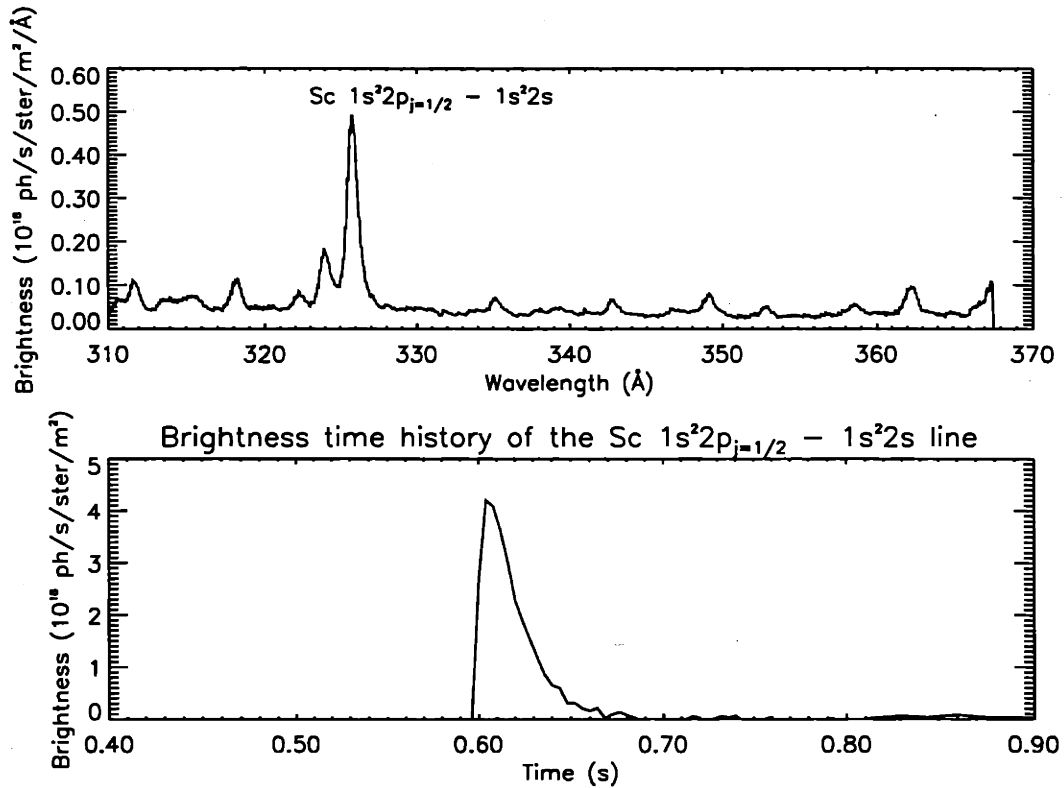
Figure 2-4: Spectrum and brightness time history of Li-like scandium line taken by the McPherson VUV spectrograph.

The most common chord viewed by this spectrometer is typically through the center of the plasma. For all the analysis involved in this thesis, only data from discharges during which McPherson spectrometer was viewing through the plasma center are used, though this spectrometer is capable of viewing chords well above and below the plasma center through a pivoting mechanism.

The McPherson spectrometer is absolutely calibrated using a soft x-ray source to wavelengths of up to $114\overset{\circ}{A}$. An extrapolation technique, using the known ratio of oscillator strengths of a set of lines spanning the range of $128\overset{\circ}{A} \rightarrow 780\overset{\circ}{A}$ which are emitted by various impurity ions, is used to extend the results of the calibration to its entire wavelength range (Ref. [20]).
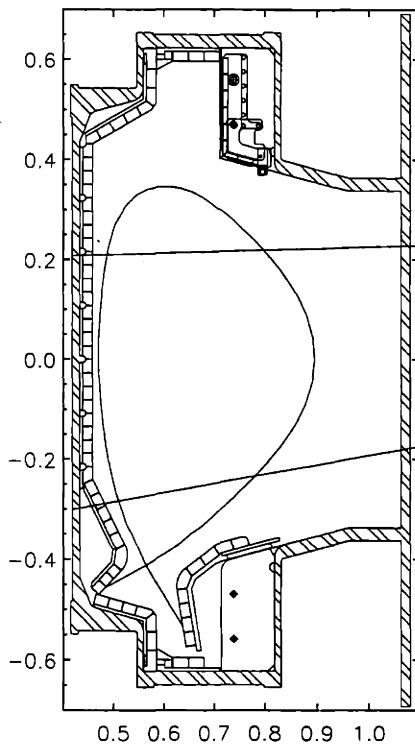
Figure 2-5: Range of viewing chords available to the VUV spectrometer.

2.2 Impurity Injection

Several methods of injecting impurities are available in the Alcator C-Mod. Gas puffing injection, laser ablation and pellet injection are all used to various degrees for the experiments which study impurity behavior. Among them, gas puffing injection and laser ablation were used to inject impurities of interest for the studies in this thesis. The behavior of argon injected through the gas puffing system has also been studied for discharges during which a pellet injection system was used to inject lithium pellets.

2.2.1 Argon Injection via A Pulsed Gas Valve

The main gas fueling system, which is capable of injecting a calibrated amount of gaseous impurities, was used for these studies. This system used piezo-electric pulsed gas valves to control the flow of gas from a four liter holding plenum into the plasma.

The amount of gas introduced is controlled by varying the pulse length of the opening of the valve as well as the pressure in the holding plenum. For the experiments for this thesis, this type of valve is calibrated for argon. See discussion in Appendix A for details.

The main gas fueling system is capable of introducing impurities at five locations around the vacuum vessel. For argon injection, the valve located on the lower B port flange, B-side lower as it is called, is normally used.

Shown in the Figure 2-6 is the location of the argon injection. The location for scandium injection by the laser ablation technique, which is discussed in the next section, is also shown.
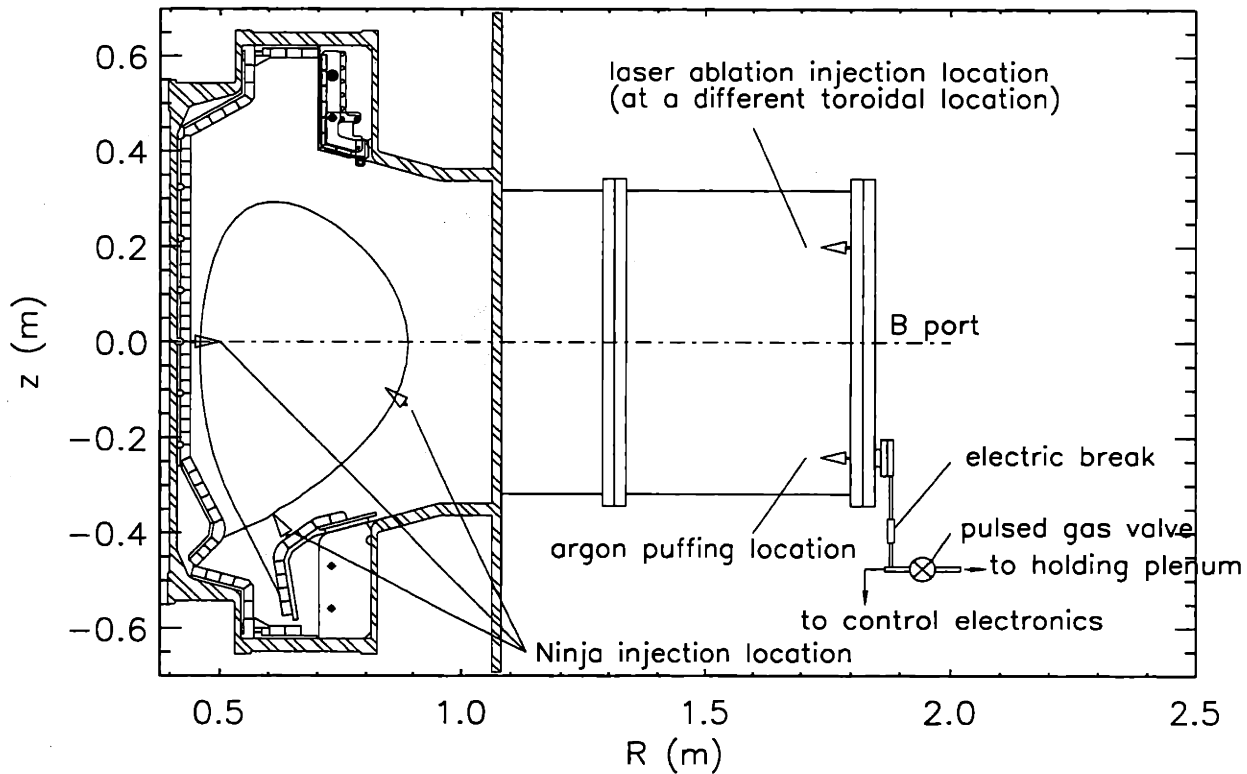
Figure 2-6: Poloidal location of B-side lower pulsed gas valve used in argon injection. Also shown is a schematics of the gas injection system setup. The poloidal location of the laser ablation injections is also shown though it is at a different toroidal location.

2.2.2 Divertor Gas Injection System

Another gaseous impurity injection system is the divertor gas injection system (NINJA), which is capable of introducing calibrated amount of impurity or fuel gas at up to 28 specified poloidal locations around the plasma. Due to the long length of the capillary tubing through which the gas is introduced, the time response of this injection system is relatively slow.

2.2.3 Laser Ablation Technique

The gas injection system is normally used for injecting recycling impurities, even though certain low recycling gaseous impurities are also available. The gas injection method is limited to injecting impurity neutrals with only relatively low energy. Pellet injection techniques can deliver macroscopic amounts of impurities at velocities of up to 1 km/s (Ref. [21]) for experiments which require impurities neutrals to be deposited deep within the plasma. But these injections are highly disturbing to the background plasma. For injections of trace amounts of impurity neutrals with finite energy, a technique called later ablation is also used. See Ref. [22].

In Alcator C-Mod , the laser ablation system uses targets which are two inch square standard glass slides with a vacuum deposited layer of the desired impurity material on the plasma facing side. The thickness of the deposited layer is typically 1 μm, but can range from 0.5 – 5 μm. (Ref. [20]). Adding to the versatility of the system is its capability to accommodate up to nine different target slides at any given time.

The laser beam used in this system is produced by a Q-switched ruby laser, with a collinear HeNe laser as the alignment instrument. Ablation by this technique produces a cloud of neutral atoms with a thermal distribution of energies superposed on a directed energy of somewhere between 1 and 10 eV.
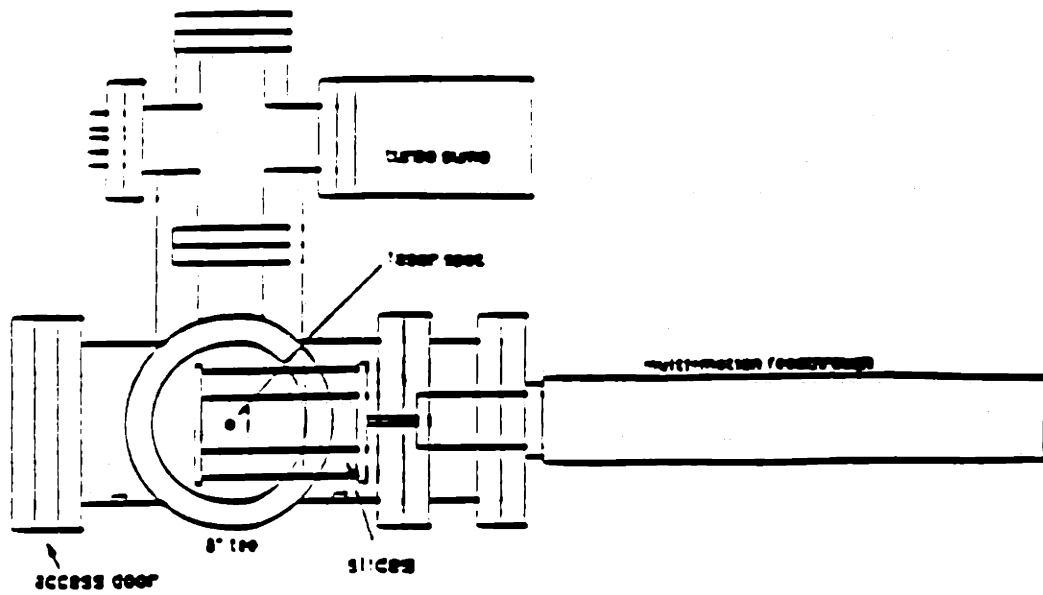
Figure 2-7: Schematic of the laser ablation impurity injector system as viewed from behind (i.e. looking toward the plasma). This is taken from Ref. [20].

2.3 Experiments

During the period in which the research for this thesis was carried out, a current flat-top during a discharge in Alcator C-Mod normally last around 0.8 second for a discharge with $B_T = 5\ Tesla, \bar{n}_e \sim 1.2 \times 10^{20}\ m^{-3}$ and $I_p = 0.8\ MA$. All the data used in this thesis were taken during discharges with $B_T = 5.3\ Tesla$ and $I_p = 0.8\ MA$. Argon is usually injected before the plasma current reaches a flat-top, giving argon sufficient time to penetrate to the core plasma and reach equilibrium. In this way, measurements can be make throughout the steady state phase. A typical argon pulse lasts around 30 ms with the absolute pressure in the holding plenum set at around 4 psi. Such a puff injects $\sim 10^{18}$ argon atoms. Figure 2-8 plots typical time histories of some important plasma parameters, including the helium-like argon x-ray signal and the voltage applied to the pulse gas valve used to inject the argon.
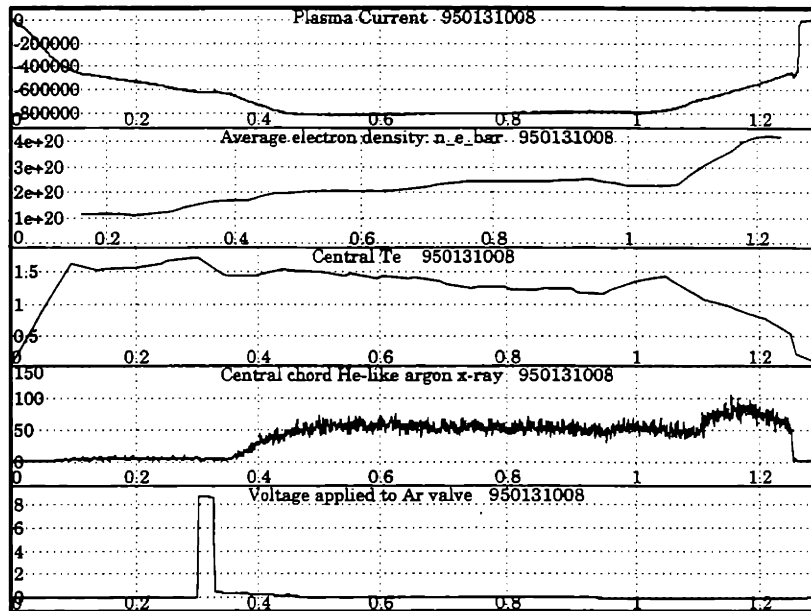
Figure 2-8:   Typical time histories of some important plasma parameters. Also shown is a typical time of the argon x-ray signal.

During each discharge, normally one or more spectrometers is devoted to the observation of helium-like argon spectra. Often the central chord is used to measure the impurity density.

Argon is normally introduced in a non-perturbing trace amount (less than 1%

of the total number of atoms in the plasma) to the plasma as a vehicle to provide understanding of the behavior of the impurities under various operating conditions. Several Alcator C-Mod runs were devoted to the comparison of impurity screening efficiency of diverted and limited plasmas. The inner wall clearances of the plasma Last Closed Flux Surface (LCFS) were varied on a discharge to discharge basis to toggle the plasma between the diverted and limited condition. Figure 2-9 shows the magnetic geometries of the diverted and the limited plasmas. (Note that the plasma of shot 950316015 is limited on the inner wall.) Comparisons of the diverted and limited plasmas were carried out for three plasma densities. During these runs, argon was the primary impurity of interest. But scandium was also injected using the laser ablation technique during one of the runs. The injection of scandium provided both complimentary data for the impurity screening study and data for the impurity transport coefficient study. Analysis of both types of impurity data obtained in this experiment proves that the use of the divertor significantly reduces the amount of low incident energy impurities enter the core plasma. The divertor is less effective against high incident energy impurities injected by the laser ablation technique.

Since the trace amounts of argon is non-perturbing to the plasma, it was injected during many experiments not explicitly dedicated to impurity studies. This enables the study of argon behavior over a wide range of operating conditions, although the interpretations are complicated by the fact that many different plasma parameters are often varied simultaneously. Data from runs during which the majority of the plasma parameters were held nearly fixed were analyzed. The analysis shows that the impurity penetration in a diverted plasma has little dependance on the divertor target plate strike points location, outer gap size and heating mode. For inner wall limited plasma there is little or no dependance on κ.

Argon was also injected during some of the lithium pellet injection runs. One pellet injection shot is analyzed and the results show that the argon density peaked strongly shortly after the pellet injection. The convective velocity is found to increase dramatically. The impurity diffusion coefficient is also found to change after the pellet injection.
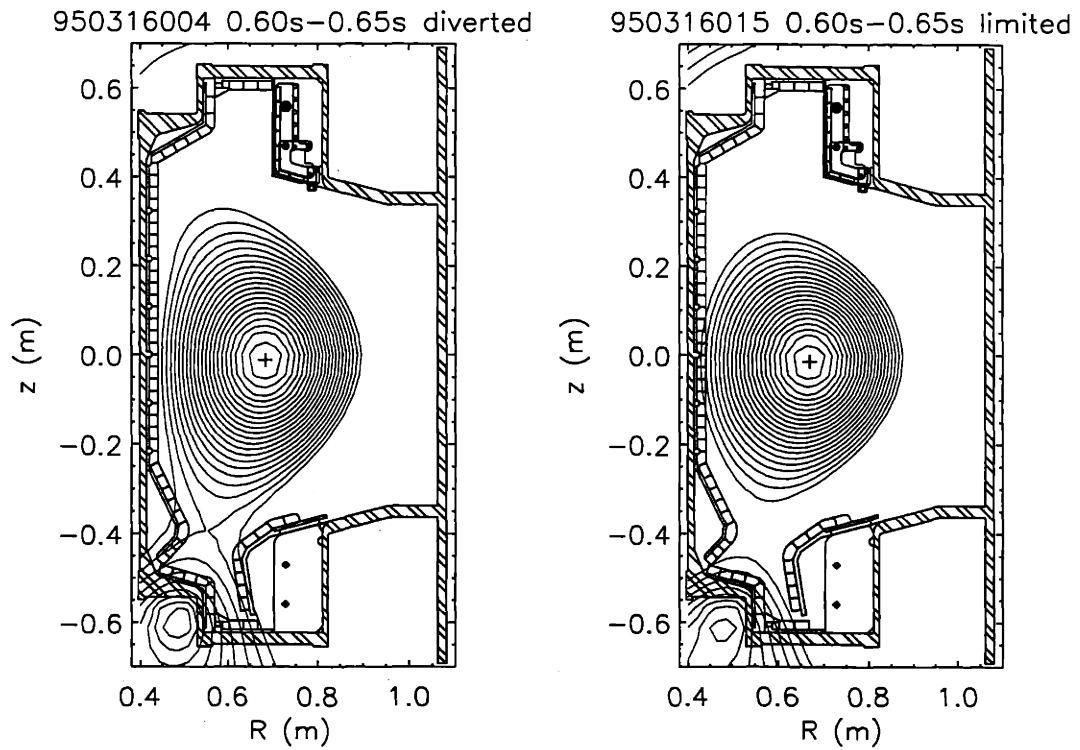
Figure 2-9: Magnetic geometries of a diverted and a limited plasma. Note that the plasma of shot 950316015 is limited on the inner wall.

Chapter 3

Modeling of Various Spectra

3.1 Helium-like Argon Spectrum

Modeling of the $\Delta n = 1$ helium-like lines and their satellite lines provides measurement of the argon density inside the plasma. The modeling process is described in the following sections.

3.1.1 Principal Lines

The $\Delta n = 1$ helium-like argon spectrum has four principal lines and eleven major satellite lines. The four principal lines are produced by $\Delta n = 1$ transitions in helium-like argon ions, while the eleven major satellite lines are produced by $\Delta n = 1$ transitions in lithium-like argon ions. Figure 3-1 shows a typical $\Delta n = 1$ helium-like argon spectrum.

The four principal lines are:

w	$1s2p\ ^1P_1 - 1s^2\ ^1S_0$	3949.2 mÅ	resonance line
x	$1s2p\ ^3P_2 - 1s^2\ ^1S_0$	3966.0 mÅ	intercombination line
y	$1s2p\ ^3P_1 - 1s^2\ ^1S_0$	3969.4 mÅ	intercombination line
z	$1s2s\ ^3S_1 - 1s^2\ ^1S_0$	3994.3 mÅ	forbidden line
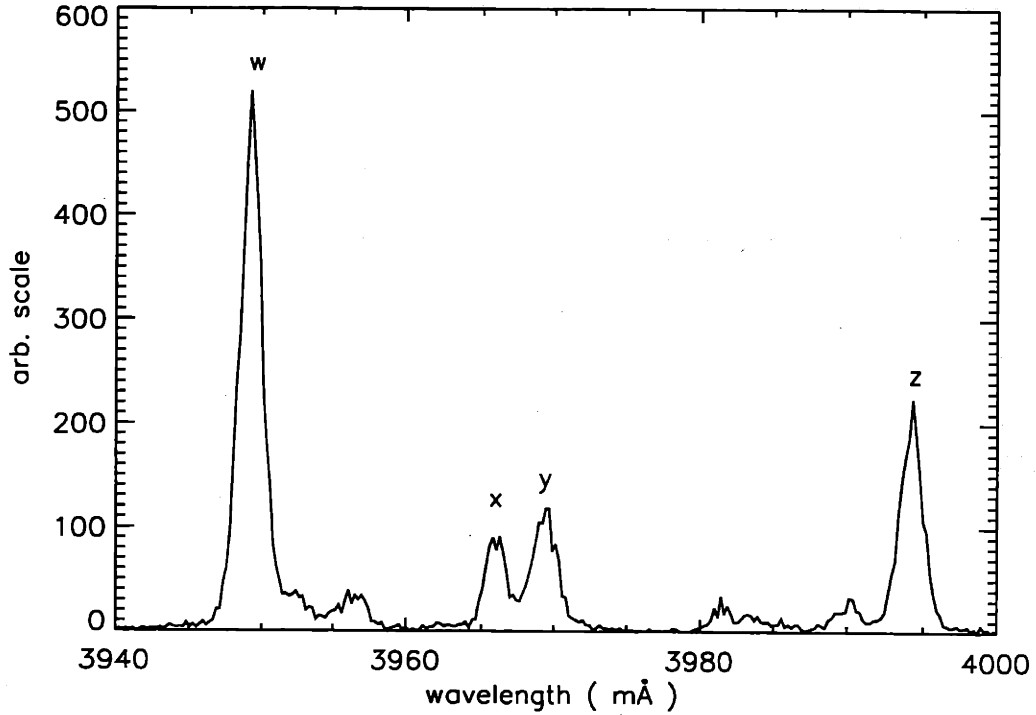
Figure 3-1: A helium-like argon spectrum.

To model the behavior of the line strengths under different plasma conditions, the population mechanisms of the upper energy levels which generate these lines have to be understood. Figure 3-2 is a diagram taken from Ref. [23] which shows all the excitation and de-excitation processes among the various levels. It should be noted that symbols are used in this figure and in the following discussions to represent various levels. g denotes the ground level $1s^2\ ^1S_0$ of the helium-like ion. g' denotes the ground level $1s^22s\ ^2S_{1/2}$ of the lithium-like ion. c denotes all the levels with $n > 2$ and the continuum, i.e. the hydrogen-like ion. 0 denotes $1s2p\ ^3P_0$. 1 denotes $1s2p\ ^3P_1$. 2 denotes $1s2p\ ^3P_2$. m denotes $1s2s\ ^3S_1$. $1'$ denotes $1s2p\ ^1P_1$. m' denotes $1s2s\ ^1S_0$.

For the plasma density we are interested in, which is around $10^{20}\ m^{-3}$, the photon induced excitation and de-excitation are insignificant, and are therefore ignored. The excited level population densities turned out to be very small compared to the ground state population density. Thus the ground state population density is assumed to be the same as the helium-like ion density for all practical applications. The level $1s2s$
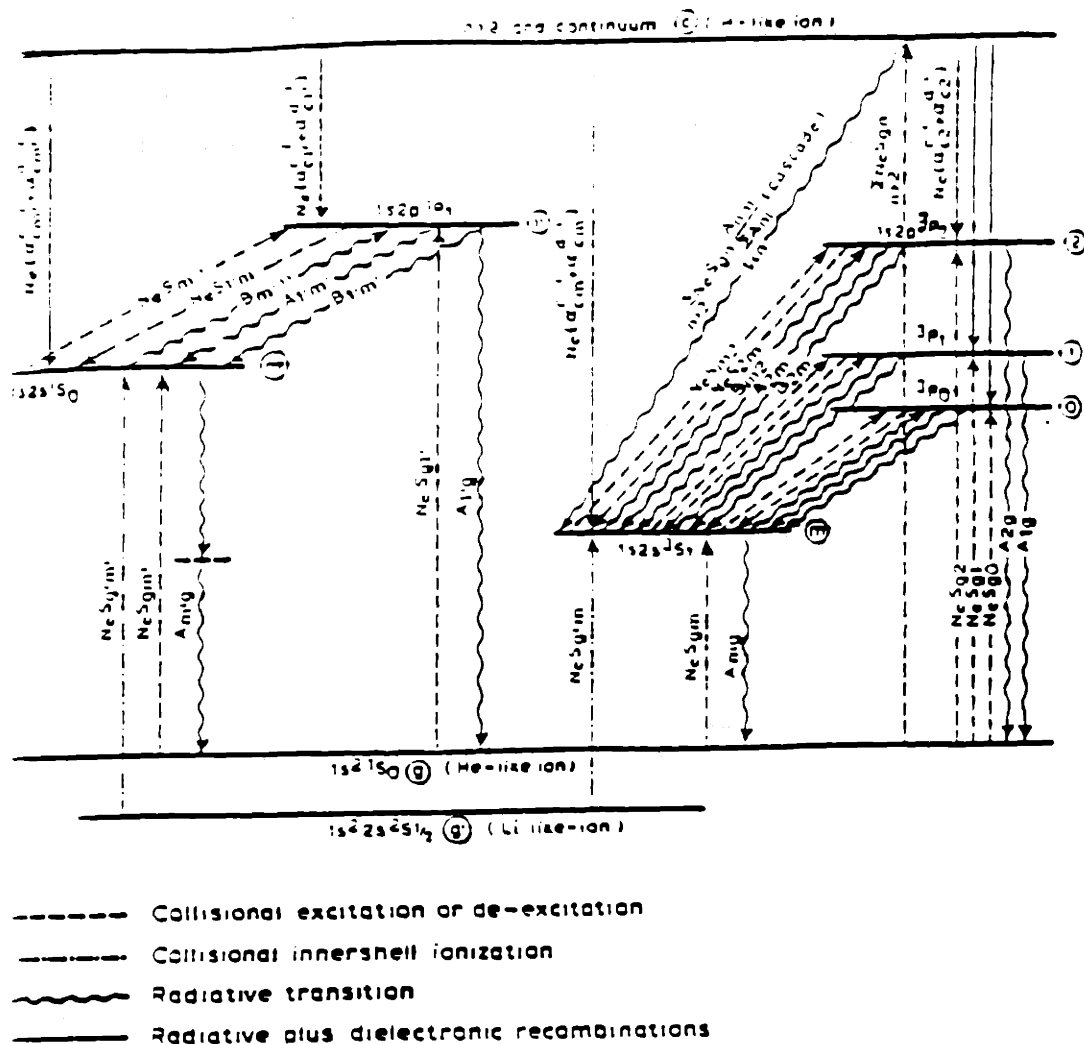
Figure 3-2: Population processes for $n = 2$ levels of helium-like argon. g denotes the ground level $1s^2\ ^1S_0$ of the helium-like ion. g' denotes the ground level $1s^2 2s\ ^2S_{1/2}$ of the lithium-like ion. c denotes all the levels with $n > 2$ and the continuum, i.e. the hydrogen-like ion. 0 denotes $1s2p\ ^3P_0$. 1 denotes $1s2p\ ^3P_1$. 2 denotes $1s2p\ ^3P_2$. m denotes $1s2s\ ^3S_1$. 1' denotes $1s2p\ ^1P_1$. m' denotes $1s2s\ ^1S_0$.

43

$^1S_0$ (m') is a metastable level from which the electron decays to the ground state only through a two-photon transition with an extremely small transition probability. This transition is also ignored as a depopulation mechanism. Table 3.1 lists all the population and depopulation processes for the six $n = 2$ levels.

After taking into account all the mentioned processes, a complete set of equations is reached. Equation 3.1 is an example of such an equation for the upper level of x line:

$$n_x(A_{2g} + A_{2m} + n_e S_{2m}) = n_z n_e S_{m2} + n_H n_e \alpha'_{c2} + n_{He} n_e S'_{g2} \quad . \tag{3.1}$$

Equations similar to this were written for each of the six levels. The equations were solved to give the populations of the upper levels of the w, x, y and z line. The results are shown below:

$$n_w = \frac{(n_H n_e \alpha'_{cm'} + n_{He} n_e S'_{gm'} + n_{Li} n_e S_{g'm'})S_{m'1'} + (n_{He} S'_{g1'} + n_H \alpha'_{c1'})(A_{m'g} + n_e S_{m'1'})}{A_{m'g}(A_{1'g} + A_{1'm'}) + n_e(S_{1'm'} A_{m'g} + S_{m'1'} A_{1'g})} n_e , \tag{3.2}$$

$$n_z = n_e\left(n_{He}\left(S'_{gm} + \sum_{k=0}^{2} S'_{gk}\right) + n_H\left(\alpha'_{cm} + \sum_{k=0}^{2} \alpha'_{gk}\right) + n_{Li}S_{g'm} - \frac{n_H \alpha'_{c1} + n_{He} S'_{g1}}{1 + A_{1m}/A_{1g} + n_e S_{1m}/A_{1g}} -$$
$$\frac{n_H \alpha'_{c2} + n_{He} S'_{g2}}{1 + A_{2m}/A_{2g} + n_e S_{2m}/A_{2g}}\right) / \left(A_{mg} + \frac{n_e S_{m1}}{A_{1g} + A_{1m} + n_e S_{1m}} A_{1g} + \frac{n_e S_{m2}}{A_{2g} + A_{2m} + n_e S_{2m}} A_{2g}\right) \tag{3.3}$$

$$n_x = \frac{n_z S_{m2} + n_H \alpha'_{c2} + n_{He} S'_{g2}}{A_{2g} + A_{2m} + n_e S_{2m}} n_e , \tag{3.4}$$

$$n_y = \frac{n_z S_{m1} + n_H \alpha'_{c1} + n_{He} S'_{g1}}{A_{1g} + A_{1m} + n_e S_{1m}} n_e , \tag{3.5}$$

in which:

n_H, n_{He}, n_{Li} and n_e are hydrogen-like Ar density, helium-like Ar density, Li-like Ar density and electron density respectively;

n_w, n_z, n_x and n_y are the population densities of the upper levels of the w, z, x and y lines respectively;

Key	Population Process	Depopulation Process
1′	collisional excitation from ground level of helium-like Ar ion with cascades from excited $(n > 2)$ levels; radiative recombination and dielectronic recombination from hydrogen-like Ar ion with cascades; collisional excitation from $1s2s^1S_0$	spontaneous transition to ground level; spontaneous and collisional transitions to $1s2s^1S_0$
m′	collisional excitation from ground state with cascades; radiative and dielectronic recombination from hydrogen-like Ar with cascades; inner shell ionization from Li-like ground state; spontaneous and collisional transitions from $1s2p^1P_1$.	collisional excitation to $1s2p^1P_1$ two photon transition to the ground level.
0, 1 & 2	collisional excitation from ground state and $1s2s^3S_1$ with cascades; radiative recombination and dielectronic recombination from hydrogen-like Ar ion with cascades.	spontaneous transition to ground state and to $1s2s^3S_1$ (level 0 doesn't have spontaneous transition to ground level)
m	excitation from helium-like ground state with cascades; inner shell ionization from Li-like ground state; radiative recombination and dielectronic recombination with cascades; spontaneous transitions from $1s2p^3P_2, 1s2p^3P_1$ and $1s2p^3P_0$; possible cascades from charge exchange recombination into levels around $n = 9$.	spontaneous transition to ground state of helium-like ion; collisional excitation to $1s2p^3P_2$, $1s2p^3P_1$ and $1s2p^3P_0$.

Table 3.1: Population processes for $n = 2$ levels of helium-like argon

A_{ij} are the spontaneous transition probabilities between level i and j;

S_{ij} are the collisional transition rate coefficients between $n = 2$ levels i and j;

S'_{gk} are the collisional excitation rates from the ground state to upper levels of the w,z,x and y lines, with cascades from higher levels taken into account;

α'_{ck} are the sum of radiative recombination and dielectronic recombination rate coefficients, with cascades from higher levels taken into account.

All the rate coefficients mentioned above are taken from Ref. [23]. Formulas for these rate coefficients are also given in Appendix B. Figures 3-3 to 3-6 plot the three major rate coefficients for each line: collisional excitation from the ground state, dielectronic recombination and radiative recombination, as functions of the electron temperature T_e. For all four lines, the collisional excitation rates are the highest at high temperature. In cases when the helium-like argon is abundant, collisional excitation is the dominant population process at high temperature (> 1.5 keV). At low temperature (several hundred eV), like that in the plasma edge region, the radiative recombination rates are several order of magnitude higher than both the collisional excitation and the dielectronic recombination. This doesn't necessarily mean that the radiative recombination contributes to the populations of the upper levels more than the collisional excitation does in low temperature region due to the fact that the hydrogen-like argon density is also much lower than the helium-like argon density if coronal equilibrium is assumed. [1] However, in tokamak plasmas where the impurity diffusion processes result in relatively abundant hydrogen-like argon ions in the low temperature region, the radiative recombination processes become dominant for population of the $n = 2$ levels. In any case, dielectronic recombination contributes little to the population of those levels.

The emissivity for transition from level i to level f is:

$$E(if) = n_e n_i A_{if} , \qquad\qquad (3.6)$$

---

[1]Coronal equilibrium assumes that all upward transitions are collisional and all downward transitions are radiative.
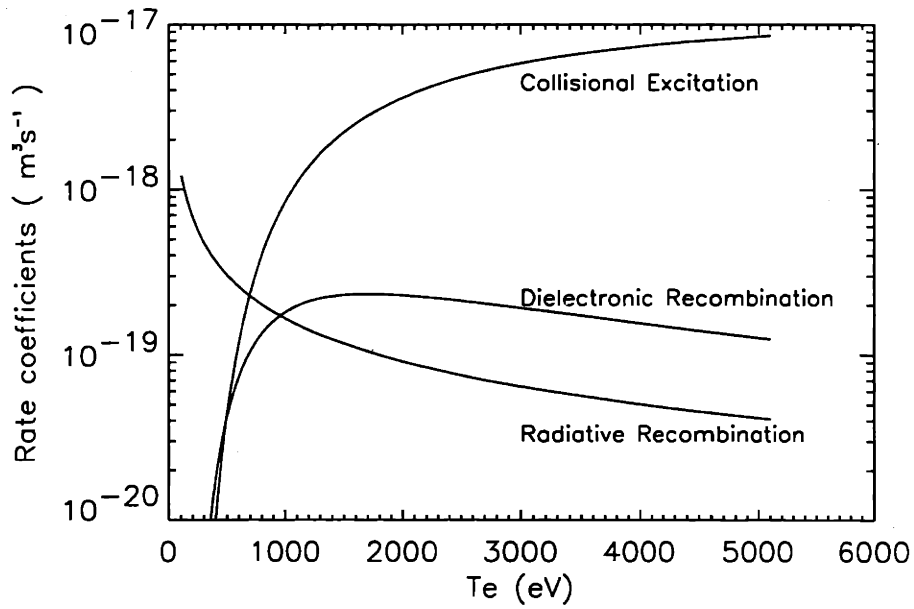
Figure 3-3:   Rate coefficients for major population processes for helium-like argon w line versus electron temperature.
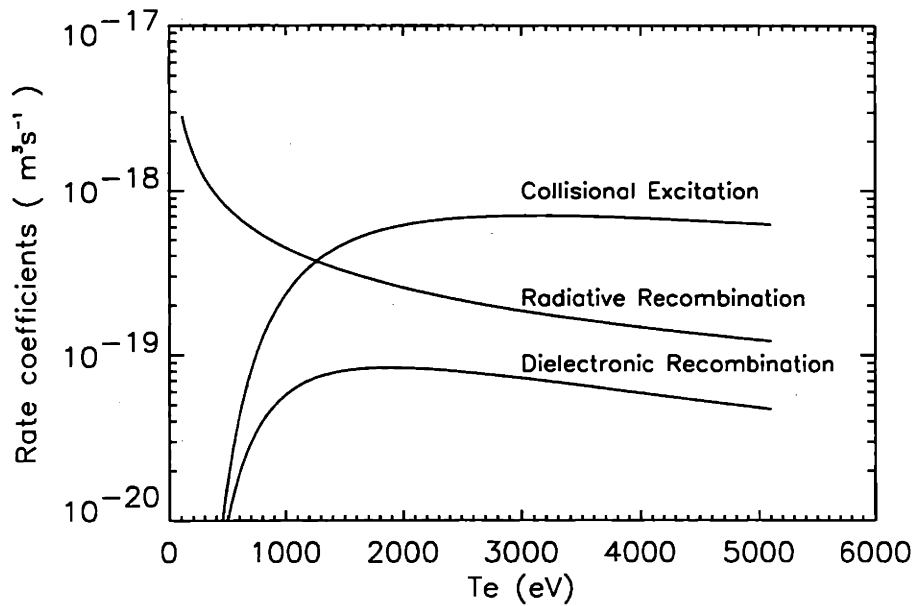
Figure 3-4:   Rate coefficients for major population processes for helium-like argon x line versus electron temperature.
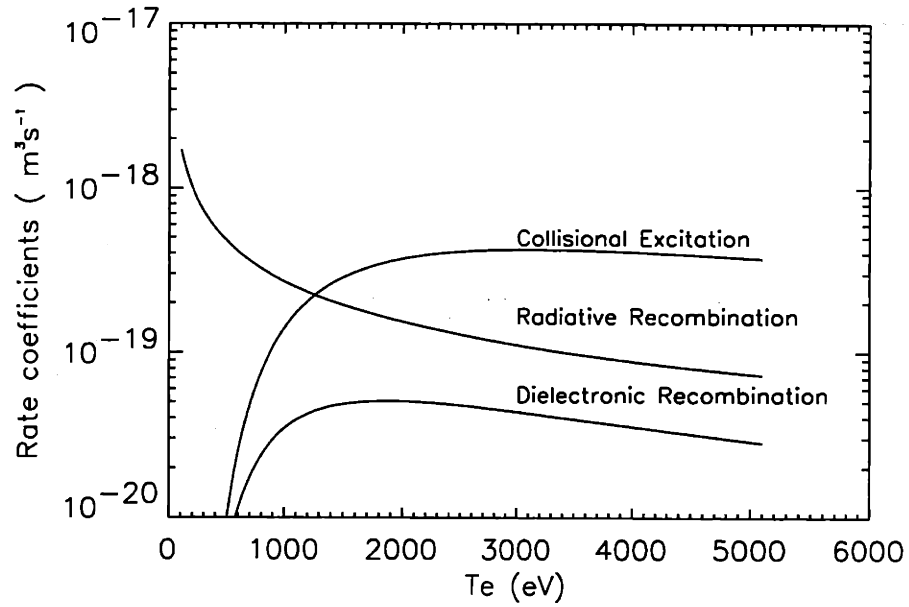
Figure 3-5: Rate coefficients for major population processes for helium-like argon y line versus electron temperature.
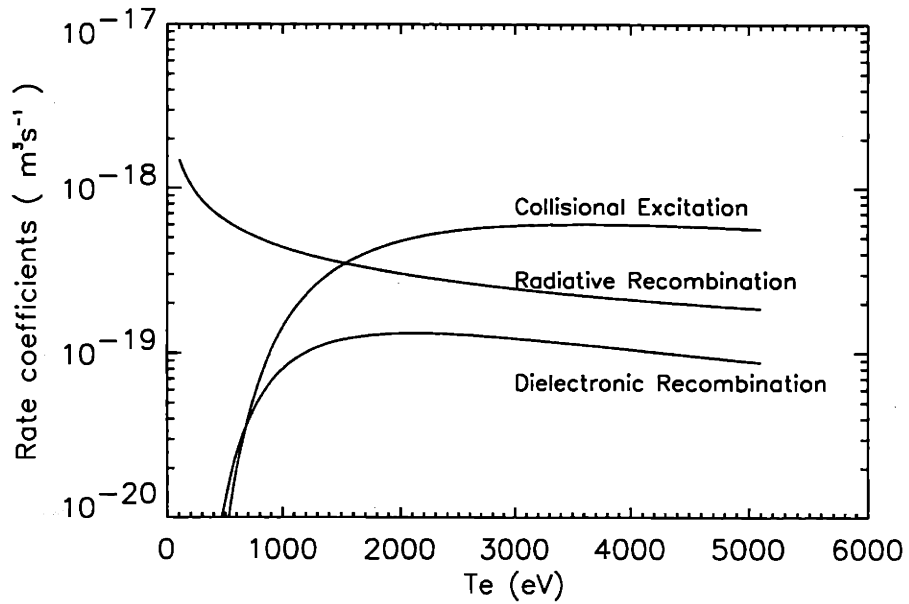
Figure 3-6: Rate coefficients for major population processes for helium-like argon z line versus electron temperature.

The following is the emissivity for the resonance line as an example:

$$E_w = \frac{(n_H n_e \alpha'_{cm'} + n_{He} n_e S'_{gm'} + n_{Li} n_e S_{g'm'}) S_{m'1'} + (n_{He} S'_{g1'} + n_H \alpha'_{c1'})(A_{m'g} + n_e S_{m'1'})}{A_{m'g}(A_{1'g} + A_{1'm'}) + n_e(S_{1'm'} A_{m'g} + S_{m'1'} A_{1'g})} n_e^2 A_{1'g} \; .$$

(3.7)

3.1.2 Charge Exchange Recombination

Another process that can play a role in populating the levels is charge exchange recombination, with subsequent cascades. The rate coefficient for charge exchange into the nth level $\alpha_{n,cx}$ is approximated in Ref. [24] as:

$$\alpha_{n,cx} = 2.2 \times 10^{-14} T_i^{0.4} e^{-(n-9.1)^2} \; m^3 s^{-1} \; .$$

(3.8)

The l distribution of the electrons captured into the nth level is also given in Ref. [24] as:

$$W_{nl} = (2l+1) \frac{((n-1)!)^2}{(n+l)!(n-1-l)!} \; .$$

(3.9)

According to Equation 3.9, 11.1% of the electrons captured into $n = 9$ level are distributed to S levels, 26.7% to P levels and 28.3% to D levels. Within each l level, 1/4 of the electrons are captured into the singlet and 3/4 into the triplet states. Nearly all the singlet P electrons undergo spontaneous radiative transitions to the ground state. The majority of the S and D electrons cascade to $n = 2$ levels. The majority of the triplet P electrons also cascade to $1s2s\,^3S_1$. Figure 3-7 is an illustration of all the transitions from $n = 9$ levels to $n = 2$ levels permissible by the selection rules. Electrons in $n = 9, l > 2$ levels are forbidden by the selection rules to undergo direct transition to $n = 2$ levels. Instead, they have to cascade down to lower $l \leq 2$ levels first. This makes modeling that part of the cascade contribution very complicated. So contribution from electrons captured into $n = 9, l > 2$ levels are ignored for the sake of simplicity.
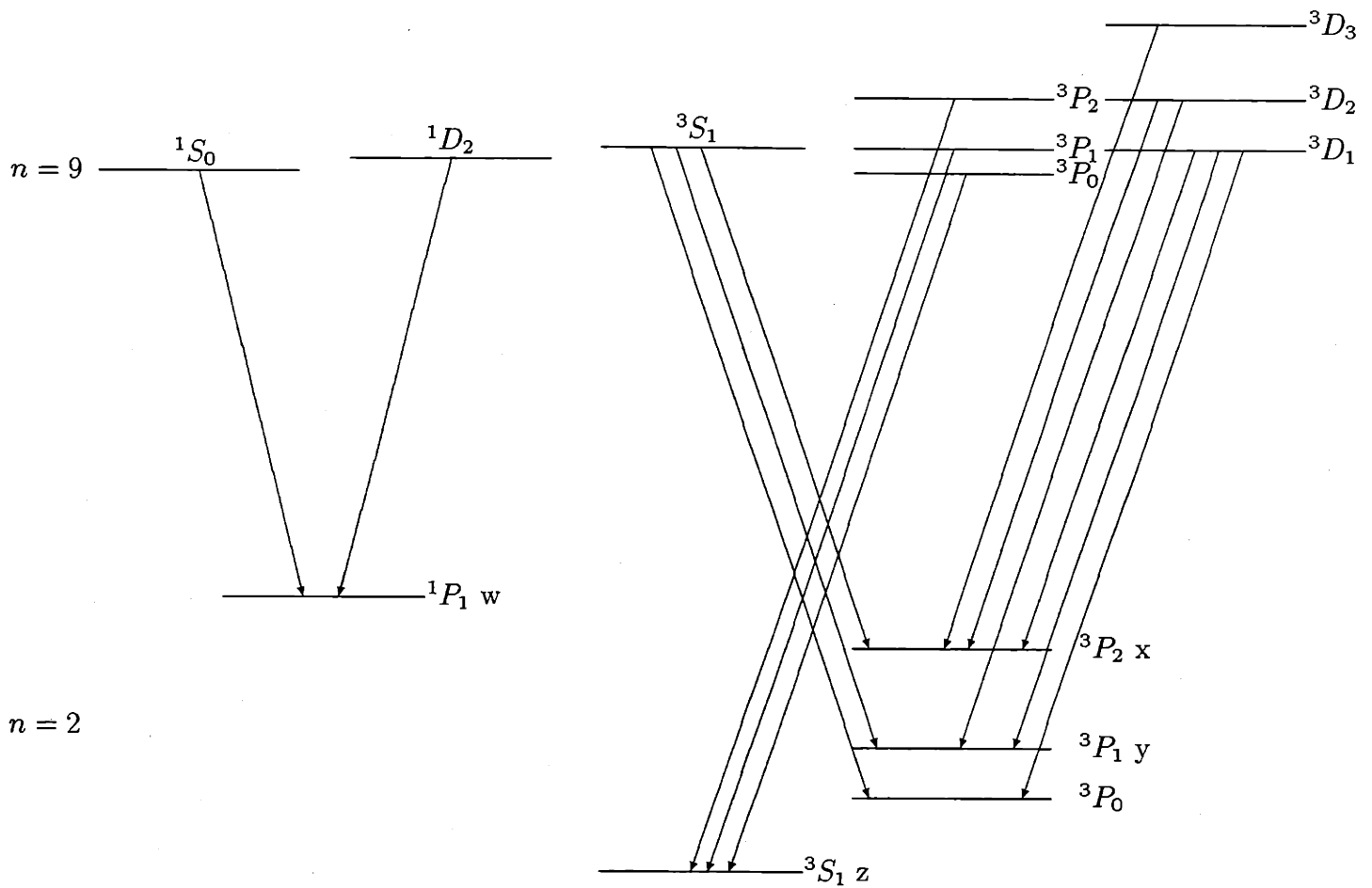
Figure 3-7: Permissible transitions for cascading from $n = 9$ levels to $n = 2$ levels

The contribution by the electrons captured into $n = 9$ levels to the population of $n = 2$ levels also largely depends on how the electrons are distributed among $n = 9$ sublevels with different J values and what the branching ratios of the cascade processes are. The following are three possibilities and the respective results:

1. Assume statistical distribution (i. e. proportional to $2J + 1$) among $n = 9$ sublevels and statistical distribution for the electrons cascading into $n = 2$ levels with different J values.

Based on this assumption (call it Model 1), after careful enumeration, contribution from all electrons captured into $n = 9$ levels to $n = 2$ levels are listed in Table 3.2.

level symbols	m′	1′	m	2	1	0
contribution (in %)	0	9.85	20.03	21.31	6.84	1.40

Table 3.2: Contribution to $n = 2$ levels from all electrons captured into $n = 9$ levels for Model 1.

2. Assume that in the high n levels interactions between sublevels break down the statistical distribution, and therefore assume an even distribution among $n = 9$ sublevels and a statistical distribution for the electrons cascading into $n = 2$ levels with different J values.

Based on this assumption (call it Model 2), contribution from all electrons captured into $n = 9$ levels to $n = 2$ levels are listed in Table 3.3.

level symbols	m′	1′	m	2	1	0
contribution (in %)	0	9.85	20.03	20.05	7.74	1.71

Table 3.3: Contribution to $n = 2$ levels from all electrons captured into $n = 9$ levels for Model 2.

3. Assume even distribution among $n = 9$ sublevels and even distribution for the electrons cascading into $n = 2$ levels with different J values.

level symbols	m′	1′	m	2	1	0
contribution (in %)	0	9.85	20.03	15.96	8.88	5.34

Table 3.4: Contribution to $n = 2$ levels from all electrons captured into $n = 9$ levels for Model 3.

Based on this assumption (call it Model 3), contribution from all electrons captured into $n = 9$ levels to $n = 2$ levels are listed in Table 3.4.

Similar calculations were also performed for $n = 8$ and $n = 10$ levels to include contributions from those levels. All three distribution models are used to try to fit the spectra. However, none proves to be successful in explaining the observed spectra that may have significant charge exchange recombination contribution. See Section 5.2.1 for detailed discussion.

3.1.3 Satellite Lines

Satellite lines are produced by $1s2l_1nl_2 \rightarrow 1s^2nl_2$ with the nl_2 electron as a spectator electron, i.e. the nl_2 electron remains in the same state before and after the transition and acts as a perturbation to the transition. This is why $1s2l_1nl_2 \rightarrow 1s^2nl_2$ produces emission lines close in wavelength to the lines produced by $1s2l_1 \rightarrow 1s^2$ transitions. The most notable satellite lines for the helium-like argon spectrum are the $n = 2$ and several $n = 3$ lines. (Ref. [25]) The related values used in the argon satellite line emission calculation are listed in Table 3.5.

When an electron with an energy slightly lower than the ionization threshold collides with a helium-like ion, it may cause excitation and simultaneously be captured into a high bound state. Such dielectronic capture can be reversed by autoionization and the helium-like ion is returned to the original state. But if a radiative transition, normally of the lower-level electron, rid the atom of its excessive energy before it breaks up of its own accord, the atom is then stabilized and a true dielectronic recombination is completed. For j, k, a, m and $n = 3$ satellite lines the main population process is dielectronic recombination from helium-like ions in the ground state. The emissivities of these lines are given as:

Array	Key	λ (mÅ)	A_a	A_r	F_2^*(if)
$1s2p^{2\,2}D_{5/2}$ - $1s^22p^2P_{3/2}$	j	3944.2	15.19	5.11	22.95
$1s2s2p^2P_{3/2}$ - $1s^22s^2S_{1/2}$	q	3981.6	.26	10.08	1.03
$1s2s2p^2P_{1/2}$ - $1s^22s^2S_{1/2}$	r	3983.7	1.56	8.52	2.64
$1s2p^{2\,2}D_{3/2}$ - $1s^22p^2P_{1/2}$	k	3990.2	14.44	5.84	16.64
$1s2p^{2\,2}P_{3/2}$ - $1s^22p^2P_{3/2}$	a	3986.2	.97	13.73	3.37
$1s2s2p^2P_{3/2}$ - $1s^22s^2S_{1/2}$	s	3967.9	10.28	.55	2.07
$1s2s2p^2P_{1/2}$ - $1s^22s^2S_{1/2}$	t	3968.7	9.03	2.13	3.44
$1s2p^{2\,2}S_{1/2}$ - $1s^22p^2P_{3/2}$	m	3966.1	2.26	4.08	2.57
$1s2s3d^2F_{7/2}$ - $1s^23d^2D_{5/2}$		3951.6	1.37	8.74	9.45
$1s2s3p^2D_{3/2}$ - $1s^23p^2P_{1/2}$		3955.5	3.45	8.58	9.51
$1s2s3p^2D_{5/2}$ - $1s^23p^2P_{3/2}$		3956.6	3.67	8.70	15.05

Table 3.5: Satellite lines of helium-like argon $\Delta n = 1$ transitions (A_a, A_r and F_2^*(if) in $10^{13}s^{-1}$)

$$E_s(T_e) = n_e n_{He} F_2^* F_1^*(i, T_e) \ , \tag{3.10}$$

where $F_1^*(i, T_e) F_2^*$ is the effective dielectronic recombination rate coefficient. $F_1^*(i, T_e)$ is given as:

$$F_1^*(i, T_e) = 1.659 \times 10^{-28} T_e^{-3/2} e^{-\frac{E_{sg}}{T_e}} \ m^3 \ , \tag{3.11}$$

and F_2^* is listed in Table 3.5.

For q, r, s and t satellite lines, inner-shell excitation from lithium-like ion ground states also plays a major role in population of the upper levels.

This part of the emissivity is

$$E_s(T_e) = n_e n_{Li} C_{if}(T_e) \ , \tag{3.12}$$

where C_{if} is the effective excitation rate which is obtained by applying a Z-scaling:

$$C_{if}(A, T_e) = C_{if}[B, (\frac{Z_B}{Z_A})^2 T_e](\frac{Z_B}{Z_A})^3 \tag{3.13}$$

to calcium data, taken from Ref. [26], Table 7b. Where A, B are the elements the scaling is applied to. In this case, A is Ar and B is Sc.
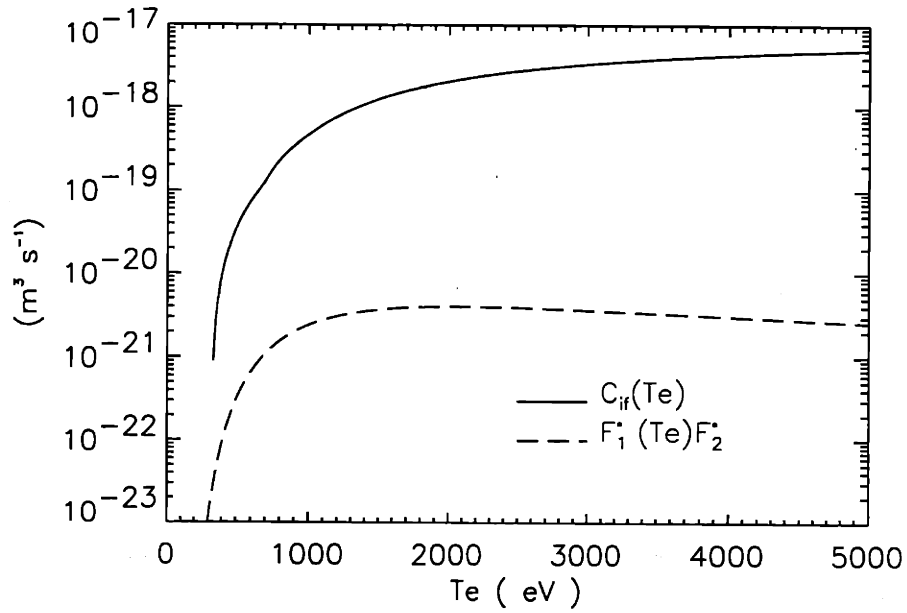
Figure 3-8: $C_{if}(T_e)$ and $F_1^*(T_e)F_2^*$ versus T_e for helium-like argon satellite line q, where $C_{if}(T_e)$ is the effective inner shell excitation rate for the lithium-like ions and $F_1^*F_2^*$ is the effective dielectronic recombination rate coefficient for the helium-like ions.
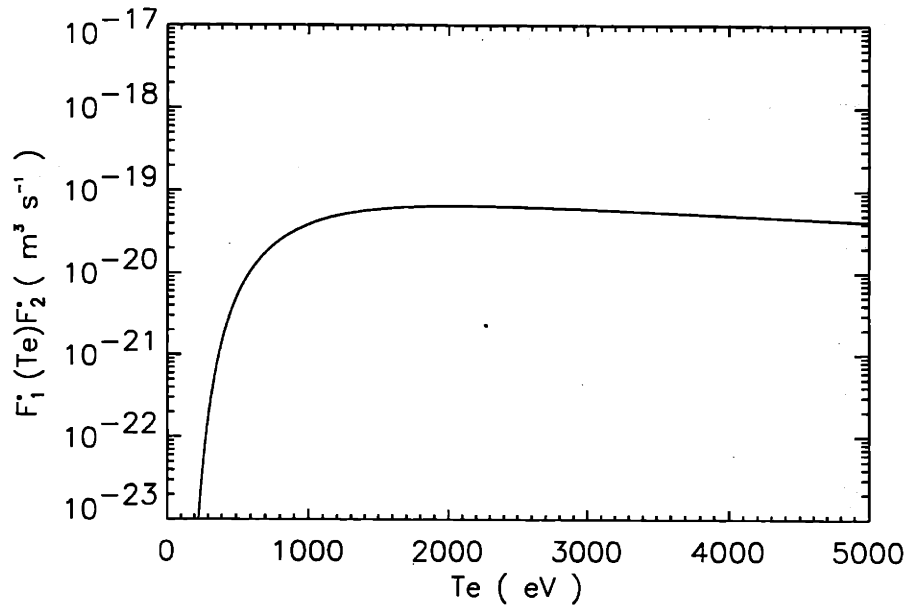
Figure 3-9: $F_1^*(T_e)F_2^*$ versus T_e for helium-like argon satellite line k, where $F_1^*F_2^*$ is the effective dielectronic recombination rate coefficient for the helium-like ions.

Figure 3-8 shows C_{if} and $F_1^* F_2^*$ versus T_e for the q satellite line of helium-like argon. Inner shell excitation is the dominant population process when the lithium-like argon density is comparable to, or higher than, the helium-like argon density. Figure 3-9 shows $F_1^* F_2^*$ versus T_e for the k satellite line of helium-like argon.

The above formulas and A_a, A_r and $F_2^*(if)$ are taken from Ref. [25]. The wavelengths of the satellite lines are taken from Ref. [27]. It is noticed that the wavelengths given in Ref. [27] have systematic shifts which are corrected in this thesis by comparing the wavelength of the forbidden line (z) given in the Ref. [27] with what is measured in Alcator C experiments (Ref. [9]) and applying the difference to all other wavelengths.

To calculate the emissivity of helium-like argon transitions, the electron temperature T_e profile is taken from Electron Cyclotron Emission (ECE) measurements (Ref. [13]); the electron density profile is taken from Two Color Interferometer (TCI) measurements (Ref. [14]); the density profiles for various argon charge states are provided by the MIST (Multiple Ionization State Transport) transport code, (Ref. [28]), with the assumption of constant diffusion coefficient of $D = 0.6$ m^2/sec (inferred from laser ablation impurity injection experiments) and a convective velocity profile of $v(r) = 0.5 \frac{-2D}{0.22} \frac{r}{0.22}$ m/sec, r is the minor radius in m; the total argon density left as a variable.

A synthetic spectrum calculated from measured n_e (Figure 3-14) and T_e (Figure 3-15) profiles is illustrated in Figure 3-10, with the positions of the principle lines and important satellite lines marked out.

3.2 Helium-like Scandium Spectrum

The helium-like scandium ($z = 21$) spectrum is very similar to that of argon ($z = 18$) due to their proximity in atomic number.

The four principal lines of helium-like scandium are:
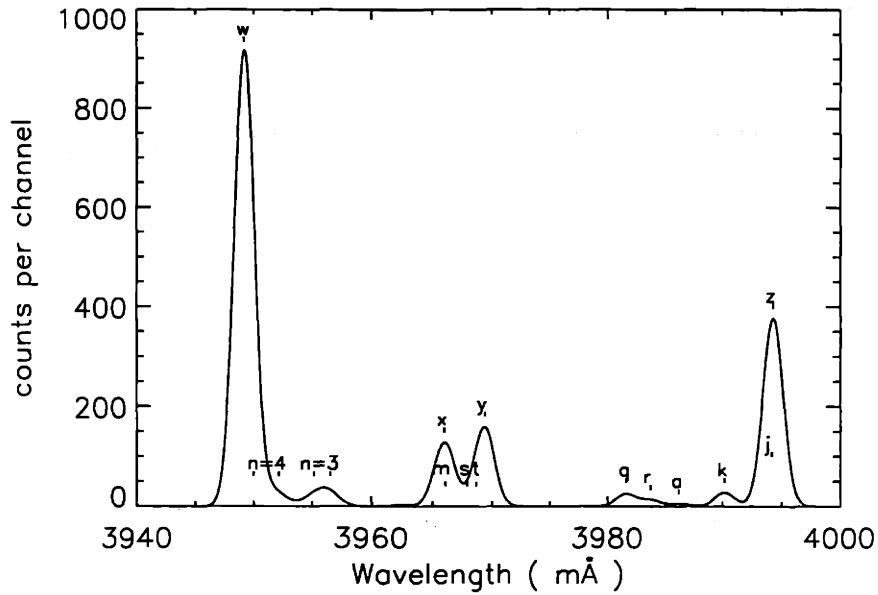
Figure 3-10:   A helium-like argon synthetic spectrum.

w	$1s2p\ ^1P_1 - 1s^2\ ^1S_0$	2873.3 mÅ	resonance line
x	$1s2p\ ^3P_2 - 1s^2\ ^1S_0$	2883.0 mÅ	intercombination line
y	$1s2p\ ^3P_1 - 1s^2\ ^1S_0$	2887.1 mÅ	intercombination line
z	$1s2s\ ^3S_1 - 1s^2\ ^1S_0$	2903.2 mÅ	forbidden line

The values needed to calculate the rate coefficients for the processes involved in the modeling of helium-like scandium are listed with the argon data in the previous tables. The formulas used for modeling the helium-like argon spectrum also apply to the modeling of the helium-like scandium spectrum.

The dielectronic recombination data for satellite lines of helium-like scandium are listed in Table 3.6. These data are obtained by applying a Z-scaling;

$$C_{if}^d(Sc, T_e) = C_{if}^d(Ar, (\frac{Z_{Ar}}{Z_{Sc}})^2 T_e)\frac{Z_{Sc}}{Z_{Ar}} \tag{3.14}$$

to argon satellite data with $Z_{Sc} = 19.5$ and $Z_{Ar} = 16.5$. Here $C_{if}^d = F_2^*(if)F_1^*(T_e)$,

Array	Key	λ (mÅ)	F_2^*(if)
$1s2p^{22}D_{5/2}$ - $1s^22p^2P_{3/2}$	j	2902.0	53.43
$1s2s2p^2P_{3/2}$ - $1s^22s^2S_{1/2}$	q	2893.4	2.40
$1s2s2p^2P_{1/2}$ - $1s^22s^2S_{1/2}$	r	2895.6	6.15
$1s2p^{22}D_{3/2}$ - $1s^22p^2P_{1/2}$	k	2898.4	38.74
$1s2p^{22}P_{3/2}$ - $1s^22p^2P_{3/2}$	a	2896.2	7.85
$1s2s2p^2P_{3/2}$ - $1s^22s^2S_{1/2}$	s	2884.8	4.82
$1s2s2p^2P_{1/2}$ - $1s^22s^2S_{1/2}$	t	2885.7	8.01
$1s2p^{22}S_{1/2}$ - $1s^22p^2P_{3/2}$	m	2884.4	5.98

Table 3.6: Satellite lines of helium-like scandium $\Delta n = 1$ transitions. (F_2^*(if) in $10^{13}s^{-1}$)

$F_1^*(T_e)$ is defined by Equation 3.11.

The contributions from inner-shell excitation to the satellite lines q, r, s and t are obtained by applying the Z-scaling Equation 3.13 to calcium data, taken from Ref. [26], Table 7b.
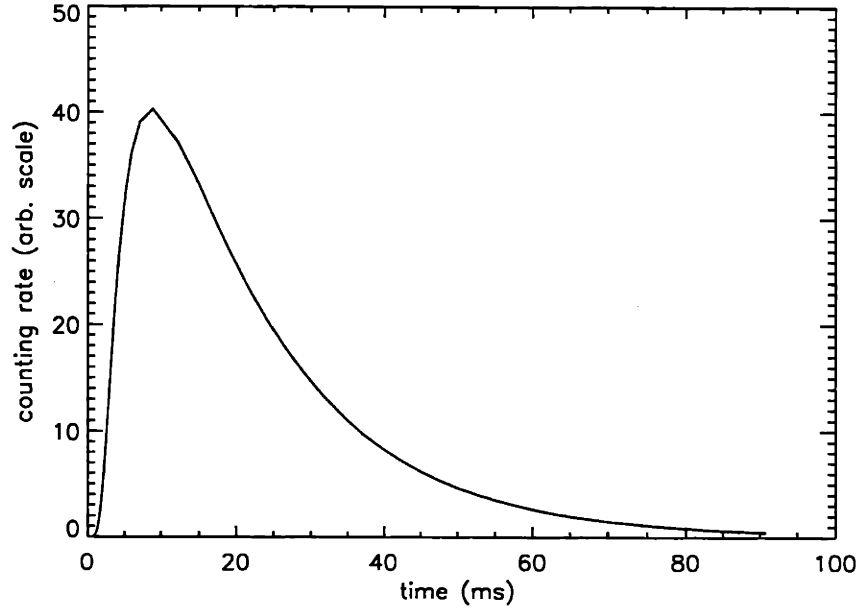
Figure 3-11:   A typical synthetic time history of x-ray signal of $\Delta n = 1$ helium-like scandium.

Unlike argon, scandium is a non-recycling impurity. It takes usually around 50 ms for injected scandium to diffuse out of the plasma. The histogram is not used in scandium analysis due to its 50 ms time resolution. Instead, data from the scaler

are used to give the time history measurements. To model the time history of the scandium line emission, the MIST code is run for scandium in a time-dependent mode to give the time-history of the fractional abundance of the various ionization stages of scandium. Then the synthetic time history (see Figure 3-11 for a typical synthetic time history of x-ray signal of $\Delta n = 1$ helium-like scandium) is compared and normalized to the experimental data to get the time history of the total scandium density profile in the plasma. Since the total number of scandium atoms in the plasma varies with time, the total number of scandium atoms is taken at the moment when the central scandium density reaches its maximum.

3.3   Lithium-like Argon and Scandium Spectrum

Another method of measuring argon and scandium is with the VUV spectrograph, which operates at ultra-violet wavelengths($50\overset{\circ}{A}$ – $1100\overset{\circ}{A}$). $\Delta l = 1$, $\Delta n = 0$ transitions of lithium-like argon and scandium produce photons of wavelength around 350 $\overset{\circ}{A}$, which are readily observable by the spectrograph, (Figure 3-12).

By modeling the spectra of these transitions and comparing them with the observed data, the impurity density can be deduced. The following will discuss the modeling of lithium-like argon lines in detail, with the understanding that lithium-like scandium is similar to argon in atomic physics.

The two principle lines from $\Delta l = 1$ transitions in argon are:

$1s^2 2p_{j=3/2} - 1s^2 2s$ 354.3 $\overset{\circ}{A}$

$1s^2 2p_{j=1/2} - 1s^2 2s$ 388.7 $\overset{\circ}{A}$

Rigorous calculation of the population of the upper level of those transitions requires detailed balancing of all the possible transitions between this level and nearby levels, i. e. the ground level and $n = 3$ levels. The following are the complete set of equations coupling the population of $n = 2$ and $n = 3$ levels:

$$n_{2p}A_{2p-2s} + n_{2p}n_e(S_{2p-2s} + S_{2p-3s} + S_{2p-3p} + S_{2p-3d}) =$$

58
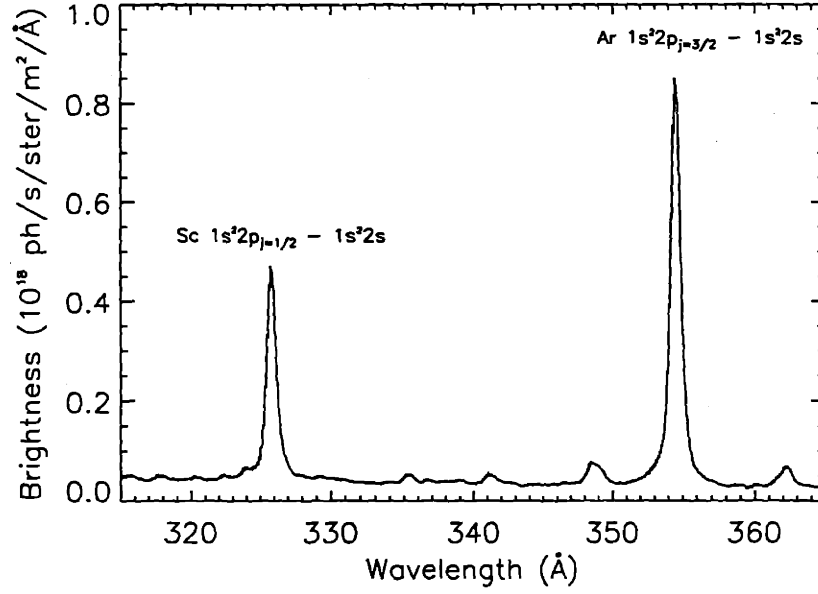
Figure 3-12: A spectrum of argon $1s^2 2p_{j=3/2} - 1s^2 2s$ and scandium $1s^2 2p_{j=1/2} - 1s^2 2s$ lines taken with the McPherson (VUV) spectrometer. The closeness of the two lines enables simultaneous measurement of both argon and scandium characteristics.

$$n_e(n_{2s}S_{2s-2p} + n_{3s}S_{3s-2p} + n_{3p}S_{3p-2p} + n_{3d}S_{3d-2p}) +$$

$$n_{3s}A_{3s-2p} + n_{3d}A_{3d-2p} + n_{He}n_e\alpha_{c-2p} , \qquad (3.15)$$

$$n_{3s}A_{3s-2p} + n_{3s}n_e(S_{3s-2s} + S_{3s-2p} + S_{3s-3p} + S_{3s-3d}) =$$

$$n_e(n_{2s}S_{2s-3s} + n_{2p}S_{2p-3s} + n_{3p}S_{3p-3s} + n_{3d}S_{3d-3s}) +$$

$$n_{3s}A_{3s-2p} + n_{3d}A_{3d-2p} + n_{He}n_e\alpha_{c-3s} , \qquad (3.16)$$

$$n_{3p}A_{3p-3s} + n_{3p}n_e(S_{3p-2s} + S_{3p-2p} + S_{3p-3s} + S_{3p-3d}) =$$

$$n_e(n_{2s}S_{2s-3p} + n_{2p}S_{2p-3p} + n_{3s}S_{3s-3p} + n_{3d}S_{3d-3p}) +$$

$$n_{3d}A_{3d-3p} + n_{He}n_e\alpha_{c-3p} , \qquad (3.17)$$

$$n_{3d}(A_{3d-2p} + A_{3d-3p}) + n_{3d}n_e(S_{3d-2s} + S_{3d-2p} + S_{3d-3s} + S_{3d-3p}) =$$

59

$$n_e \left(n_{2s} S_{2s-3d} + n_{2p} S_{2p-3d} + n_{3s} S_{3s-3d} + n_{3p} S_{3p-3d} \right) +$$

$$n_{He} n_e \alpha_{c-3d} \; . \tag{3.18}$$

n_{2p}, as well as the population densities of the $n = 3$, levels can be calculated by solving the above set of equations. Figure 3-13 plots the emissivity of the $1s^2 2p \rightarrow 1s^2 2s$ transitions versus electron temperature. It also plots the contribution to this emissivity by population processes other than collisional excitation, e.g., radiative recombination and cascades from $n = 3$ levels.
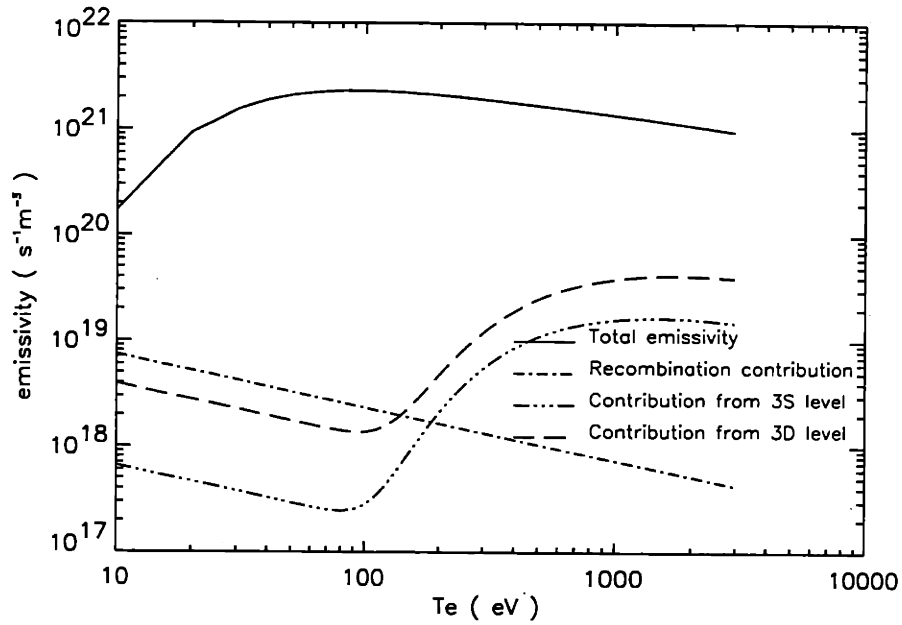
Figure 3-13: Contribution to lithium-like argon emissivity by various population processes. Calculated for $n_e = 10^{20} \; m^{-3}$, $n_{Ar^{16+}} = n_{Ar^{15}} = 10^{16} \; m^{-3}$.

Figure 3-13 shows that in the range of temperature that we are interested in, all other population and depopulation mechanisms are insignificant in comparison with the collisional excitation from the ground level. Hence all practical applications will take the collisional excitation from the ground level as the only population mechanism, for which the rate coefficient is;

$$S_{gk} = 1.58 \times 10^{-11} T_e^{-1/2} E_{ij}^{-1} f_{ij} \bar{\Omega}(y) e^{-y} \; m^3 s^{-1} \; , \tag{3.19}$$

where $y = E_{gk}/T_e$; E_{gk} is the excitation energy in eV; T_e is the electron temperature

Element	j	λ (Å)	E_{gk} (eV)	f_{ij}	A	B	C	D
Ar	$\frac{1}{2}$	388.7	31.9	0.0263	0.68	0.95	-0.47	0.28
	$\frac{3}{2}$	354.3	35.0	0.0584	0.68	0.95	-0.47	0.28
Sc	$\frac{1}{2}$	326.3	38.0	0.0220	0.68	0.96	-0.47	0.28
	$\frac{3}{2}$	281.8	44.3	0.0522	0.68	0.96	-0.47	0.28

Table 3.7: Parameters for lithium-like argon and scandium.

in eV; f_{ij} is the oscillator strength of the transition $i \to j$; $\bar{\Omega}(y)$ is the average of the collision strength, $\Omega(U)$, over the Maxwellian electron energy distribution:

$$\bar{\Omega}(y) = y e^y \int_1^\infty \Omega(U) e^{-yU} dU \ , \tag{3.20}$$

and can be approximated by:

$$\bar{\Omega}(y) = A + (By - Cy^2 + D)f(y) + Cy \ , \tag{3.21}$$

where A, B, C, D for the $j = \frac{1}{2}$ and $j = \frac{3}{2}$ levels for argon and scandium are listed in Table 3.7, and $f(y)$ is defined by:

$$f(y) = e^{-y} E_1(y) \ , \tag{3.22}$$

where:

$$E_1(y) = \int_1^\infty z^{-1} e^{-yz} dz \ , \tag{3.23}$$

and f can be approximated as;

$$f(x) = \ln\left(\frac{x+1}{x}\right) - \{0.36 + 0.03(x + 0.01)^a\}(x+1)^{-2} \ , \tag{3.24}$$

in which $a = 0.5$ ($x \geq 1$) or $a = -0.5$ ($x < 1$).

Lithium-like scandium transitions have very similar behaviors as the argon transitions.

$1s^2 2p_{j=3/2} - 1s^2 2s$ 281.8 Å

$1s^2 2p_{j=1/2} - 1s^2 2s$ 326.3 Å

The McPherson spectrograph is able to cover the argon $j = \frac{3}{2}$ line and the scandium $j = \frac{1}{2}$ line simultaneously. Thus it provides the measurements of both argon and scandium density in the plasma.

3.4   Testing the Helium-like Argon Modeling

Using the atomic physics calculation described in the last chapter, emissivities of various argon and scandium emission lines can be calculated as functions of given T_e, n_e and fractional abundance of argon and scandium ions. What are observed, however, are the integrals of the emissivities along the line of sight. With the emissivities given in the last chapter, a code was written to produce synthetic spectra for argon with given electron temperature and density profiles and density profiles of various argon charge states for a given line of sight. Geometric factors, crystal reflectivities, window transmissions and detector sensitivities are all taken into account in this code.
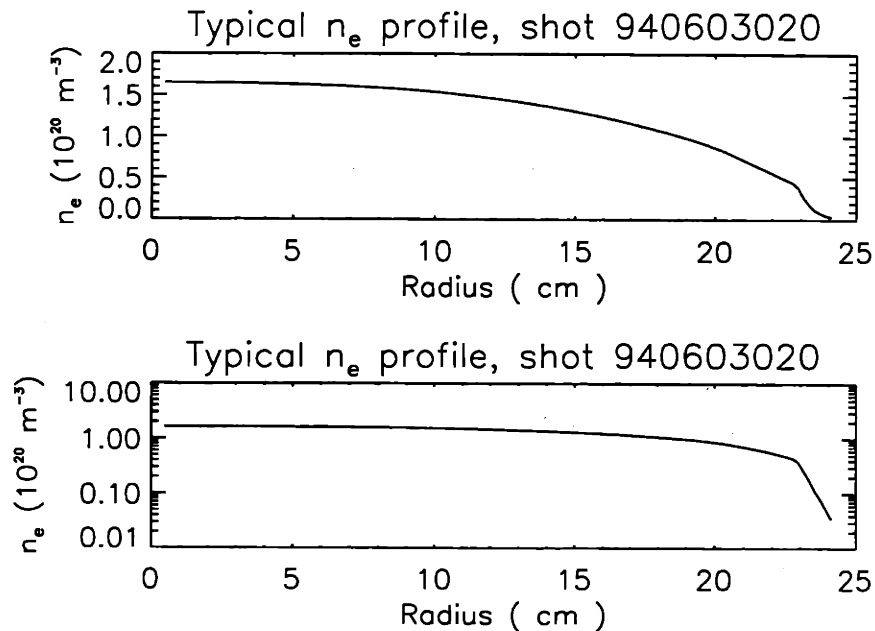
Figure 3-14:   Typical n_e profile shown in a linear and a log plot.

For the line of sight which is near the plasma center where the temperature is high, the dominant population process is collisional excitation from the ground state.

Typical Te profile, shot 940603020
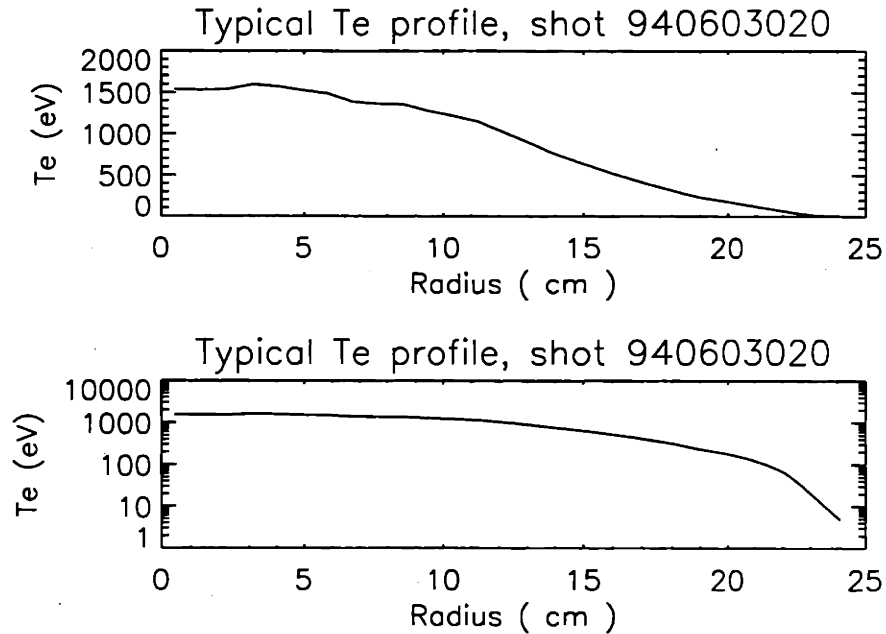
Figure 3-15: Typical T_e profile shown in a linear and a log plot.

Since this is a relatively simple process which is well understood and well documented and since the plasma parameters are well measured near the center, the spectrum of the centermost chord is used to calculate the total argon density. The n_e profile used in the modeling is taken from the Two Color Interferometer measurements. (Ref. [14]) Figure 3-14 shows a typical n_e profile. The T_e profile is taken from the Electron Cyclotron Emission measurements. (Ref. [13]) Figure 3-15 shows a typical T_e profile. The locations of the Hirex viewing chords as functions of flux surface are obtained by converting the vertical positions of the viewing chords using flux surface information provided by the EFIT code. Figure 3-16 shows a flux plot of Alcator C-Mod shot 940603020, with the viewing chords of the x-ray spectrometers overploted. As mentioned before, the total argon density is left as a variable in the MIST transport code. It is adjusted so that the synthetic spectrum fits best with the experimental data. In Figure 3-17 – Figure 3-20, the total argon density was adjusted so that the synthetic spectra for spectrometer #2, which looked at a line of sight 3.5 cm away from the center of the plasma, fitted best with the observed spectra. There was a good agreement between the synthetic spectra and the observed

spectra for this spectrometer. The same argon density profiles were then used to produce synthetic spectra for the spectrometers looking further out in the plasma. Those synthetic spectra also agreed with the observed ones within a 25% discrepancy. These agreements proved the validity of both the modeling of argon spectra and the assumption of the transport coefficients used in the MIST code.
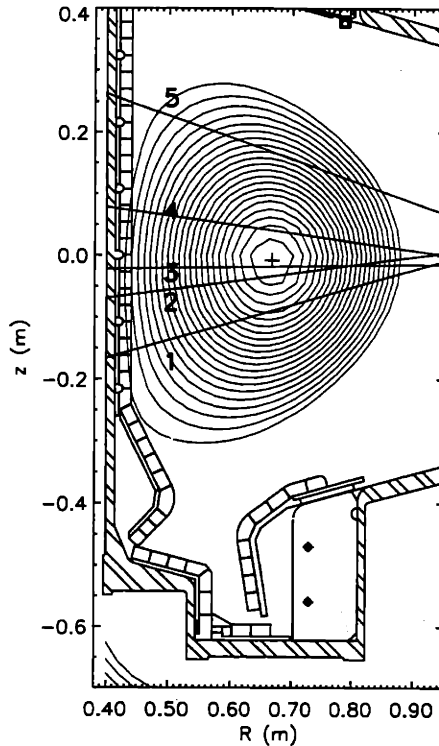
Figure 3-16:   Hirex viewing chord locations for Alcator C-Mod discharge 940603020.

It should be noted that while the spectra looking near the center of the plasma were modeled very well in terms of both principle line strengths and satellite line strengths, the discrepancy between the synthetic spectrum and the observed one increased as the line of sight moved further out, as illustrated in Figure 3-19 and Figure 3-20. Several factors could contribute to this discrepancy. The uncertainty of the measurements of T_e and n_e profiles increases at the outer region of the plasma. Therefore the synthetic spectrum calculated from those profiles also became less accurate. Also, the assumption of a spatially constant diffusion coefficient was not necessarily correct. Discussion in the following part of this thesis shows that the diffusion coefficient is

spatially variant for at least some cases. Thus in this specific case, the diffusion coefficient might not be taken as spatially constant in reality, hence causing the observed spectra to differ from those calculated assuming a spatially constant diffusion coefficient.
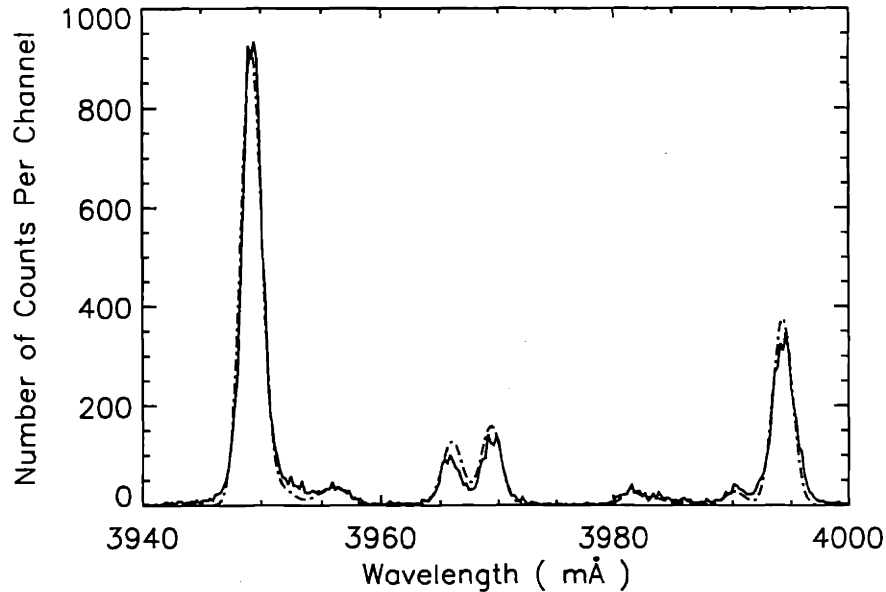
Figure 3-17: Fit for shot 940603020 HIREX spectrometer # 2 spectrum integrated from 0.8 sec — 0.85 sec viewing at minor radius of 3.0 cm. The solid line is the observed spectrum. The dashed line is the synthetic spectrum.

Figure 3-21 plots the calculated density profiles of the Ar ions using $D = 0.5\ m^2 s^{-1}$ and a convective velocity profile of $v(r) = 0.5\frac{-2D}{0.22}\frac{r}{0.22}$ m/sec for Alcator C-Mod plasma discharge 940603020. The total number of argon ions in the plasma is obtained by volume-integrating the sum of the density profiles of all charge states.

3.5 Obtaining the Central Argon Density Time History

Another technique to study the argon screening is to use the time history data taken from the scaler attached to each HIREX spectrometer. The scaler data provide a time history of the sum of all helium-like argon lines plus the satellite lines within the
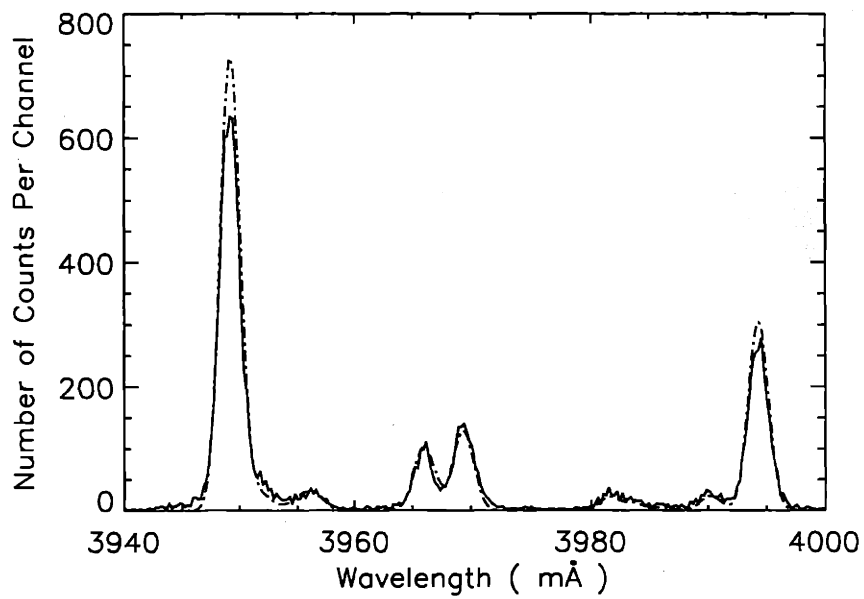
Figure 3-18: Fit for shot 940603020 HIREX spectrometer # 4 spectrum using argon density obtained by normalizing the brightness of w line of the synthetic spectrum of spectrometer #2 to its observed value. The spectrum was integrated from 0.8 sec — 0.85 sec viewing at minor radius of 4.5 cm. The solid line is the observed spectrum. The dashed line is the synthetic spectrum.

940603020 Spectrometer #1, .8 − .85 sec, 7.4 cm
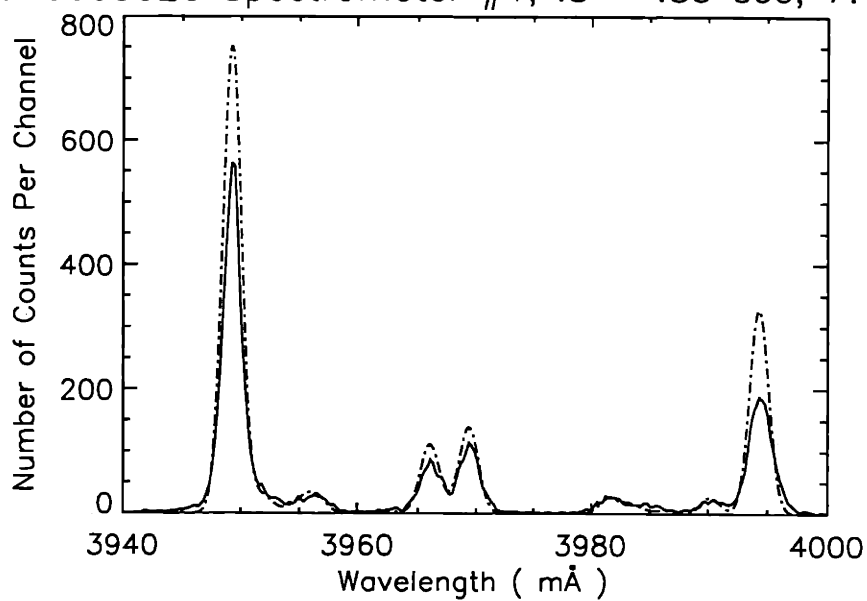
Figure 3-19: Fit for shot 940603020 HIREX spectrometer # 1 spectrum using argon density obtained by normalizing the brightness of w line of the synthetic spectrum of spectrometer #2 to its observed value. The spectrum was integrated from 0.8 sec — 0.85 sec viewing at minor radius of 7.4 cm. The solid line is the observed spectrum. The dashed line is the synthetic spectrum.
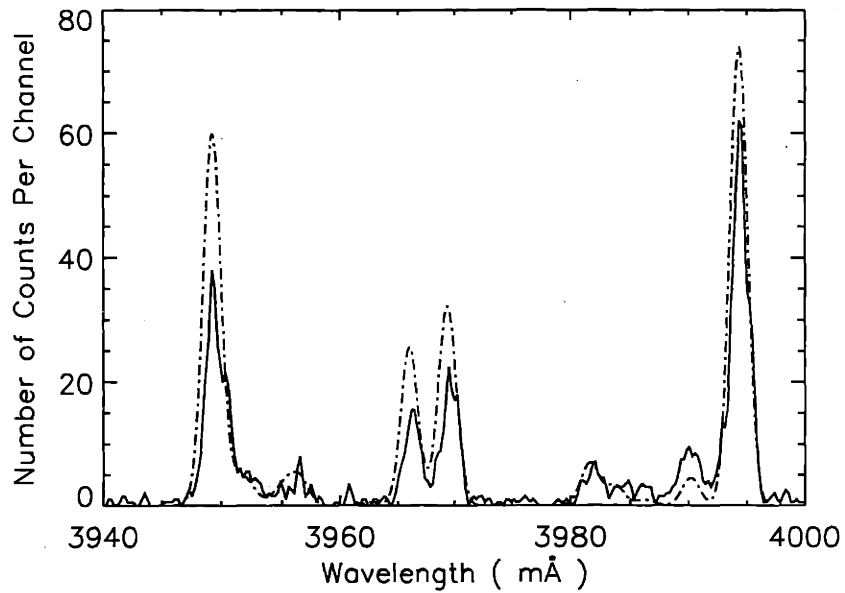
Figure 3-20: Fit for shot 940603020 HIREX spectrometer # 5 spectrum using argon density obtained by normalizing the brightness of w line of the synthetic spectrum of spectrometer #2 to its observed value. The spectrum was integrated from 0.8 sec — 0.85 sec viewing at minor radius of 15.0 cm. The solid line is the observed spectrum. The dashed line is the synthetic spectrum.
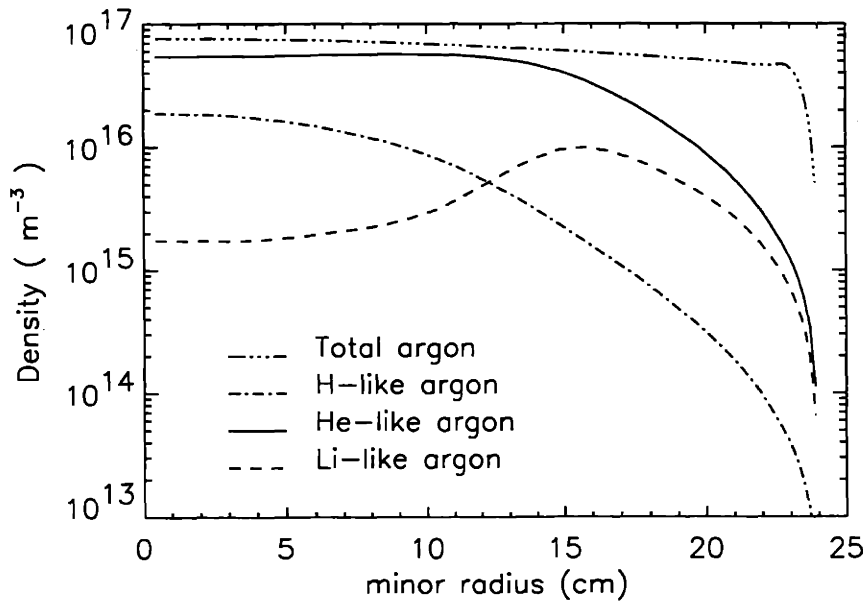
Figure 3-21: Density profiles for total argon, H-like argon, He-like argon and Li-like argon for shot 940603020.

spectrometer range. The analysis process is as following: T_e data and n_e are taken from the ECE and TCI measurements, respectively, for each specific moment. The fractional abundance of argon ions of various charge states are obtained by applying coronal equilibrium and the ignoring impurity transport. The MIST code isn't used in this technique because the brightness comes mostly from the vicinity of the plasma center and impurity transport has little effect on the charge state distribution of the argon ions in the plasma center. Figure 3-22 plots the comparison between the radial relative abundance profiles of argon ions produced by assuming coronal equilibrium alone and by using MIST code. It shows no significant difference in the plasma center. In the further out region of the plasma, however, the coronal equilibrium predicts much lower (two order of magnitude) hydrogen-like argon density than MIST code, which incorporates the impurity transport terms. In the previous discussion about the rate coefficients, the radiative recombination coefficients are shown to be several order of magnitude higher than the collisional excitation coefficients at temperature lower than several hundred eV, e.g. 500 eV. The fact that hydrogen-like argon density is comparable to the helium-like argon density in the outer part of the plasma means that radiative recombination becomes the dominant population process for all $\Delta n = 1$ lines beyond minor radius of 15 cm. Thus radiative recombination has to be taken into account in order to calculate the line ratios and the brightness profiles of the $\Delta n = 1$ lines correctly in the outer part of the plasma. This is why the atomic physics model used in this thesis includes radiative recombination in its calculation and use MIST-produced argon ion density profiles.

In Appendix C the technique for calculating the fractional abundance of argon ions is presented.

3.6 Conclusion

Modeling for the helium-like argon and scandium $\Delta n = 1$ transitions is developed, taking into account all possible collision excitations and de-excitations, inner shell excitations, radiative and dielectronic recombinations, charge-exchange recombinations
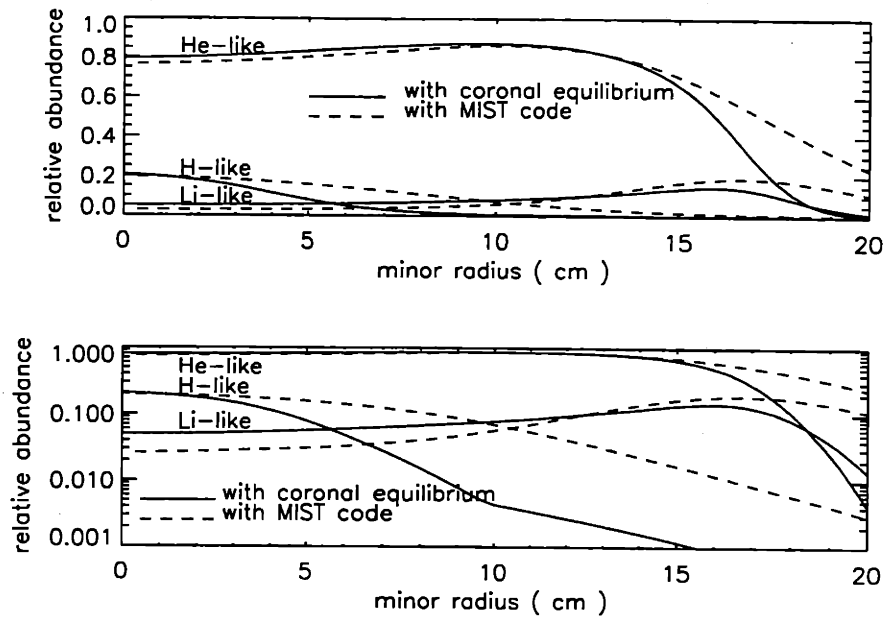
Figure 3-22: Linear and log plots of the comparison between coronal equilibrium-produced and MIST-produce abundance profiles of argon ions.

and spontaneous radiative decays between the ground states of helium-like argon, the ground states of lithium-like argon, and $n = 2$ levels, and among the $n = 2$ levels, and between the $n = 2$ levels and higher levels including the hydrogen-like argon. Utilizing the density profiles for various charge state provided by MIST code with anomalous impurity transport taken into account, this model is successful in fitting the experimentally observed spectrum taken with HIREX at various minor radius. Both the brightness profile of the lines and the line ratio between different lines agrees well with the observation. Also developed is the modeling of satellite lines to the helium-like argon and the modeling of lithium-like argon and scandium.

Chapter 4

Impurity Penetration Studies

4.1 Introduction

The presence of the plasma impurities can affect the plasma in various ways, some of which are detrimental to plasma performance because of the impurities' strong radiating power. Thus it is important to understand the behavior of impurities under various plasma conditions. The ability of the plasma to screen the impurities is one of the behaviors that needs studying.

Studies regarding impurities had been carried out in many tokamaks in the past. In particular, the studies of impurity screening had been carried out in DIIID (diverted plasmas) ([29]) and TEXTOR (limited plasmas) ([30]) through impurity injections. In DIIID, argon and neon were injected through a gas puffing system at various locations. Argon was found to have a penetration rate of the order of 50% ([29]) in DIIID, which was an order of magnitude higher than what was found in Alcator C-Mod . Neon was found to have a penetration rate of around 90% ([31]) and this result was independent of the gas injection locations. Similar investigations were also carried out in TEXTOR in the past several years for limited plasmas. Various impurities, including argon, were used in those studies. While it was found that the argon is 100% recycling, its penetration efficiency is found to be just around 4% (i.e. 4% of the total argon atoms injected were found to reside in the core plasma), comparable to what was found in Alcator C-Mod .

An important question left unanswered from the previous studies of impurity screening is what plasma parameters determine or influence the screening efficiency. Studies were carried out in Alcator C-Mod trying to answer this question.

A major difficulty in studying impurity screening in actual tokamak plasmas is that normally more than one plasma parameter which can potentially affect the screening changes from discharge to discharge or even during a discharge. This makes it difficult to isolate the cause of changes in impurity screening. Great effort has to be made in selecting data of discharges during which only one variable significantly changes.

To study the effect of plasma variables and conditions on impurity screening/penetration, a series of experiments was carried out. Intuitively, plasma geometry, e.g. elongation κ, divertor strike point locations, inner and outer gap, etc, all have potential influence over the impurity penetration. Several experiments were carried out to explore such influence. Results from these experiments are presented in this chapter.

4.2 Impurity Screening Comparison of Diverted and Limited plasmas

Divertors were conceived of as a way of reducing the sputtered and recycled impurity inflow characteristic of limiters. (Ref. [32]) Poloidal divertors are used in the Alcator C-Mod tokamak. External coils carry currents parallel to the plasma current, diverting the poloidal magnetic field and creating magnetic nulls. A magnetic separatrix thus defines the LCFS. Flux surfaces outside the LCFS can be conveyed some distance away from the main plasma to separate divertor chambers. Although divertors may have several other advantages, such as facilitating H-mode and possibly helium pumping, this impurity screening effect is their primary raison d'être. One pays a rather heavy price to include a divertor in a tokamak design — increased magnet complexity, increased vacuum vessel complexity, less efficient use of B-field volume, and severe difficulties with heat removal. Therefore it is necessary to verify experimentally a

divertor's superior impurity screening in comparison to a limiter. Three experiments (C-Mod run 950316, 950519 and 951208) dedicated to such comparison were carried out. During those experiments, plasma elongation was kept at $\kappa = 1.50 - 1.55$, and the plasmas were toggled between limited on the inner wall and diverted, on a shot-to-shot basis. See Figure 2-9 for the comparison of the magnetic geometries between limited and diverted plasmas. During run 950316, experiments were carried out for both topologies at three different densities using the main gas fueling system. During run 950519, experiment was carried out at high density, $\bar{n}_e \sim 2.6 \times 10^{20}$ m^{-3}, also using the main gas fueling system. During run 951208, the experiment was carried out at medium density, $\bar{n}_e \sim 1.5 \times 10^{20}$ m^{-3}, using the NINJA system to inject argon at several locations. These experiments confirmed the advantage of the divertor over the limiter in argon screening. In 950519 and 951208, successful measurements of the edge electron density and temperature profiles were obtained using the Fast Scanning Langmuir Probe.

4.2.1 Experimental Data of Run 950316

During this run, diverted and limited plasmas were studied for three density ranging from $\bar{n}_e \sim 1.2 \times 10^{20}$ m^{-3} to $\bar{n}_e \sim 2.6 \times 10^{20}$ m^{-3}. Plasma current during the flat-top was $800kA$ throughout the run. The plasmas were limited on the inner wall in the limited shots. Argon was injected using 30 ms long pulses with 4 psi plenum pressure (injecting $\sim 10^{18}$ argon atoms) in the diverted shots and using shorter pulses in the limited shots. Figure 4-1 plots the argon penetration $p \equiv \frac{number\ of\ Ar\ atoms\ in\ the\ plasma}{number\ of\ Ar\ atoms\ injected}$ (expressed in percent) of limited and diverted plasmas obtained from HIREX data for three plasma densities. The argon penetration for the limited plasmas is around a factor of 2 of that for the diverted plasmas.

The McPherson spectrograph was also used to measure the argon density in the plasma from lithium-like argon emission. The modeling of the lithium-like argon and scandium are discussed in Section 3.3. The MIST code again provided the fractional abundance of argon ions. As it typically is, the line of sight for the McPherson spectrometer during this run passed near the center of the plasma, as shown in Figure 4-2.
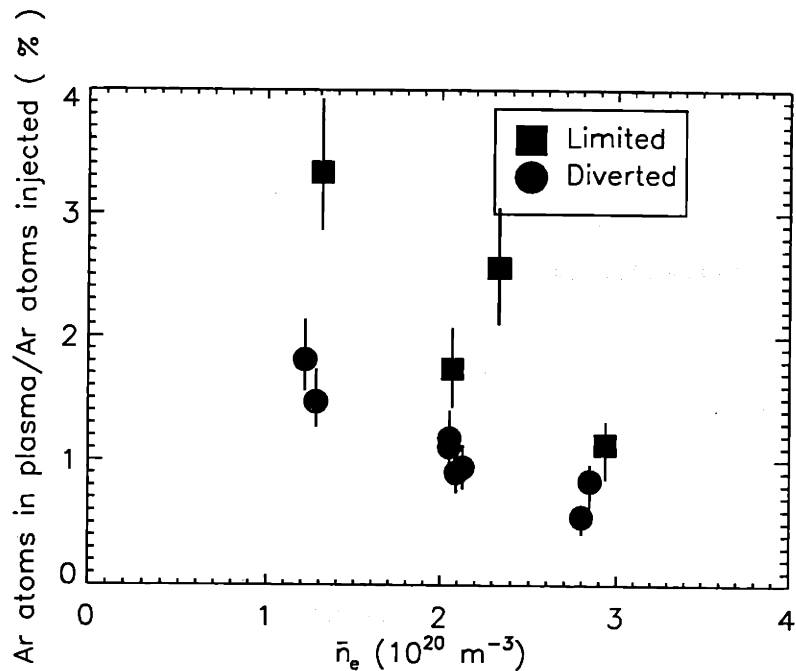
Figure 4-1: Argon penetration comparison between diverted and limited plasmas, obtained by HIREX during Alcator C-Mod run 950316. $I_p = 800\ KA$, $\bar{n}_e$ is in $10^{20}\ m^{-3}$. Solid vertical lines show the error bars.

A code was written to calculate the line-integrated brightness of lithium-like $j = \frac{3}{2}$ line with given T_e and n_e profiles and the MIST argon ion profiles. Line brightness calculated this way was then compared to the line brightness observed through the McPherson Spectrometer. The total argon density used in the MIST calculation was adjusted to equate the two line brightnesses. Figure 4-3 plots the argon penetration obtained from the McPherson data versus the $\bar{n}_e$. The ratio between argon penetration of limited plasmas and that of diverted plasmas was also around 2:1, confirming the HIREX results.

It should be noted that the penetration calculated from the McPherson's data is nearly four times that calculated from the HIREX data. One reason for this may be that HIREX is not absolutely calibrated. Comparison with other diagnostics inferred a factor of two accuracy for the HIREX measurements. The McPherson data also has a factor of two error range. ([33]) The factor of four discrepancy could be accounted for if both measurements gave errors in the same direction. Also, another possible reason was that the lithium-like argon density in the outer region of the plasma was
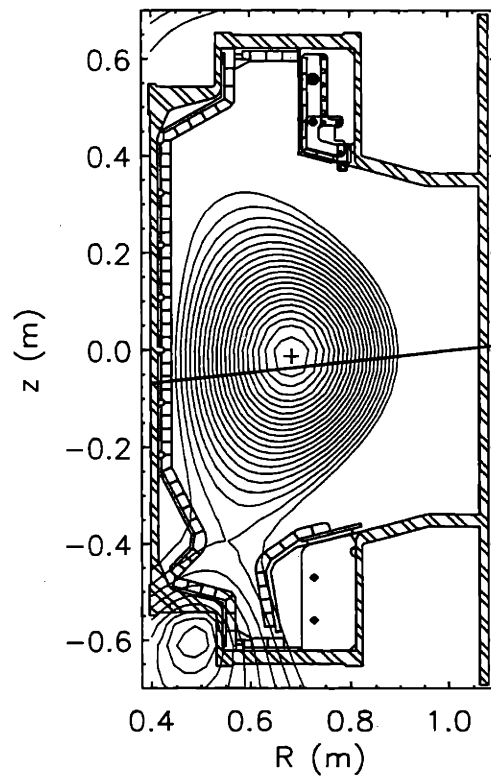
Figure 4-2:   Line of sight of the McPherson spectrometer during Alcator C-Mod run 950316.
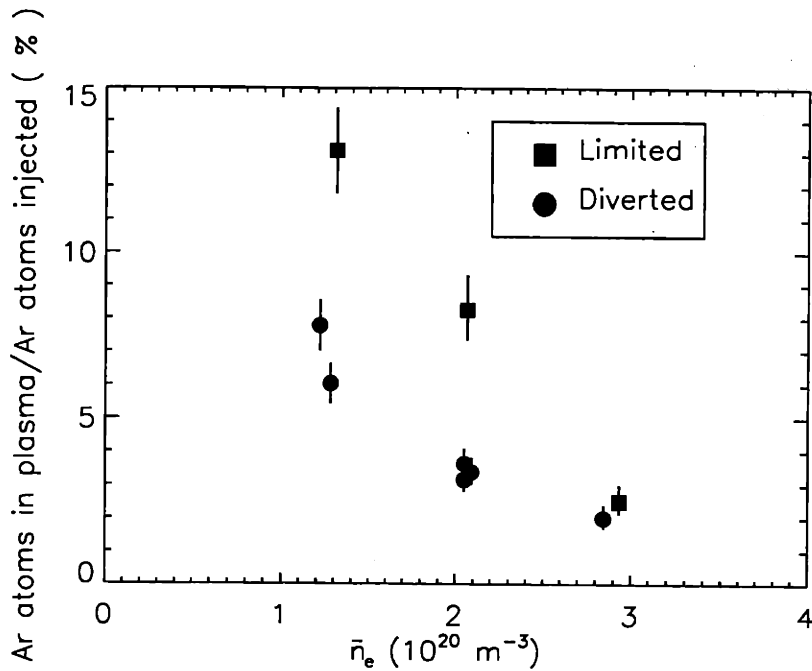
Figure 4-3:   Argon penetration comparison between diverted and limited plasmas, obtained by McPherson Spectrometer during Alcator C-Mod run 950316. $I_p = 800\ KA$, $\bar{n}_e$ is in $10^{20}\ m^{-3}$. Solid vertical lines show the error bars.

higher than that predicted using a spatially constant diffusion coefficient. Evidence provided in Section 5.2.1 suggested that lithium-like argon density in the outer part of the plasma was higher than that predicted by a spatially constant diffusion coefficient. In that case, a factor of 10 difference is suggested. This direction of the discrepancy was consistent with what was suggested by the difference in VUV and HIREX data.

Scandium was also injected during this run using the laser ablation technique to study screening of the non-recycling impurities. Figure 4-4 plots the number of Sc atoms from a series of identical injections that get into the plasma vs. $\bar{n}_e$. It was clear that the screening became better when the density was higher. But the difference of screening between limited and diverted plasmas was significantly smaller than that of argon. This could be partially explained by the fact that some scandium ablated by the laser may enter the scrape-off layer as microscopic particles instead of as separated atoms. ([34]) Therefore a significant number of scandium atoms would penetrate into the core plasma before they were ionized. Thus the difference in screening between limited and diverted plasmas had no effect on at least part of the scandium atoms,
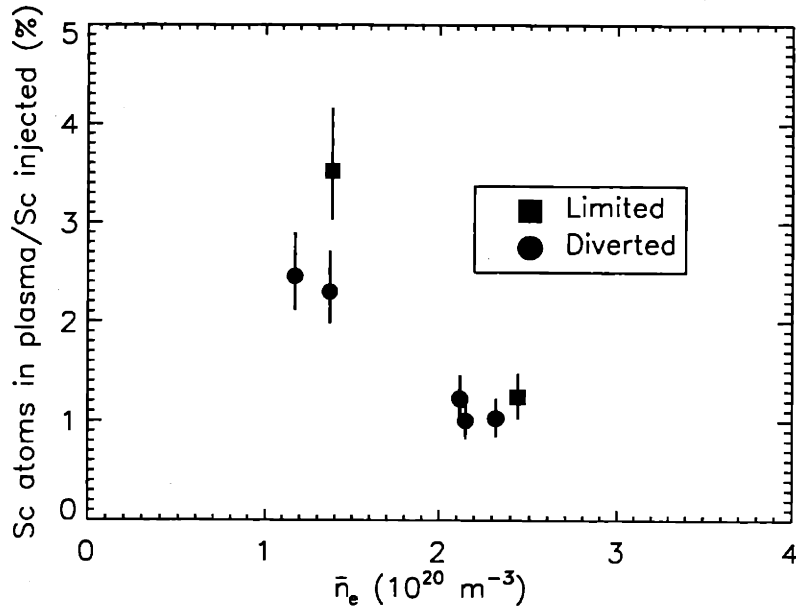
Figure 4-4: The number of scandium atoms in the plasma versus the $\bar{n}_e$. Alcator C-Mod run 950316. $I_p = 800\,kA$. The solid vertical lines show the error bars.

and therefore reduced the difference in total screening.

4.2.2 Modeling of Impurity Penetration.

In an attempt to explain how impurities penetrate into the main plasma, a simple model is developed to correlate the impurity density in the plasma with potentially measurable edge plasma parameters. It is a 1-D model which assumes that all incoming neutral impurity atoms ionized within the SOL are swept into the divertor region and the rest of the neutral impurity atoms enter the main plasma.

For an influx of neutrals with $v_\perp = v\cos\theta$ as the velocity component normal to the SOL layer, the fraction of neutrals penetrate the SOL is:

$$P_{pen} = \exp(-\int_0^{x_0} \frac{n_e \overline{\sigma v_i}}{v_\perp} dx) = \exp(-\int_0^{x_0} \frac{n_e \overline{\sigma v_i}}{v\cos\theta} dx) , \qquad (4.1)$$

where θ is the incident angle and $\overline{\sigma v_i}$ is the first ionization rate coefficient, which is expressed as(see Ref. [35]);

$$\overline{\sigma v_i} = 1.7 \times 10^{-14} \bar{g} \left(\frac{R_y}{\chi_i}\right)^2 \left(\frac{T_e}{R_y}\right)^{1/2} e^{-\frac{\chi_i}{T_e}} \left(1 - e^{-\frac{5\chi_i}{T_e}}\right) \ m^3 s^{-1} . \tag{4.2}$$

Here χ_i is the first ionization energy of the impurity expressed in eV, R_y is the ionization energy of hydrogen (13.6 eV), T_e is in eV, $\bar{g}$ is the average Gaunt factor approximated in Ref. [35] as:

$$\bar{g} = 1 + \frac{\sqrt{3}}{\pi} \ln\left(1 + \frac{T_e}{\chi_i}\right) , \tag{4.3}$$

where x_0 is the location of the LCFS with respect to the edge of the SOL.

Averaging Equation 4.1 over all incident angles and velocities to get total impurity influx at the LCFS for a plasma of surface area A_p surrounded by neutral impurity gas of density n and temperature T_{imp}:

$$\Gamma_{in}(a) = nA_p \int_0^\infty dv \frac{4}{\sqrt{\pi} v_m^3} e^{-v^2/v_m^2} v^3 \int_0^{\frac{\pi}{2}} d\theta \frac{\sin\theta \cos\theta}{2} \exp\left(-\int_0^{x_0} \frac{n_e \overline{\sigma v_i}}{v \cos\theta} dx\right) , \tag{4.4}$$

where $v_m = \sqrt{\frac{2kT_{imp}}{m}}$ is the most probable velocity of a gas of Maxwellian distribution with a temperature of T_{imp}, a is the minor radius at the LCFS. A_p is the total plasma area. n is the number density of the neutral impurity gas. Some evidence suggest that T_{imp} is higher than the room temperature. Discussion about this is presented in Appendix D.

In this 1-D model, it is assumed that the gaseous impurities fill the whole volume in the vacuum chamber outside of the plasma in the form of neutral atoms. Also, the impurity gas is assumed to have a constant density everywhere outside of the plasma. Therefore:

$$n = \frac{N}{V_{tot} - V_p} , \tag{4.5}$$

where N is the total number of impurity atoms existing outside of the plasma in the form of neutral gas. If wall pumping is ignored and only a small percentage of the impurity gets into the plasma, then N is effectively the same as the total number of the injected impurity atoms N_{inj}. V_{tot} is the total volume of the vacuum chamber and V_p is the plasma volume.

Thus the total impurity influx is given as:

$$\Gamma_{in}(a) = \frac{N}{V_{tot} - V_p} A_p \int_0^\infty dv \frac{4}{\sqrt{\pi} v_m^3} e^{-v^2/v_m^2} v^3 \int_0^{\frac{\pi}{2}} d\theta \frac{\sin\theta \cos\theta}{2} \exp(-\int_0^{x_0} \frac{n_e \overline{\sigma v_i}}{v \cos\theta} dx) .$$

(4.6)

Assuming the perpendicular diffusion coefficient at the LCFS is the same as the anomalous diffusion coefficient $D_\perp$ throughout most of the plasma, and assuming zero convection for the sake of simplicity, the total outflux of the impurity ions $\Gamma_{out}(a)$ is given as;

$$\Gamma_{out}(a) = A_p D_\perp \nabla n_{imp}(a) \approx A_p D_\perp n_{imp}(a)/\lambda_{SOL} , \qquad (4.7)$$

where n_{imp} is the impurity density in the plasma and $n_{imp}(a)$ is the impurity density at the LCFS. λ_{SOL} is the characteristic decay length of impurities in the SOL.

When convection is ignored, and if $D_\perp = constant$, the radial profile of the impurity density consists of a region of constant density to the edge and a falling profile beyond it. In this case,

$$\lambda_{SOL} \approx \lambda_{iza} , \qquad (4.8)$$

where the mean free path of the ionization λ_{iza} is approximated by:

$$\lambda_{iza} = v_0/\overline{\sigma v_i}(a) n_e(a) , \qquad (4.9)$$

where v_0 is the average velocity of the neutral impurity influx. If the impurity is a gas at temperature T_{imp}, v_0 is given by:

$$v_0 = (\frac{8KT_{imp}}{\pi m})^{\frac{1}{2}} . \qquad (4.10)$$

In steady state, across the LCFS the total impurity outflux Γ_{out} must equal the total impurity influx Γ_{in}:

$$\Gamma_{out}(a) = \Gamma_{in}(a) . \qquad (4.11)$$

Substituting Equation 4.6 and 4.7 back to 4.11;

$$A_p D_\perp n_{imp} \frac{\overline{\sigma v_i}(a) n_e(a)}{v_0} = \frac{N}{V_{tot} - V_p} A_p \int_0^\infty dv \frac{4}{\sqrt{\pi} v_m^3} e^{-v^2/v_m^2} v^3 \int_0^{\frac{\pi}{2}} d\theta \frac{\sin\theta \cos\theta}{2} \exp\left(-\int_0^{x_0} \frac{n_e \overline{\sigma v_i}}{v\cos\theta} dx\right) .$$

(4.12)

From Equation 4.12, the impurity density at the LCFS is given as;

$$n_{imp}(a) = \frac{N}{(V_{tot} - V_p) D_\perp} \frac{v_0}{\overline{\sigma v_i}(a) n_e(a)} \int_0^\infty dv \frac{4}{\sqrt{\pi} v_m^3} e^{-v^2/v_m^2} v^3 \int_0^{\frac{\pi}{2}} d\theta \frac{\sin\theta \cos\theta}{2} \exp\left(-\int_0^{x_0} \frac{n_e \overline{\sigma v_i}}{v\cos\theta} dx\right) .$$

(4.13)

For such a model, ignoring convection, the impurity density at the LCFS is a good approximation of the central impurity density. For argon, it turns out that a very small percentage (several percent) of the injected atoms are in the plasma, implying that $N \simeq N_{inj}$. Thus find the relation:

$$p \equiv \frac{number\ of\ Ar\ atoms\ in\ the\ plasma}{number\ of\ Ar\ atoms\ injected} = \frac{n_{imp} V_p}{N_{inj}}$$

$$\simeq \frac{V_p}{(V_{tot}-V_p) D_\perp} \frac{v_0}{\overline{\sigma v_i} n_e(a)} \int_0^\infty dv \frac{4}{\sqrt{\pi} v_m^3} e^{-v^2/v_m^2} v^3 \int_0^{\frac{\pi}{2}} d\theta \frac{\sin\theta \cos\theta}{2} \exp\left(-\int_0^{x_0} \frac{n_e \overline{\sigma v_i}}{v\cos\theta} dx\right) . (4.14)$$

A crude test was done to qualitatively support this model. See Appendix D for detailed discussion.

4.2.3   Experimental Data of Run 950519 and Run 951208

In run 950519, argon was injected using the B-side lower pulsed valve. The time histories of the central argon density (obtained using method described in Section 3.5) of a limited shot and a diverted shot, both of which had an 30 ms argon pulse starting at 0.5 s, are presented in Figure 4-5. The central argon density of the limited shots was about twice as high as the diverted shot, indicating a better screening ability of the divertor configuration.

In run 951208, argon was injected through the NINJA system in order to explore the impact of different puffing locations. Also a series of successful Fast Scanning Probe measurements of the edge electron temperature and density profile were carried
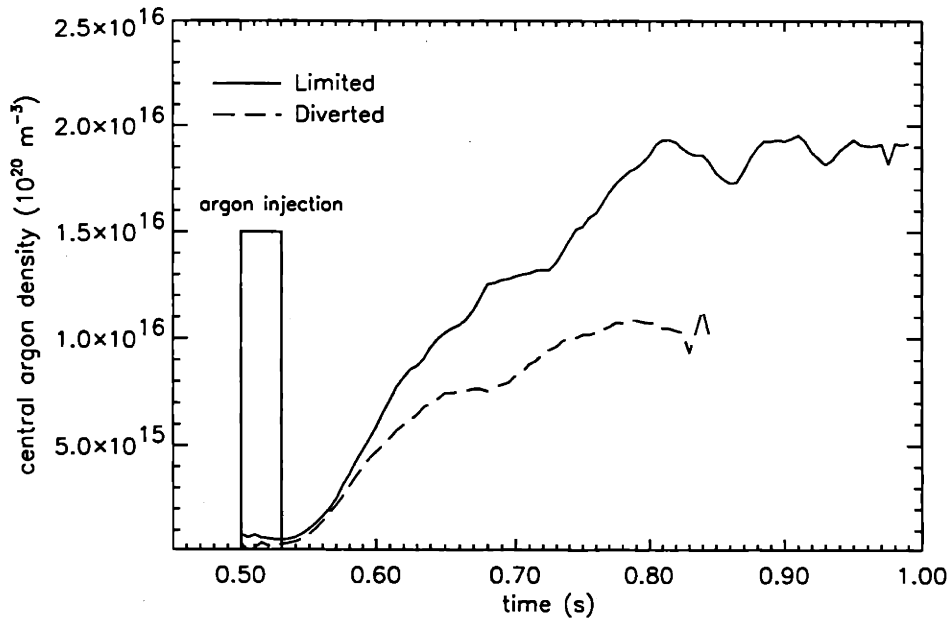
Figure 4-5: Time histories of the central argon density of a limited and a diverted discharge during run 950519. Also shown is the argon injection pulse.

out. Due to low conductance of the capillary tubes used in the NINJA system to inject gas, it usually takes longer than a discharge for the impurity gas to enter the vacuum chamber completely. Therefore identical injections were made at -0.3 s for 300 ms for different shots and the time history of the central argon density were used to study the limiter-versus-divertor problem. Figure 4-6 shows the argon density for argon injections from various locations for both limited and diverted shots. It is obvious that the diverted shots are much better at impurity screening than the limited ones. Argon densities in the limited shots are an order of magnitude higher than that in the diverted shots.

To explain such difference between the diverted and the limited plasmas, one has to study the screening mechanism. When the simple penetration/screening model was developed in Section 4.2.2, it was assumed that the screening depended entirely on the electron density and temperature profiles in the SOL, but not on where the gas was injected. This would imply that shots in which the same amount gas was injected at different locations should have the same impurity density in the core plasma, as long as their SOL structures were similar, i.e. they were of similar magnetic geometry.

81
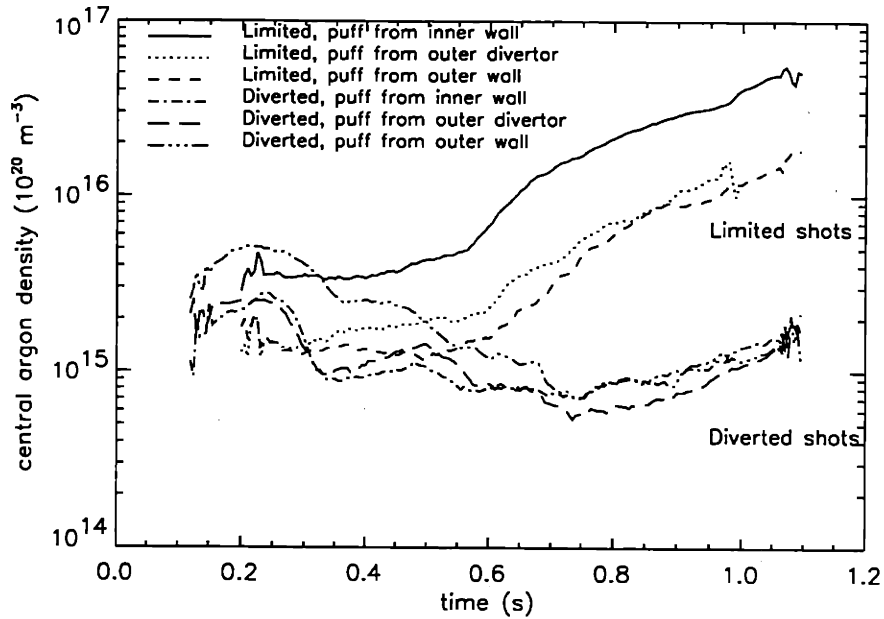
Figure 4-6: Time histories of the central argon density of limited and diverted discharges during run 951208.

This was indeed the case for the diverted and the limited shots, respectively. The experimental observations was consistent with the model.

Since the electron temperature and density profiles play an essential role in impurity screening, the Fast Scanning Probe (FSP) data were analyzed. This two runs were separated by a major maintenance period. It was found that the impurity screening was better for the later. Otherwise the conditions in those two runs were similar, both of which were ohmic, $B_T = 5.3T$ and $I_p = 800 \ kA$. Elongation of the diverted shots in both runs were between 1.6 and 1.7. For the limited shots in both runs the elongation were around 1.3. One important difference of the two runs, however, was that run 950519 was of higher density, $\bar{n}_e \approx 2.6 \times 10^{20} \ m^{-3}$, and run 951208 was of medium density, $\bar{n}_e \approx 1.5 \times 10^{20} \ m^{-3}$. Figure 4-7 plots the typical FSP data for the diverted and the limited shots in both runs. It shows that the both the electron temperature and density were higher in the diverted shots than in the limited shots. The model suggests that this is the reason why diverted plasmas are better at impurity screening. Higher edge electron density and temperature means that more neutral impurity atoms are ionized within the SOL and fewer can enter the core plasma.
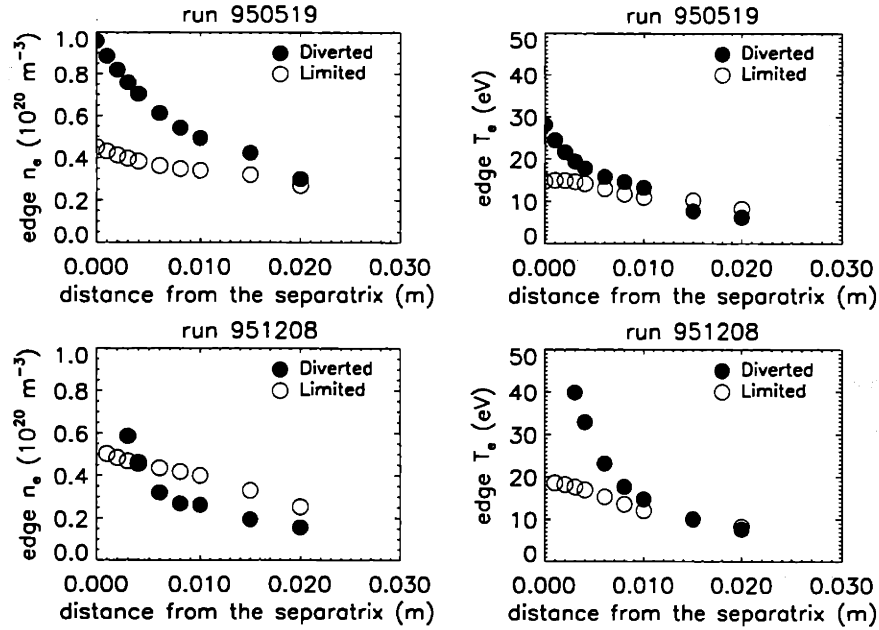
Figure 4-7: FSP data for typical diverted and limited shots in run 950519 and run 951208. For run 950519, $\bar{n}_e \approx 2.6 \times 10^{20}\ m^{-3}$. For run 951208, $\bar{n}_e \approx 1.5 \times 10^{20}\ m^{-3}$

The FSP data were then used as input to Equation 4.14 to calculate the argon penetration $p \equiv \frac{number\ of\ Ar\ atoms\ in\ the\ plasma}{number\ of\ Ar\ atoms\ injected}$. Other parameters assumed are: $D_\perp = 0.5\ m^2 s^{-1}$; $\lambda_n = 0.005\ m$. For each run day, T_{imp} was deduced by adjusting its value to fit the argon penetration calculated from HIREX data for a shot in which argon was inject through the B-side lower valve and use that T_{imp} in calculating p for other shots of the run day. Error analysis was done by varying the electron temperature and density profiles to their maximum error ranges both in magnitude (10%) and in radial coordinates (1 mm). Figure 4-8 and Figure 4-9 shows the range of p for limited and diverted plasmas. It predicts better screening for the diverted plasma than for the limited plasma. This was consistent with the experimental observations.

4.3 Effect of Divertor Target Plate Strike Point Location on Impurity screening

The locations of the places (called strike points) where the magnetic field lines connecting the LCFS through the magnetic null hit the target plate categorize the diver-
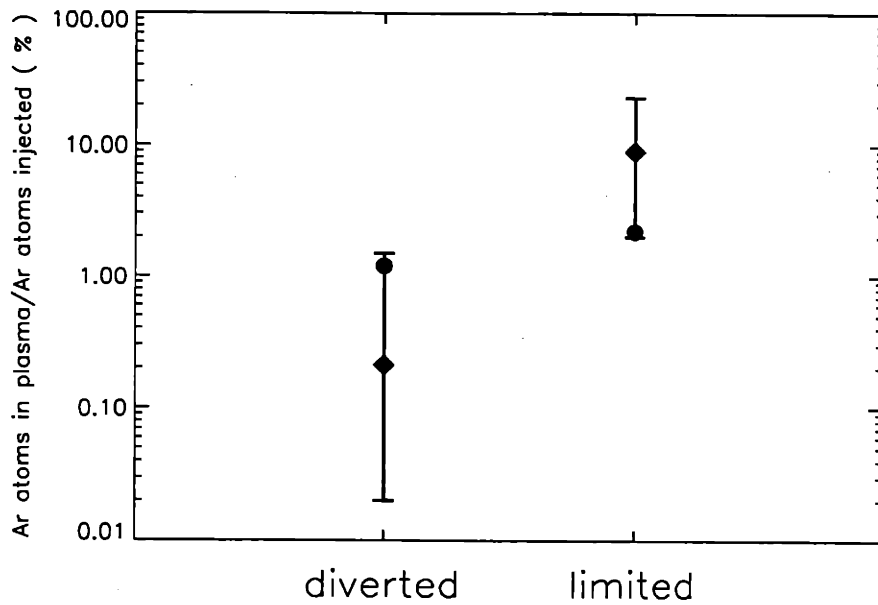
Figure 4-8:   Penetration predicted by the penetration model and FSP data of the $\bar{n}_e \approx$ $2.6 \times 10^{20} \ m^{-3}$ run. The vertical lines show the error bars. The solid dots show the experimental points. The solid diamonds show the results calculated directly from FSP data.
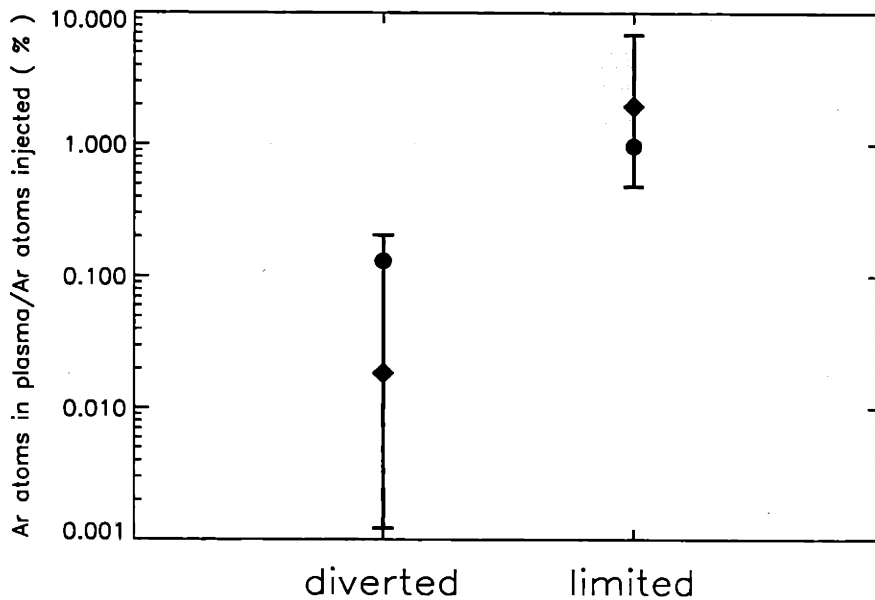
Figure 4-9:   Penetration predicted by the penetration model and FSP data of the $\bar{n}_e \approx$ $1.5 \times 10^{20} \ m^{-3}$ run. The vertical lines show the error bars. The solid dots show the experimental points. The solid diamonds show the results calculated directly from FSP data.

tor configurations into open, closed and slot divertor. See Figure 4-10 for illustrations of each configuration. The divertor configuration can be obtained using the magnetic geometry measurements and the EFIT code.

standard closed divertor   open divertor   slot divertor
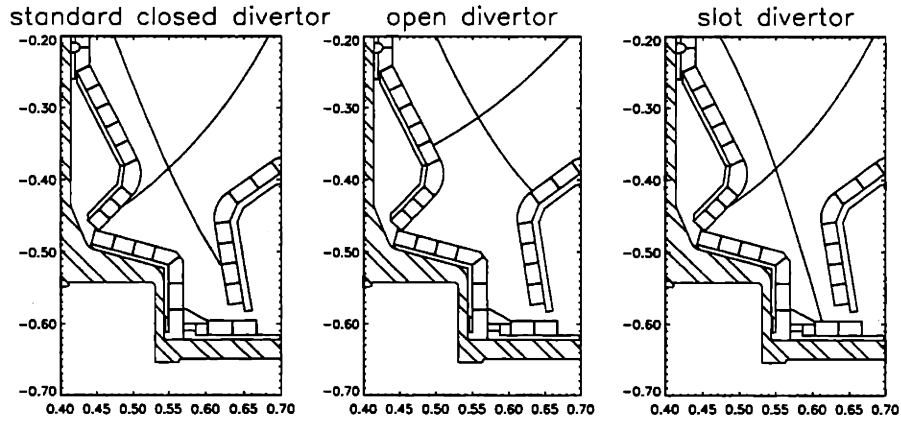
Figure 4-10: Various divertor configurations. The X and Y axis show the dimensions of the divertor in meters.

During several experiments, the strike points were scanned while other plasma parameters were held as steady as possible. The argon penetration results from the strike point scan are presented in this section. Figure 4-11 shows the flux plots of some shots with different strike points locations.

Figure 4-12 and 4-13 plot the argon penetration versus the vertical coordinates of the outer and inner divertor strike points of some discharges of various densities. The combined range of the scans at three densities covered the whole length of the divertor plate. (See Figure 4-10 for the dimension of Alcator C-Mod divertor) For one density the strike points were scanned on the lower half of the outer divertor target plate. On one discharge the outer divertor strike point was located on the floor of the divertor, making the configuration a slot divertor. Figure 4-12 and 4-13 indicate that impurity screening was independent of divertor strike point positions for diverted plasmas.

Scanning probe measurement of the edge electron density and temperature profiles were successfully carried out in the divertor strike points scan experiment. Figure 4-14 shows the edge electron temperature and density profiles obtained with FSP. It shows that there were not significant difference between edge electron density and
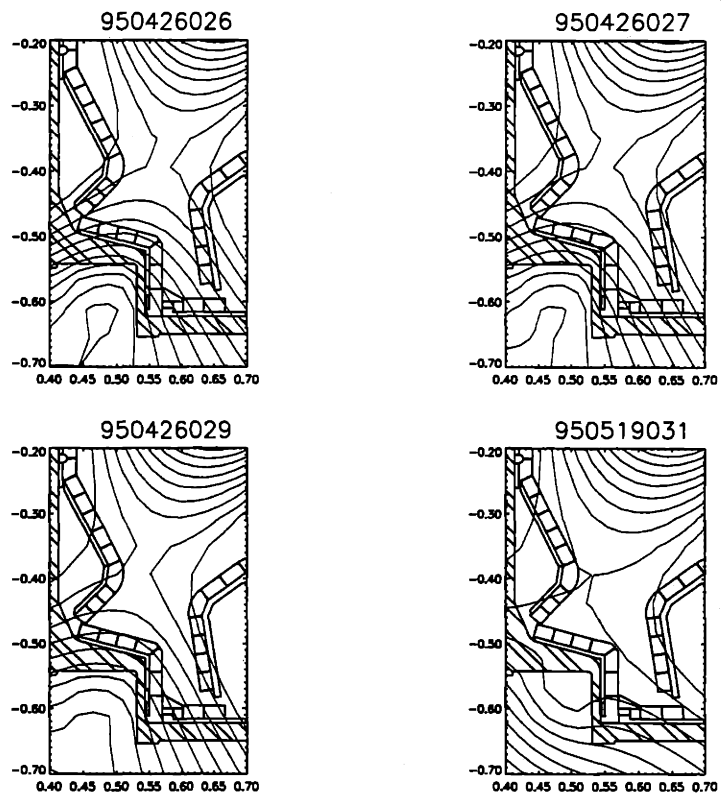
Figure 4-11: Flux plots for discharges with different strike point locations. Flux surfaces were taken from the EFIT calculations.
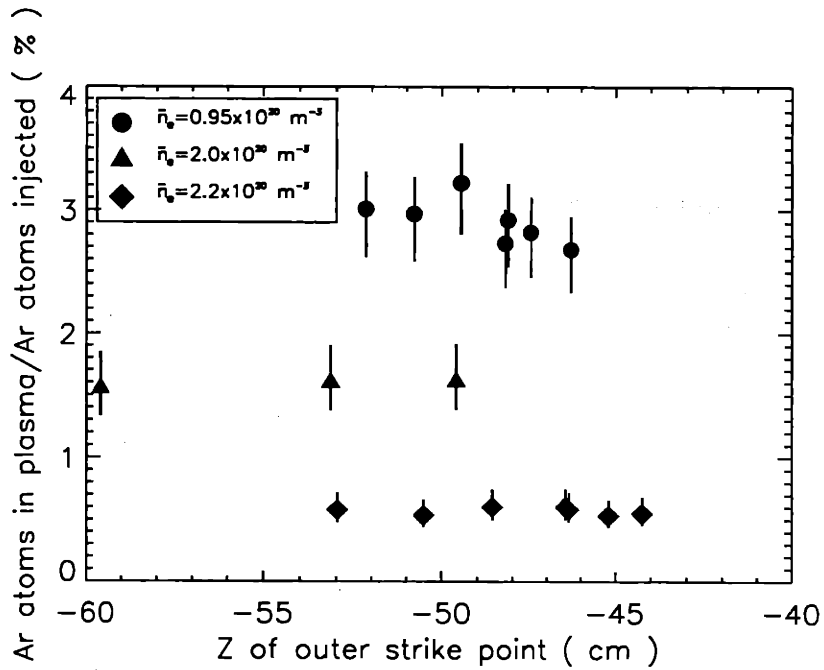
Figure 4-12: Argon impurity penetration versus the vertical (z) coordinates of the outer divertor target plate strike points for Alcator C-Mod run 950426 and 950519. Solid vertical lines show the error bar.
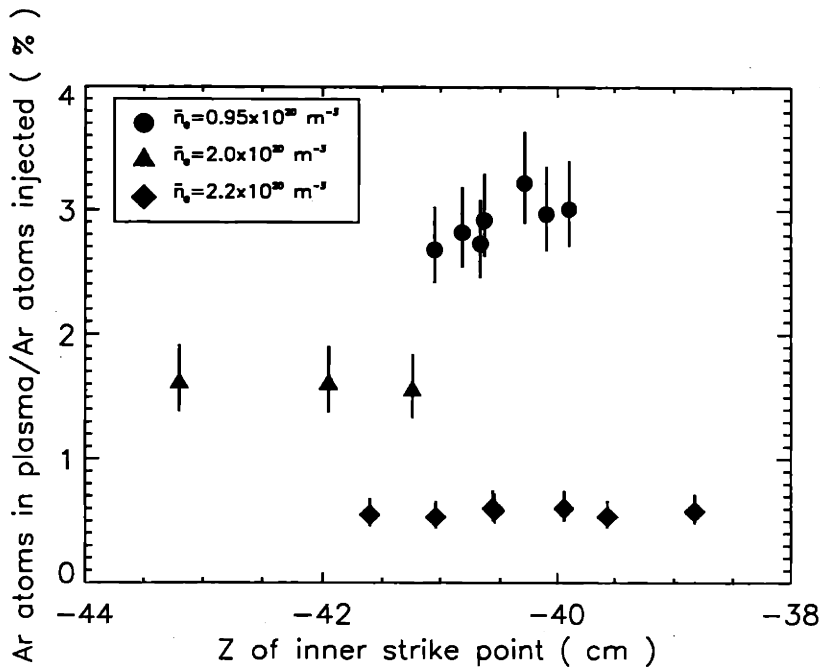
Figure 4-13: Argon impurity penetration versus the vertical (z) coordinates of the inner divertor target plate strike points for Alcator C-Mod run 950426 and 950519. Solid vertical lines show the error bar.

temperature profiles of shots of different divertor strike point locations. The model in Section 4.2.2 then predicts the argon penetration should be essentially the same for those shots. This is consistent with the experimental observation shown in Figure 4-12 and 4-13.
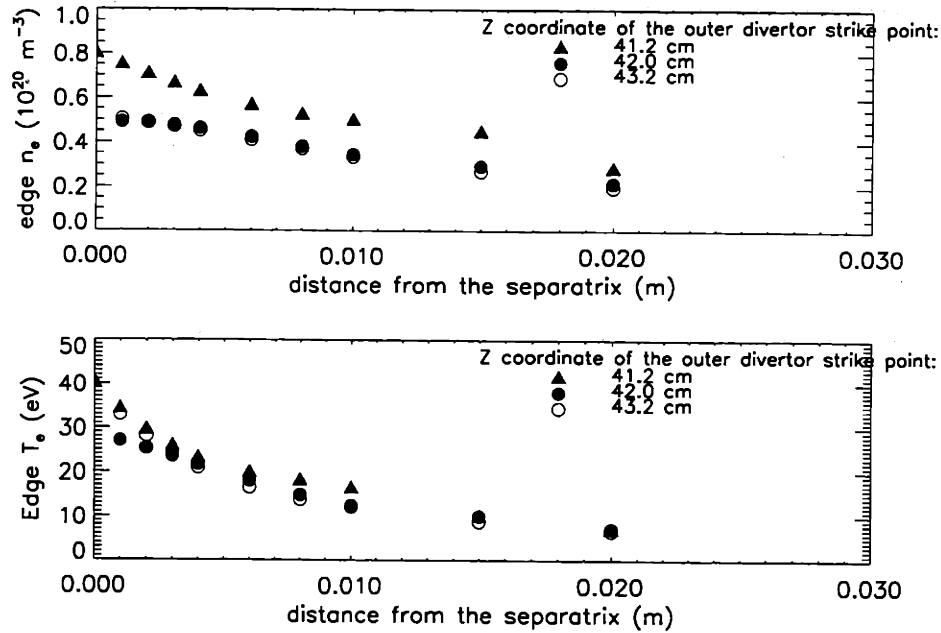
Figure 4-14: Edge electron temperature and density profiles for the divertor strike points scan shots.

4.4   Effect of κ on Impurity screening

No dedicated plasma elongation (κ) scan for the diverted plasmas was carried out in Alcator C-Mod , but a dedicated κ scan for the limited plasmas was done. Even though the limited plasmas may behave differently compared to the diverted plasmas, this experiment still offered information on which speculation about the κ dependence of the diverted plasmas could be made. κ scan were done for two densities at $I_p = 500$ kA. Figure 4-15 and Figure 4-16 show the results for κ scans for low density, $\bar{n}_e \simeq 5 \times 10^{19}$ m^{-3}, and medium densities, $\bar{n}_e \simeq 1.3 \times 10^{20}$ m^{-3}, respectively.

For the medium density case (Figure 4-16), argon penetration had no dependence on κ. Even for the low density case, which seemingly demonstrated a monotonic
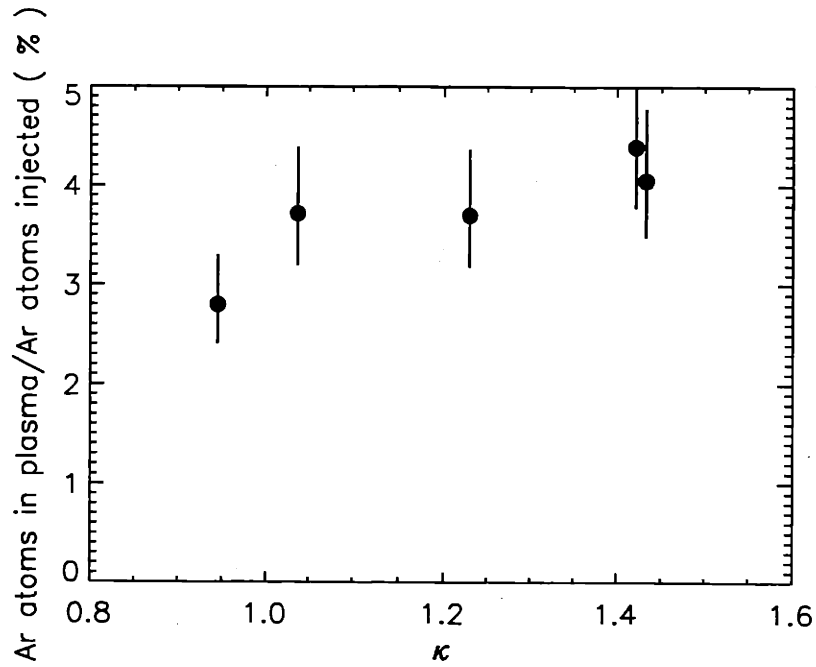
Figure 4-15: κ scan for low density limited plasmas in Alcator C-Mod run 950606. $I_p = 500\,kA$. $\bar{n}_e \simeq 5 \times 10^{19}\,m^{-3}$

dependence, the dependence was not strong enough to necessitate the inclusion of κ as a variable in scaling studies. The reason for this was that the argon penetration only changes by a factor of 20% (a relatively small amount) when κ varies from 0.9 to > 1.4, which covers most of the κ range in Alcator C-Mod operation (Alcator C-Mod plasmas normally have $\kappa < 1.6$). For limited plasmas, at least, the argon penetration had no more than a weak dependence on κ.

4.5 Effect of the Outer Gap on Impurity Screening

During one experiment, the plasma outer gap was varied by moving the plasma centroid while keeping the inner gap fixed. All other plasma parameters were kept fixed as nearly as possible. $\bar{n}_e \simeq 2.0 \times 10^{20}\,m^{-3}$; $\kappa \simeq 1.7$; $I_p = 800\,kA$. The outer gap was varied from 0.7 cm to 2.3 cm. This almost covers the whole possible outer gap range for Alcator C-Mod plasmas.
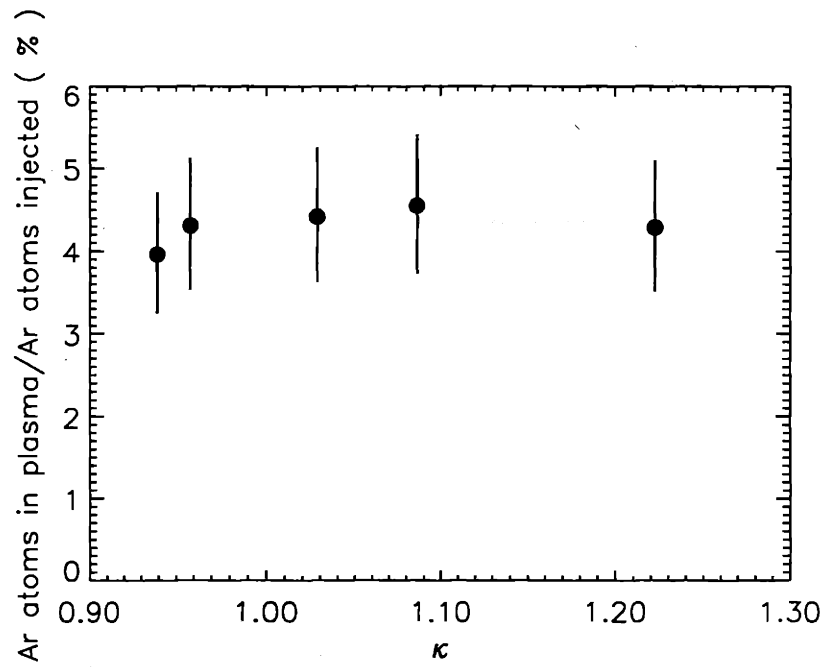
Figure 4-16: κ scan for medium density limited plasmas in Alcator C-Mod run 950606. $I_p = 500\ kA.$ $\bar{n}_e \simeq 1.3 \times 10^{20}\ m^{-3}$
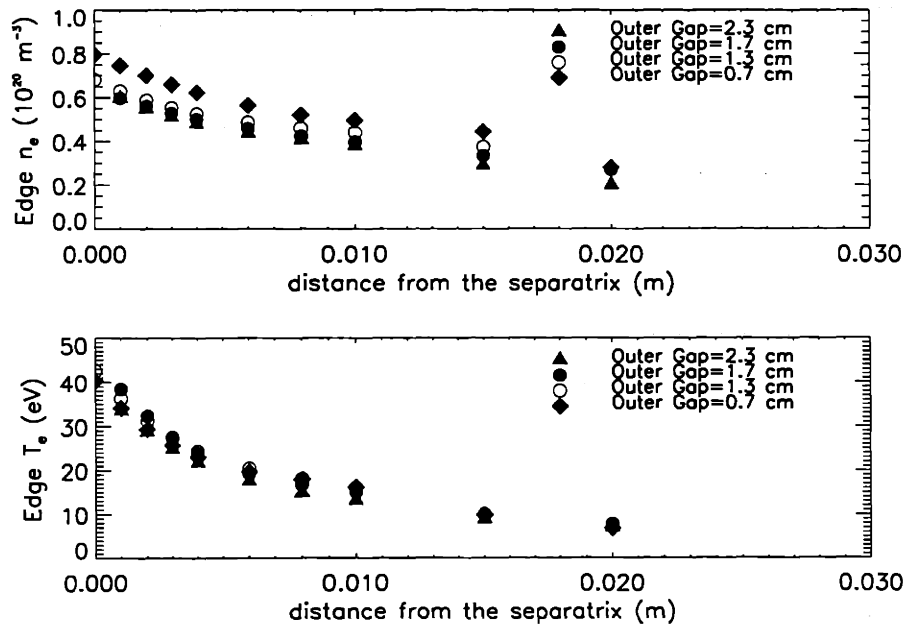
Figure 4-17: Edge electron temperature and density profiles for the outer gap scan shots.

Figure 4-17 shows the edge electron temperature and density profiles obtained with FSP. It shows that there are not significant difference between edge electron density and temperature profiles of shots of different outer gap. According to the model in Section 4.2.2, the argon penetration should be essentially the same for those shots. Figure 4-18 shows that this was indeed the case. It shows that the argon penetration p was independent of the outer gaps (expressed in cm), consistent with the model's prediction.
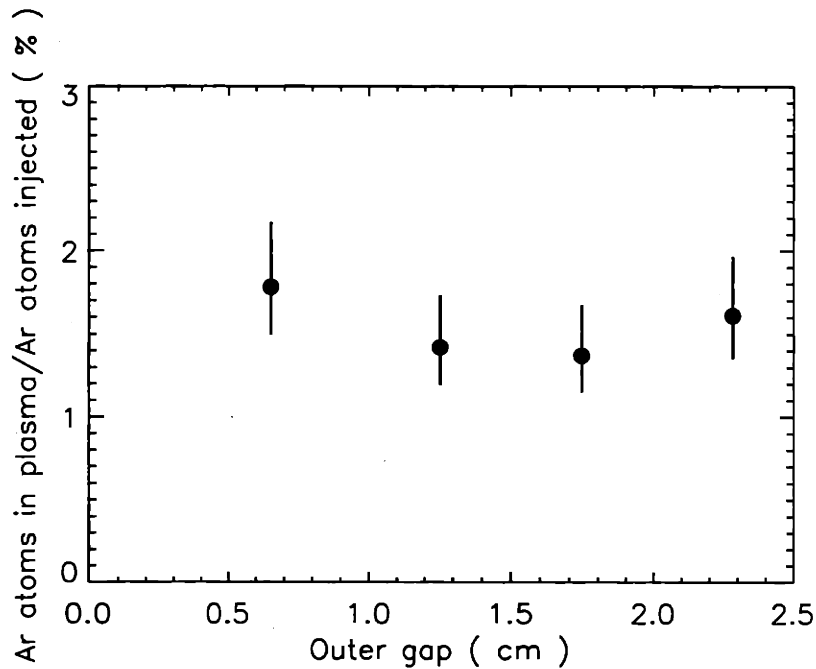
Figure 4-18: Argon impurity penetration versus outer gap. The solid vertical lines show the error bars.

4.6 Effects of ICRF Heating on Impurity screening

Data from ICRF heating experiments were analyzed in search of its effect on the impurity screening. During Alcator C-Mod run 950502, the electron density was kept constant during the ICRF pulses, whose power ranged from 1.25 MW to 2 MW, while the electron temperature increased. The ohmic power ranged from 1 MW to 1.5 MW. Figure 4-19 shows the time histories of one of the discharges during this

91
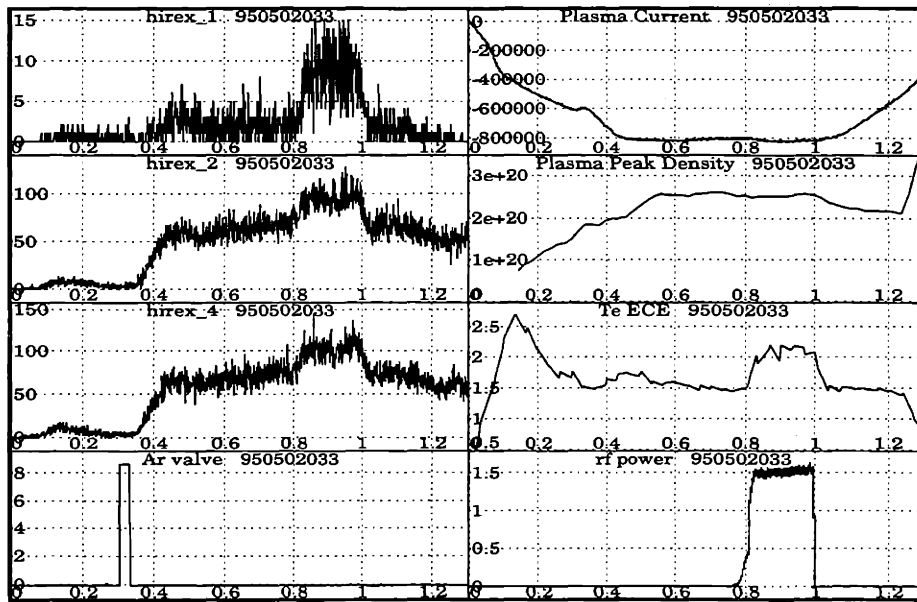
Figure 4-19: Time histories of various plasma parameters and x-ray signals in the Alcator C-Mod ICRF heating experiment. HIREX_2 is spectrometer #2, with which the argon density is measured.

run. Figure 4-20 plots the time history of the central argon density. It shows that the ICRF heating, though it increased the intensity of the x-ray emission, did so primarily by increasing the electron temperature, not by increasing the impurity penetration into the plasma. In less well-controlled ICRF experiments, the electron density as well as the electron temperature changed during the ICRF pulses. In such cases, the impurity penetration did change. But when the data for Ohmic plasmas and for the L-mode ICRF plasmas are plotted versus $\bar{n}_e$, they show no scaling difference between these two heating modes. Figure 4-21 plots the data from another experiment.

4.7 Argon Penetration Scaling for Alcator C-Mod Diverted Plasmas

The study of the argon penetration scaling was carried out during the Alcator C-Mod operation period between November 1994 and June 1995. By carefully selecting plasma discharges in which n_e is the only variable that changes significantly, an em-
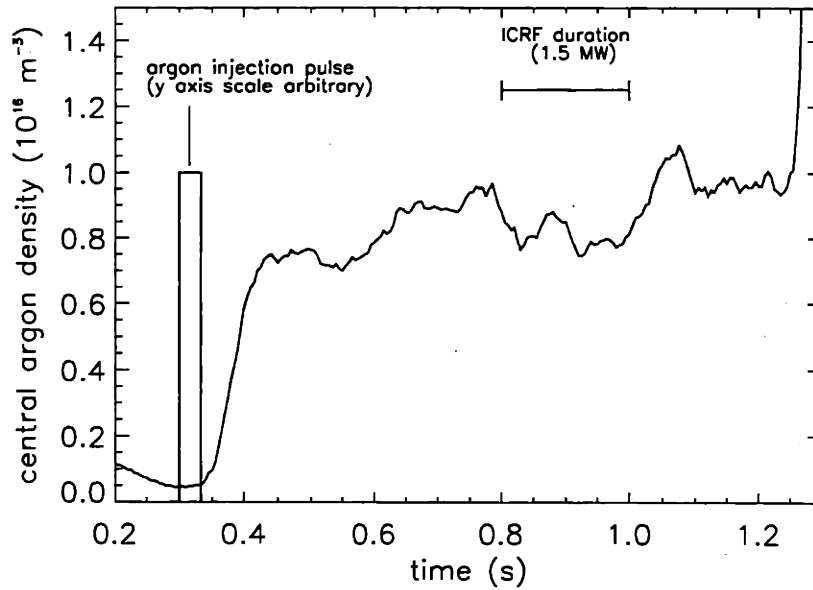
Figure 4-20: Time history of the central argon density for Alcator C-Mod discharge 950502033. The duration of the ICRF heating pulse is also shown.
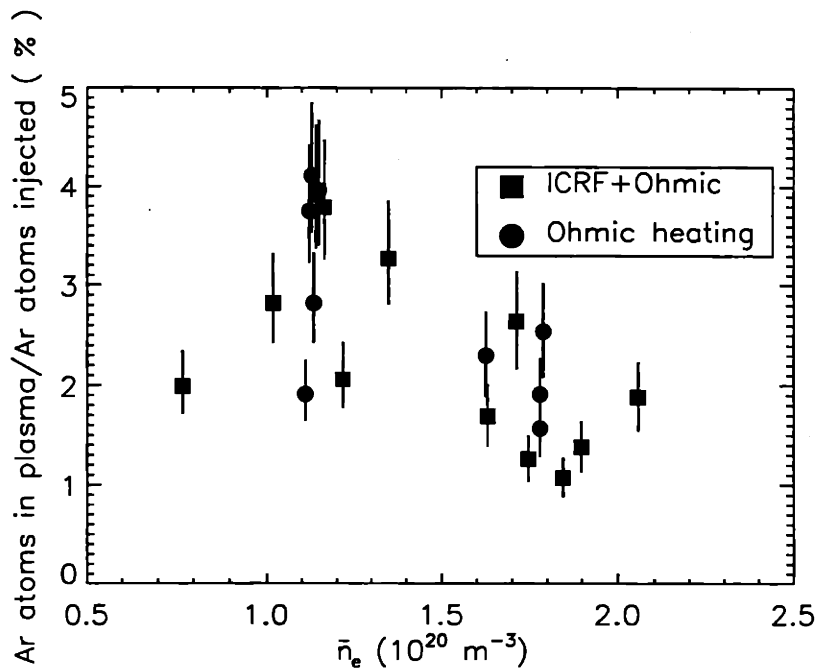
Figure 4-21: Argon penetration for Ohmic heated only plasmas and Ohmic+RF heated plasmas versus $\bar{n}_e$. RF power ranged from 1 MW to 2 MW were applied. Error bars are represented by solid vertical lines.

pirical scaling of the argon penetration/screening was obtained for Alcator C-Mod diverted plasmas.

$$p = \frac{2.1}{\bar{n}_e} , \qquad (4.15)$$

where $p \equiv \frac{number\ of\ Ar\ atoms\ in\ the\ plasma}{number\ of\ Ar\ atoms\ injected}$ is the argon penetration in %. $\bar{n}_e$ is the line averaged density divided by $10^{20}\ m^{-3}$.

Figure 4-22 shows the dependence of p on $1/\bar{n}_e$ for discharges during run 950316. It is a replot of Figure 4-1, with the x-axis changed from $\bar{n}_e$ to $1/\bar{n}_e$. A linear relation between p and $1/\bar{n}_e$ is apparent. The solid straight line plots the p values given by the scaling Equation 4.15.
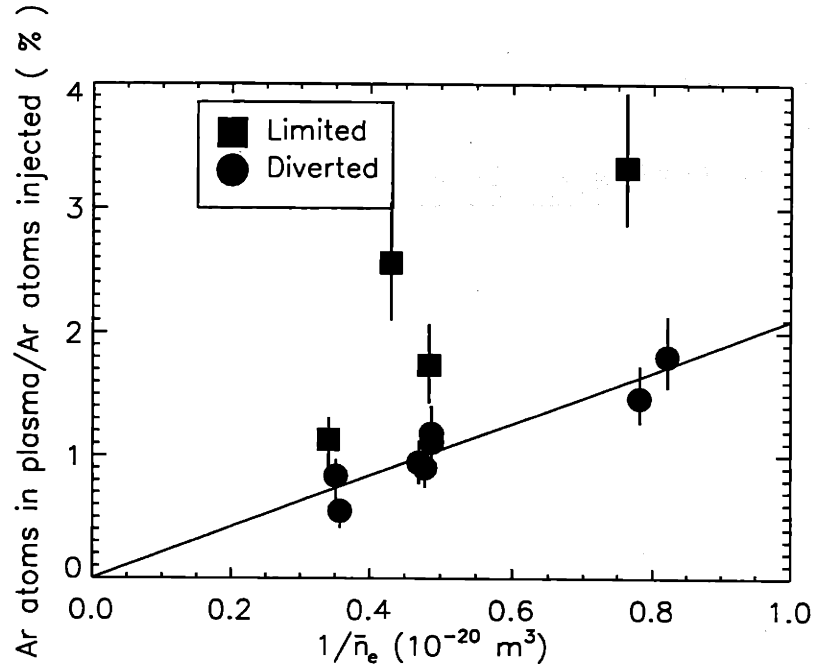
Figure 4-22: Argon penetration scaling versus $\bar{n}_e$. Alcator C-Mod run 950316. $I_p = 800\ KA$. Solid vertical lines show the error bars.

Figure 4-23 plots data from three similar Alcator C-Mod runs (all diverted, ohmic and $I_p = 800KA$) obtained using HIREX data. Again, the solid straight line plots the p values predicted by scaling $p = \frac{2.1}{\bar{n}_e}$. Also plotted is the dependence of p on $\bar{n}_e$ predicted by the penetration model in Section 4.2.2. Edge parameter scaling with respect of $\bar{n}_e$ can be found for C-Mod. (Ref. [20]) In this thesis, scaling with the

same form but different coefficients were used in order to fit the FSP-measured edge electron density and temperature profiles better. The scaling used were:

$$n_e^{separatrix} = 0.4(\bar{n}_e - 0.6) + 0.2 \ ,$$

$$\lambda_n = 7.0(\frac{\bar{n}_e}{I_p} - 1.0) + 4.9 \ ,$$

$$T_e^{separatrix} = -10.7(\frac{\bar{n}_e}{I_p} - 1.0) + 53. \ ,$$

$$\lambda_T = 2.9(\frac{\bar{n}_e}{I_p} - 1.0) + 6.3 \ , \tag{4.16}$$

where $n_e^{separatrix}$ and $\bar{n}_e$ are in $10^{20}m^{-3}$; I_p is in MA; $T_e^{separatrix}$ is in eV; λ_n and λ_T are the e-folding widths of the density and temperature, respectively, in the scrape-off layer, and they are both in mm.
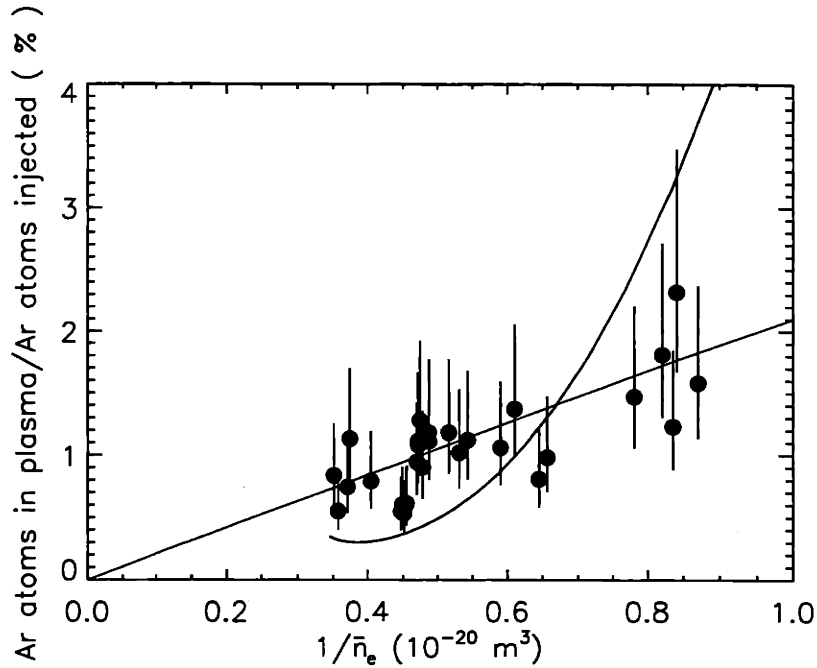
Figure 4-23: Argon penetration scaling versus $1/\bar{n}_e$. $I_p = 800 \ KA$. The solid vertical lines show the error bars. The sloped solid straight line shows the scaling $p = \frac{2.1}{\bar{n}_e}$. The curved solid line shows the scaling obtained by applying the penetration model and edge parameter scaling.

The inverse dependance of p on $\bar{n}_e$ is contradictory to an earlier study on argon conducted also in Alcator C-Mod , which shows no dependance of argon p on the electron density ([20]). However, this result is consistent with the result from an

earlier study of the laser ablated scandium ([20]). This suggests that the earlier experiment with argon might have less well controlled experimental conditions.

Also it should be noted that Alcator C-Mod tokamak's impurity screening capability has been observed to improve on a run period to run period basis. So the constant in Equation 4.15 would not be the same for other run periods.

4.8 Impurity Screening during the H-mode

Since its discovery on ASDEX tokamak in 1982, the H-mode remains the interest of the fusion community. During the H-mode, the particle confinement time also increase substantially, resulting impurity accumulation which may adversely affect the plasma. Thus it is necessary to study the impurity screening characteristics of the H-mode plasmas. Argon was injected during the H-mode to study the screening characteristics of the H-mode. The proper transport coefficients were obtained by the scandium injection experiment. The process of obtaining the transport coefficients is discussed in detail in Chapter 5.
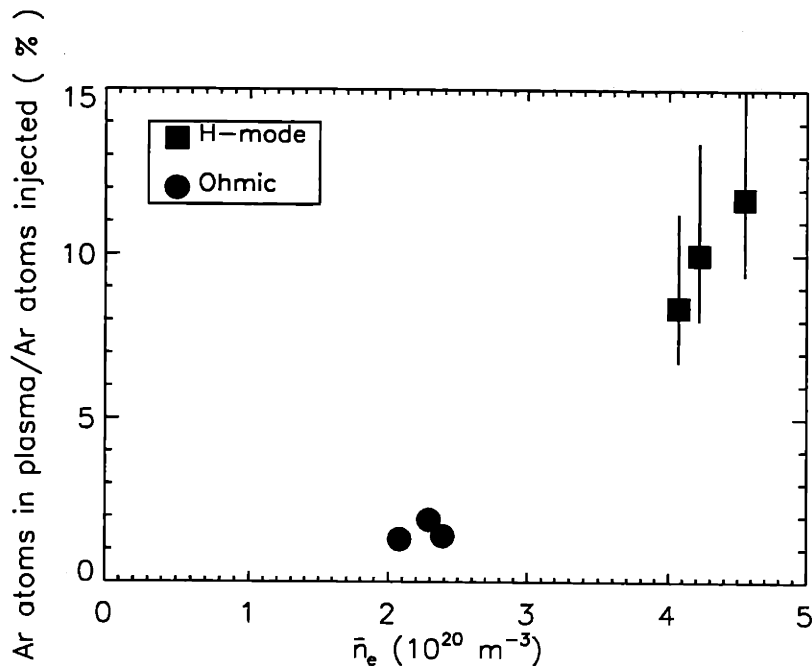
Figure 4-24: Argon penetration comparison before and during the H-mode. Vertical solid lines show the error bars.

The impurity penetration was found to be substantially higher during the H-mode than in the Ohmic plasma. Figure 4-24 shows the argon penetration before and during the H-mode. It shows that the H-mode penetration was over a factor of 5 higher than the ohmic one.

Laser blow-off scandium injections also confirm that there were much more impurities in the plasma during the H-mode. Figure 4-25 shows the helium-like scandium X-ray time histories of two nearly identical injections. The solid line is the H-mode time history. The dotted line is the L-mode one. The H-mode signals not only show that the confinement time is much longer in the H-mode than in the L-mode, also they show nearly an order of magnitude increased in intensity over the L-mode. This is consistent with the findings from the argon injection experiment.
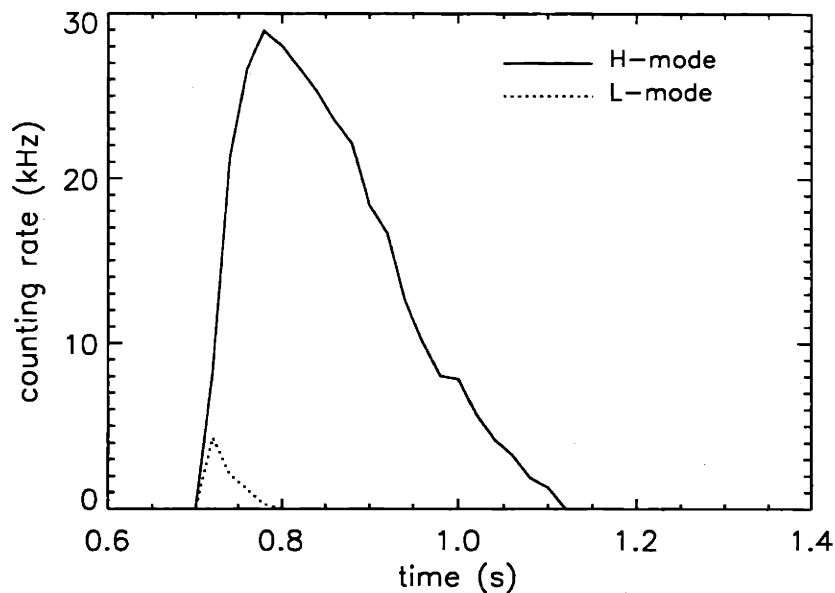
Figure 4-25: Comparison of helium-like scandium X-ray signals between a H-mode shot and a L-mode shot. The solid line is the H-mode time history. The dotted line is the L-mode one.

The H-mode studies show that the impurity content in the core plasma increases substantially during the H-mode. In the case of argon, the increase reached a factor of 5. Two factors might contribute to this increase, the increase of the impurity confinement time and the change of the ability of the SOL to screen the impurities. For a fixed impurity influx at the LCFS, the impurity density is proportional to the

impurity confinement time. So an order of magnitude increase in particle confinement time could contribute to all the increase in impurity density and suggested that there was no significant change in the screening ability of the SOL.

4.9 Uncertainties in the Argon Density Measurements

The high resolution x-ray spectrometers haven't been absolutely calibrated. But for the problems in this thesis, it is more important to measure the argon density of one discharge relative to another in order to compare the influence of various plasma parameters on the impurity screening than to measure the absolute level of argon density. To achieve maximum consistency, the data used in the thesis for argon impurity screening studies were taken with the same spectrometer at the same wavelength setting and viewing approximately the same location in the plasma. During the time the data were taken, this spectrometer had no change in configuration. So the uncertainty in the relative argon density measurement mainly comes from the uncertainty of the electron temperature and density measurements, especially the electron temperature measurements because the emissivities of the helium-like argon lines are strong functions of the electron temperature. This fact is also advantageous in terms of reducing the uncertainty of the argon density measurements because the line-integrated brightness of the helium-like argon lines have little contribution from the outer cooler region of the plasma where the electron density and temperature measurements have larger uncertainties.

Since it's more important to know the relative trend of the impurity penetration variation as a function of various plasma conditions for the purpose of this thesis, the systematic errors of the electron temperature and density measurements are of little concern. Instead, the random errors, or dispersion, of these measurements contribute most to the uncertainties of the analysis used here. For a standard magnetic geometry plasma discharge, as all the discharges discussed in this chapter, the electron density measurement has a error range of less than 10% for the core plasma. (Ref. [36])

The situation for the electron temperature measurement is, however, more complex. Electron temperature (ECE) measurement has gone through many re-calibrations during the course of the Alcator C-Mod operations. This inevitably increase the uncertainty of the temperature data if data from runs between different calibration period are used. The uncertainty is about 15%. When data from the same calibration period, especially the same run day, are used, the random errors are reduced to within 5%. (Ref. [37]) So in the analysis in this chapter, T_e's error range for discharges from the same run day is taken as 5%, while it is taken as 15% for discharges taken from different run days.

Error bars for the analysis in this chapter are obtained by varying the electron density and temperature to their maximum error range and calculating the argon density using the varied electron density and temperature profiles.

4.10   Conclusion

Comparisons of the impurity screening characteristics between the diverted plasmas and the limited plasmas showed that argon penetration in the diverted plasmas was significantly lower than that in the limited plasmas. The reason for divertor's superior performance was that in the scrape-off region the diverted plasmas have higher electron density and temperature than the limited plasmas. This confirmed the advantage of the divertor over the limiter in impurity screening. A penetration model was developed to relate impurity penetration to edge plasma parameters. The results calculated using this model were consistent with the experimental observations. For diverted plasmas, the argon penetration shows no dependence on divertor target plate strike point locations, outer gaps, or heating modes (ICRF versus ohmic). An argon penetration scaling was found to be in the form of $p \propto \frac{1}{\bar{n}_e}$ for ohmic and L-mode plasmas. For the Alcator C-Mod run period from November 1994 to June 1995, $p(\%) \approx \frac{2.1}{\bar{n}_e/10^{20}}$. This inverse dependency of p on $\bar{n}_e$ was consistent with the penetration model's prediction. Impurity content in the H-mode plasmas was about a factor of 5 higher than that in the L-mode plasmas. However, the longer H-mode

particle confinement time also suggests that the screening efficiency of the SOL may not change significantly during the H-mode.

Chapter 5

Impurity Transport Studies

5.1 Introduction

5.1.1 The MIST Code

The analysis in Chapter 4 relies on the correct prediction of argon density profiles by the MIST (Multiple Ionization State Transport) code. MIST is a one-dimensional time dependent impurity transport code developed to predict the impurity behaviour in an evolving plasma ([28]). Its use in diagnosing the plasma has been extensively described in Ref. [38]. The equation governing the impurity transport is:

$$\frac{dn_i(\mathbf{r})}{dt} = n_{i+1}(\mathbf{r})n_e(\mathbf{r})\alpha_{i+1}(T_e) - n_i(\mathbf{r})n_e(\mathbf{r})S_i(T_e) - \nabla \cdot \mathbf{\Gamma}(\mathbf{r}) , \qquad (5.1)$$

where $n_i(\mathbf{r})$ is the density of the i times ionized ions at the location $\mathbf{r}$; $n_e(\mathbf{r})$ is the electron density; $\alpha_{i+1}(T_e)$ is the total recombination coefficient for the recombination from the $i + 1$ times ionized to the i times ionized ions; $S_i(T_e)$ is the ionization coefficient of the i times ionized ions; $\mathbf{\Gamma}(\mathbf{r})$ is the flux of the i times ionized ions, described as the sum of a diffusive and a convective term:

$$\mathbf{\Gamma}(\mathbf{r}) = -D_i \nabla n_i(\mathbf{r}) + n_i(\mathbf{r})\mathbf{V_i} , \qquad (5.2)$$

where D_i is the impurity diffusion coefficient of the ith charge state; $\mathbf{V_i}$ is the convection velocity of the ith charge state. Both D_i and $\mathbf{V_i}$ are taken to be functions of

the radial coordinates.

Equation 5.1 can be written for each of the charge states and the resulting set of equations is coupled. The MIST code solves this coupled set of equations and gives the relative abundance of different charge states as a result. In the calculation, D_i and V_i are taken as the same for all charge states.

5.1.2 Topics in this Chapter

Of all the factors that can affect the impurity density profile, two important ones are the diffusion coefficient (D) and convection velocity (V) because they determine the impurity flux, as indicated by Equation 5.2. Studies were done on Alcator C-Mod using the laser ablation technique to measure the impurity transport coefficients $(D$ and $V)$. Another way to infer these coefficients is to model the brightness profiles of argon x-ray signals and studies were done this way as well. The results of the studies will be presented in the following sections. In Section 5.2, evidence that an edge concentration of impurity existed in some cases will be given. Analysis in this section also suggests that possible cause of this phenomenon was a reduced D and an outward convection at the outer region of the plasma. In Section 5.3, analysis of a pellet injection plasma in Alcator C-Mod will be presented. The results of the analysis suggest that a large inward convection followed the pellet injection and caused the impurity density profile to peak strongly. In Section 5.4, Results from two H-mode transport studies will be presented, showing that H-mode impurity particle transport characteristics differed with L-mode mainly at the edge. The impurity particle transport itself also changed within the duration of H-mode. Evidence of this will also be discussed in this section.

5.2 Analysis of the Brightness Profiles for Alcator C-Mod Shot 931014005

5.2.1 Data Analysis
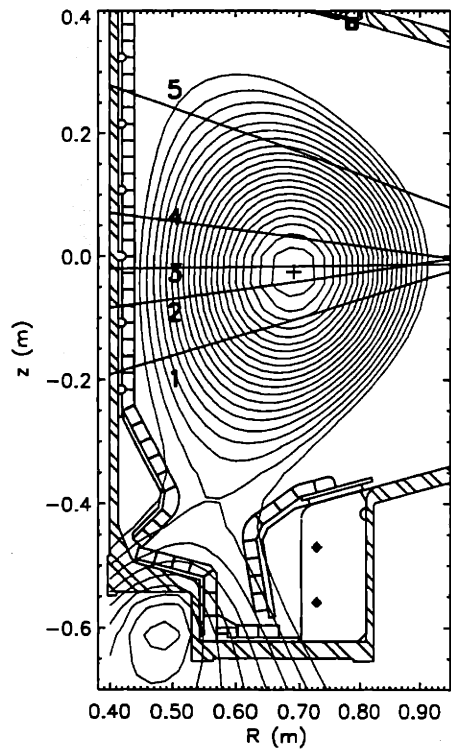
Figure 5-1: Hirex viewing chords locations in Alcator C-Mod discharge 931014005.

Figure 5-2: Brightness profile for the w line calculated with no D or V modification. Shot 931014005. Total counts were integrated over 0.55 sec — 0.65 sec. Solid line represents the modeled brightness profile. Black dots are the observed brightnesses.

Figure 5-3: Observed and synthetic spectra for shot 931014005, spectrometer # 5. The spectrum was integrated from 0.55 second to 0.65 second. The solid line is the observed spectrum. The dashed line is the synthetic spectrum.

Figure 5-4: Observed spectrum and synthetic spectrum multiplied by 5 for shot 931014005 spectrometer # 5. The solid line is the observed spectrum. The dashed line is the synthetic spectrum.

For Alcator C-Mod discharge 931014005, (see Figure 5-1 for the flux contour and the hirex viewing chord locations), the modeling of the spectra whose lines of sight were near the plasma center were successful within a reasonable range of error. But for spectrum #5, which looked near the edge ($r/a = 0.8$) of the plasma, the synthetic line strength was 1/5 of that of the observed one. See the calculated brightness profile for the w line and the actual brightness obtained by the spectrometers in Figure 5-2. Also see Figure 5-3 and Figure 5-4. One possible reason for this was that the contribution from charge exchange recombination was not accounted for in the calculation. Charge exchange between the hydrogen-like argon ions and the neutral hydrogen atoms produces excited state helium-like argon ions with n around 9, which subsequently cascades to $n = 2$ levels. However, when trying to fit the difference between the experimental and synthetic data using the three distribution models discussed in Section 3.1.2, it was found that none of these models yielded a satisfactory result. Figure 5-5 shows the discrepancy between the observed spectrum and a synthetic spectrum with no charge exchange contribution. This discrepancy was obtained by subtracting the synthetic spectrum in Figure 5-3 from the observed spectrum. Figures 5-6 to 5-8 show the charge exchange recombination contribution calculated from each of the three models. Comparisons between Figure 5-6 to Figure 5-8 and Figure 5-5 show that even though all three charge exchange models produced results agreeing well with the observed spectrum for w and z lines, none of the models produced the correct line ratio between the intercombination lines x and y. All three models reversed the line ratio between the x line and the y line. The ratio between the intercombination lines and the forbidden lines was also wrong. To make matters worse, charge exchange recombination made no contribution to the satellite line brightnesses. So the satellite lines would remained too low if charge exchange recombination indeed made a significant contribution to the line strength at the outer regions of the plasma. It was very difficult to include charge exchange recombination as a significant population mechanism.

A re-examination of Figure 5-4 showed reasonable agreement between the observed spectrum and the synthetic spectrum multiplied by a factor of 5. Both the line
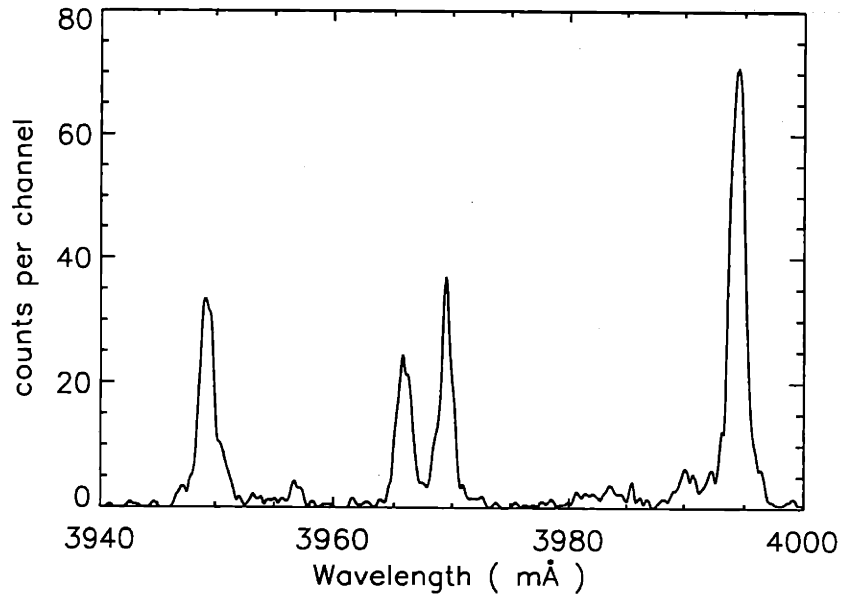
Figure 5-5: Discrepancy between the observed and synthetic spectrum for spectrometer # 5 in shot 931014005. From 0.55 sec to 0.65 sec
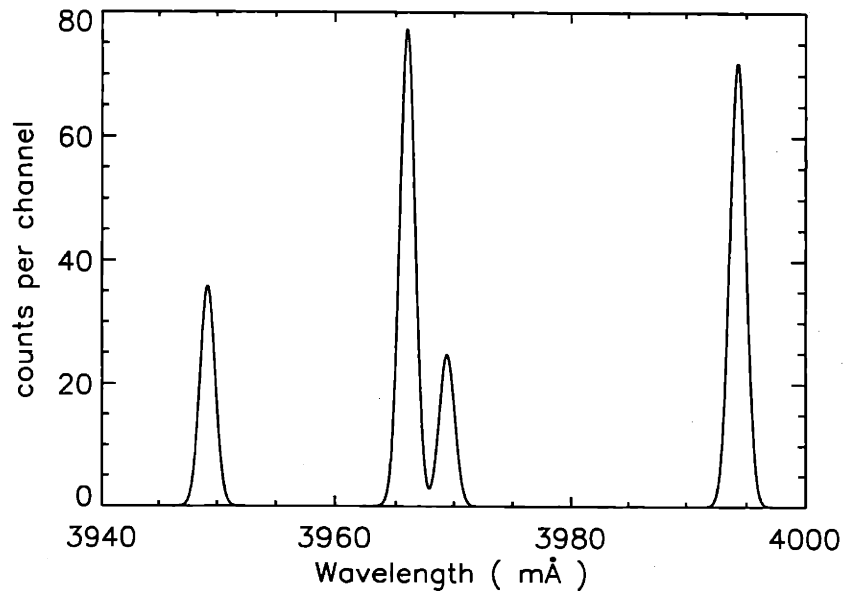
Figure 5-6: Charge exchange recombination contribution calculated from Model 1 of Section 3.1.2 for spectrometer # 5
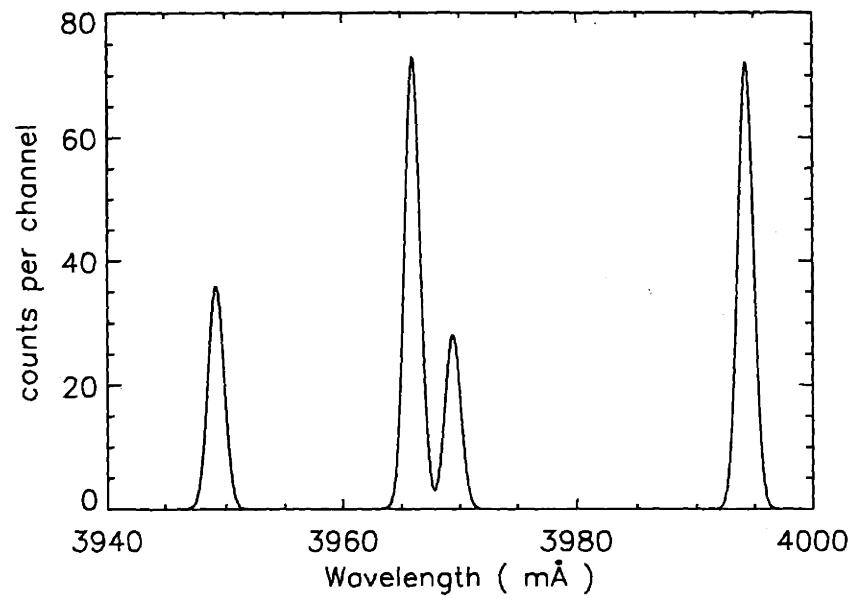
Figure 5-7:   Charge exchange recombination contribution calculated from Model 2 of Section 3.1.2 for spectrometer # 5
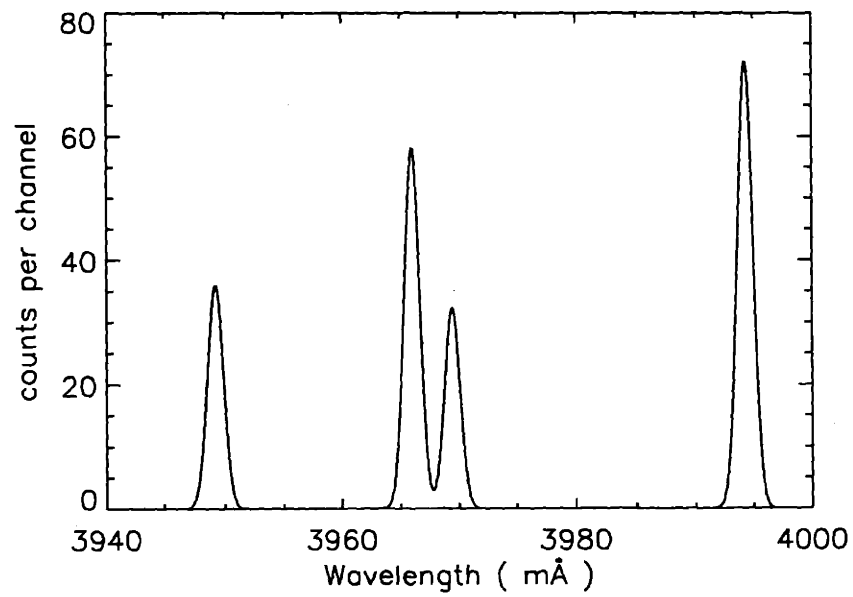
Figure 5-8:   Charge exchange recombination contribution calculated from Model 3 of Section 3.1.2 for spectrometer # 5

ratios and the satellite line strengths agreed well. This suggested that the model was systematically underestimating the intensities which in turn might be explained by a local concentration of argon in the edge of the plasma.

A possible cause for the edge concentration of the impurities was that an edge transport barrier existed. To produce a suitable argon ion density profile in which there is an edge concentration of argon, the diffusion coefficient profile and convective velocity profile used in the MIST code were varied. With the highly simplified profiles shown in Figures 5-9 and 5-10, the synthetic spectrum was more than doubled in intensity. See Figure 5-11 for the brightness profile of the w line. Also see Figure 5-12 and Figure 5-13. The satellite line ratios also agreed better with the observed spectrum. This supported the assumption of a local concentration of argon.
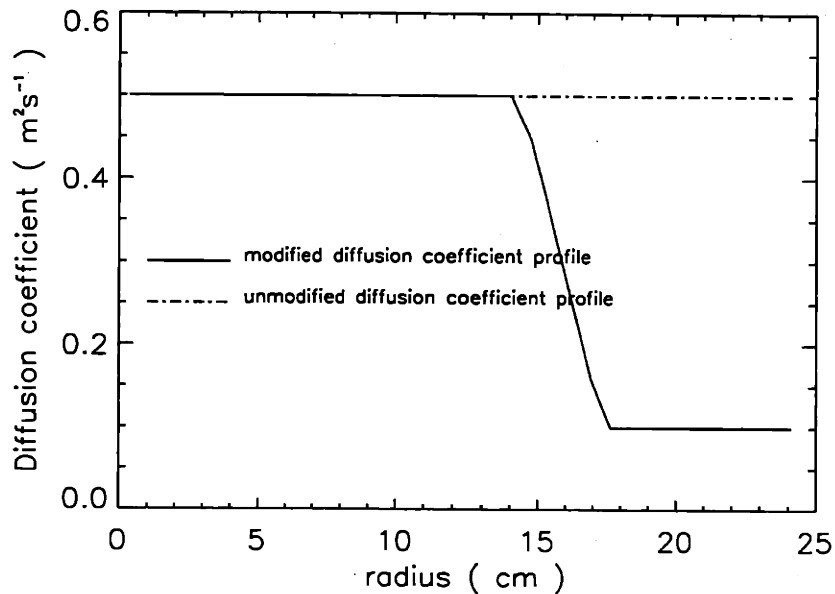
Figure 5-9: Diffusion coefficient profile modified to produce higher argon density at outer region. Also shown in the dashed line is the unmodified diffusion coefficient profile.

The new argon ion density profiles produced by the MIST code with modified diffusion coefficient and convective velocity profiles are shown in Figure 5-14, along with the argon ion densities produced by unmodified diffusion coefficient and convective velocity profiles. Comparison of those two sets of profiles shows that the new Li-like Ar density was over 10 times higher than the unmodified Li-like Ar density beyond
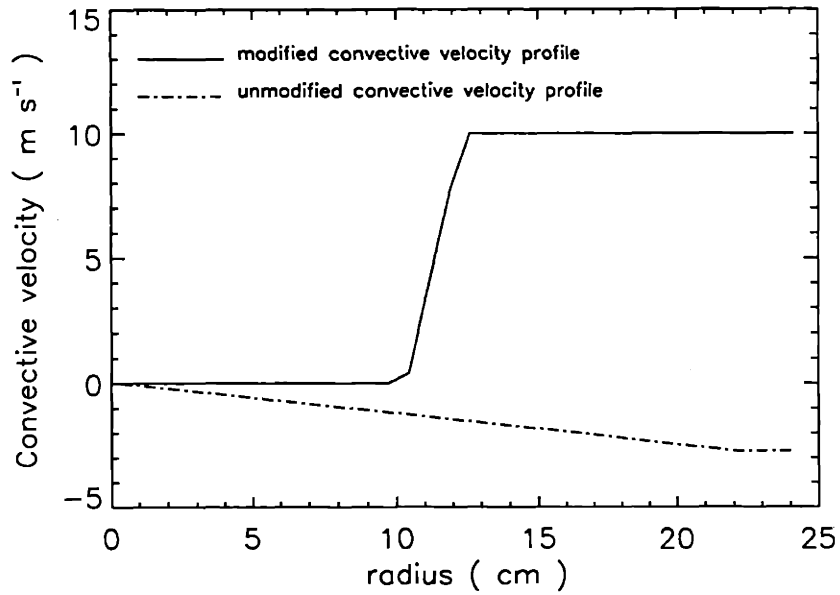
Figure 5-10: Convective velocity profile modified to produce higher argon density at outer region.Also shown in the dashed line is the unmodified convective velocity profile.
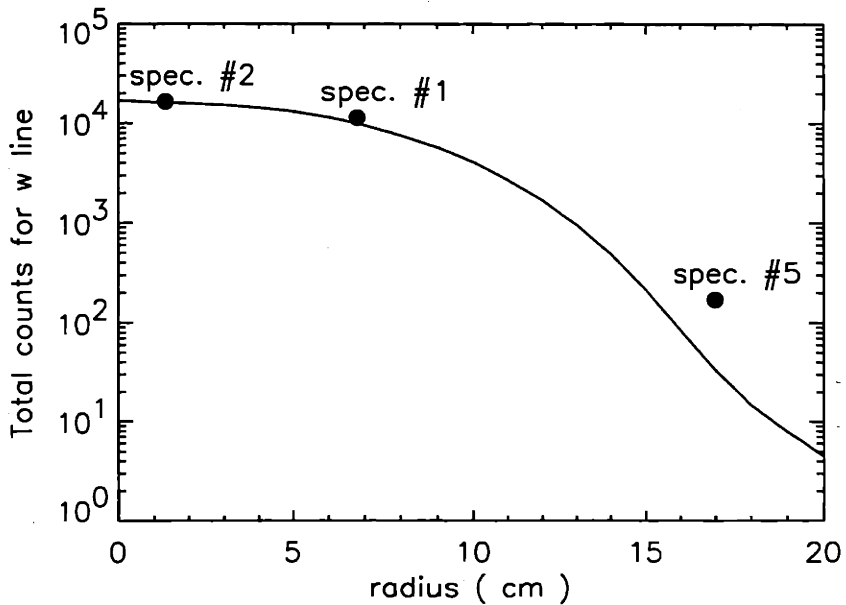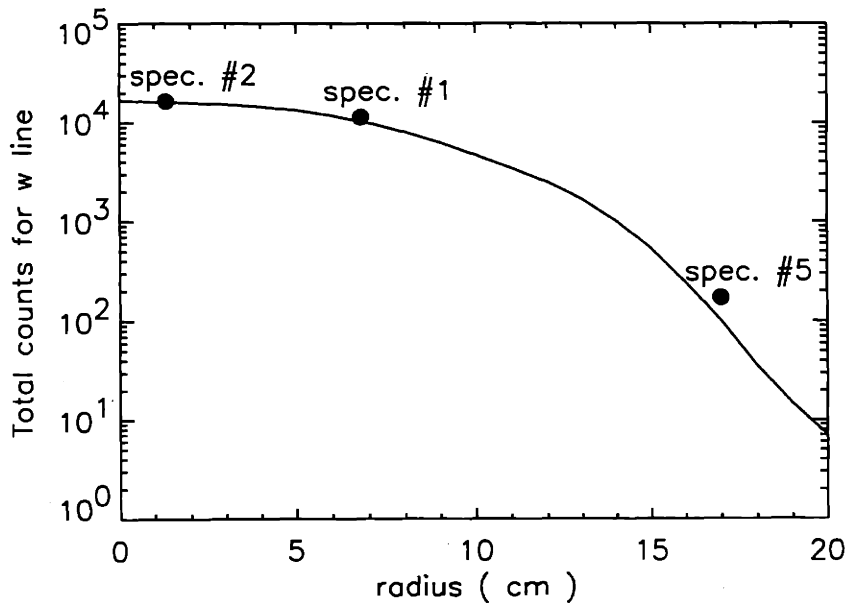

Figure 5-11: Brightness profile for the w line calculated with D and V modification. Shot 931014005. Total counts were integrated for 0.55 sec — 0.65 sec. Solid line represent the modeled brightness profile. Black dots are the observed brightness.
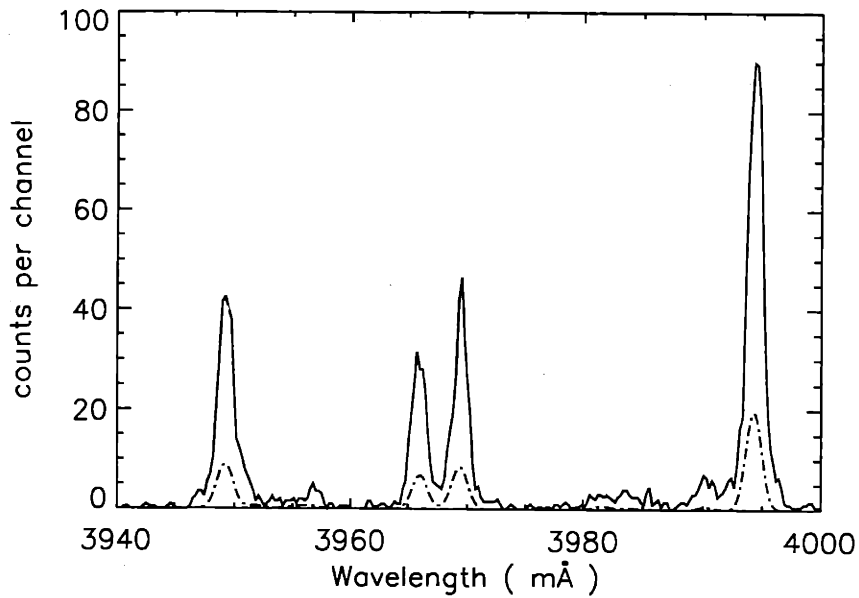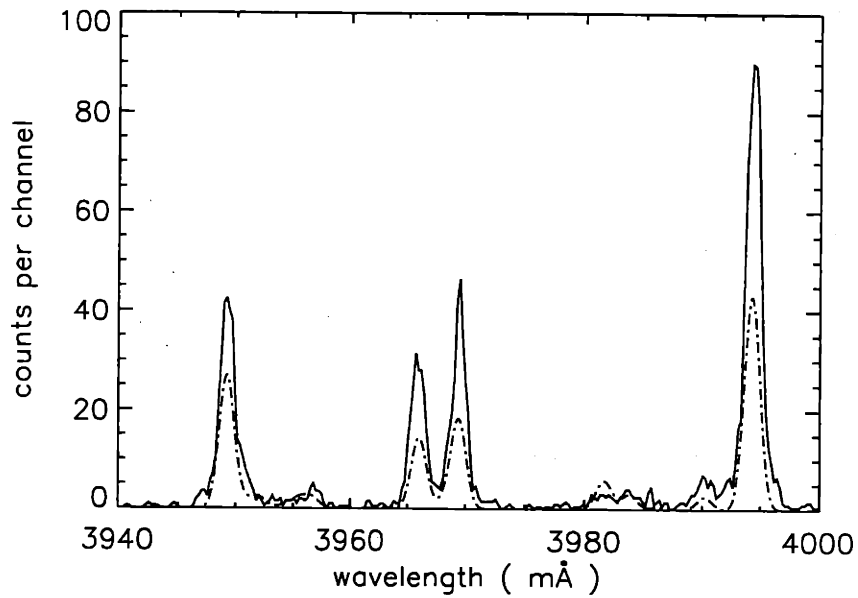
Figure 5-12: Overplot of observed spectrum and synthetic spectrum obtained with modified D and V profiles for shot 931014005 spectrometer # 5. Spectrum taken from 0.55 second to 0.65 second. The solid line is the observed spectrum. The dashed line is the synthetic spectrum.

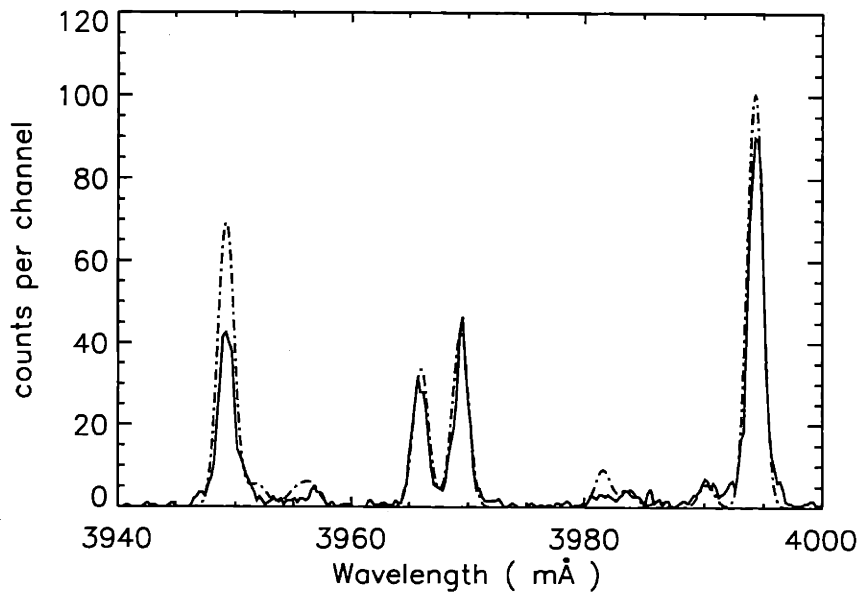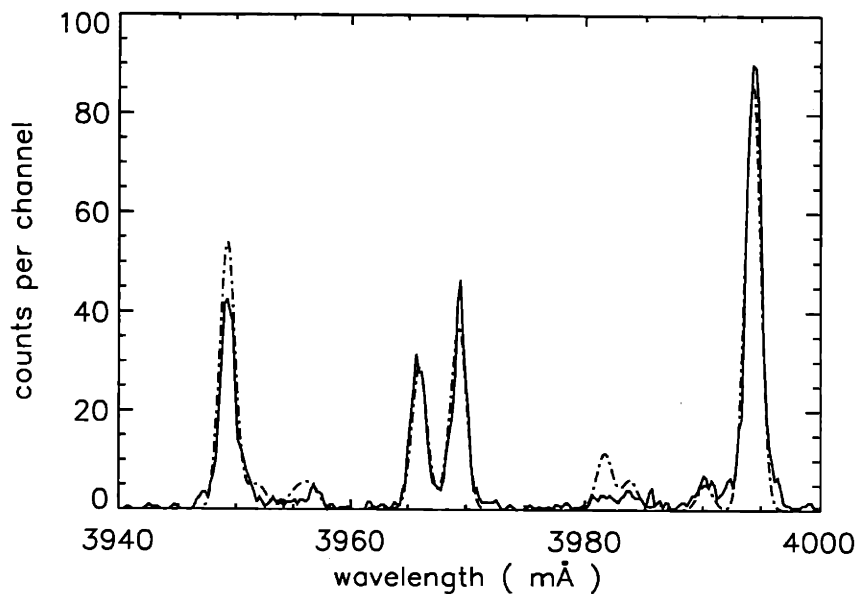Figure 5-13: Observed spectrum and synthetic spectrum obtained with modified D and V profiles and multiplied by 2 for spectrometer # 5. The solid line is the observed spectrum. The dashed line is the synthetic spectrum.

17 cm. This will be discussed further in Section 5.6.
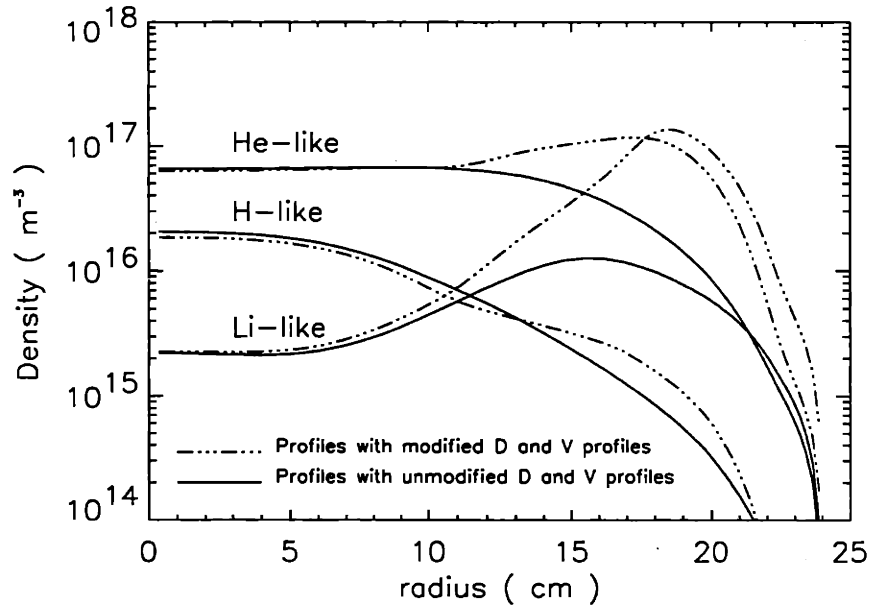
Figure 5-14:   Density profiles for H-like, He-like and Li-like argon using unmodified and modified D and V profiles.

5.2.2   Uncertainty Analysis

As in any other analysis using the argon density obtained by fitting the absolute intensity of the helium-like argon spectrum, the uncertainties in the T_e and n_e measurement contribute to the uncertainties in the analysis in this chapter. But unlike in Chapter 4, in which only the central chord x-ray data are used, data from two or more spectrometers viewing at different locations are used in this chapter. Therefore the difference in the sensitivities of the spectrometers has to be taken into account. The relative sensitivities of the five spectrometers have been calibrated by having two spectrometers with overlapping ranges looking at the same magnetic flux surface and comparing the signal intensity. Adjustments were made to the raw spectra to compensate for the difference in sensitivities. So the uncertainties in the adjustment coefficients determine the uncertainty this contributes to the total error bar. The spatial resolution of the spectrometer is around 1cm. This brings $\sim$ 10% error in

111

relative sensitivity calibration. For many cases where a spectrum is taken along a line of sight distant from the plasma center, a slight error in electron temperature measurement would cause more than twice as much error in the argon density measurement due to the strong dependance of helium-like argon emissivity on the electron temperature, especially in the low temperature region. Since the T_e measurement has error bars of $\sim 15\%$ at the outer region of the plasma, ([39]), in many cases by varying the T_e within its error range, the calculated brightness can be varied greatly to fit the observed brightness. But this cannot be the case for shot 931014005. The line ratios between the helium-like argon principal lines are also strongly dependant on the electron temperature. Figure 5-4 shows that the observed line ratio between the z and w line was higher than the calculated one. This indicates that the actual electron temperature was lower than the one used in the intensity calculation, and a lower electron temperature would only result in a even lower x-ray intensity. So the uncertainty in the electron temperature measurement cannot explain the fact that the observed line intensity was five times as large as the theoretically predicted one.

In shot 931014005, the line of sight of the spectrometer #5 is 17 cm away from the center of the plasma. It was within the range of the last chord of TCI. This means the uncertainty of density measurement should be within 10% ([36]). So the total uncertainty of electron density and temperature measurement and spectrometer sensitivity differences could increase the calculated intensity by no more than 20%. The only logical means to explain the large discrepancy between observed and calculated line intensity was to suggest that a local concentration of argon in the edge existed, as the previous discussions have done.

5.3 Effect of the Pellet Injection on the Diffusion Coefficient and Impurity Penetration

The pellet injection technique has become the leading technology of refueling the magnetically confined plasma, enabling central fueling. One of the added benefits of this technique is the improvement in particle and energy confinement. An extensive

review of this technique can be found in Ref. [40]. The injection of a pellet causes a peaked density profile. This peaked profile, however, is not simply due to the central fueling. The peaking persists, demonstrating that pellet injection changes the particle transport. Of interest is whether the impurity transport also undergoes similar changes, because accumulation of impurities in the central region caused by peaked impurity density profile would result in a significant dilution of the fuel ([41]—[42]). Studies of impurity transport in several tokamaks observed the accumulation of impurities indeed ([43]—[49], [41]). In this section, analysis of pellet fueled plasmas in Alcator C-Mod will be presented.

5.3.1 Data Analysis
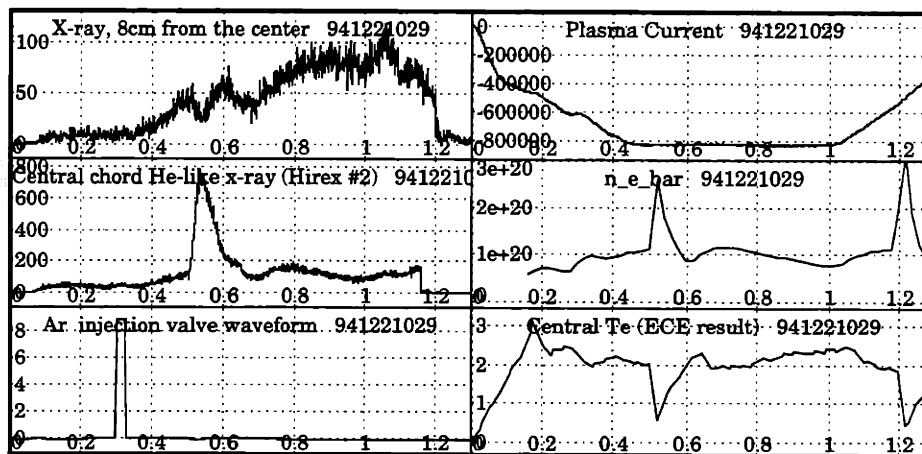
Figure 5-15: Time histories of x-ray signals and other important plasma parameters for Alcator C-Mod shot 941221029, during which lithium pellets were injected at 0.505 second and 1.2 second. For the plasma current, the y axis is in Amp. For the $\bar{n}_e$, the y axis is in m^{-3}. for the central T_e, the y axis is in keV. For the x-ray signals, the y axis is the counting rate in kHz. For the argon inject pulse, the y axis is the voltage applied to the pulsed valve in 10 volts.

During Alcator C-Mod shot 941221029, lithium pellets of macroscopic size were injected at 0.505 sec and 1.2 second. The one injected at 0.505 seconds was of interest. Figure 5-15 plots the time histories for important plasma parameters and the scaler signals from spectrometer # 2 looking at the center of the plasma and spectrometer #1 looking at about 8 cm away from the center. See Figure 5-16 for the magnetic
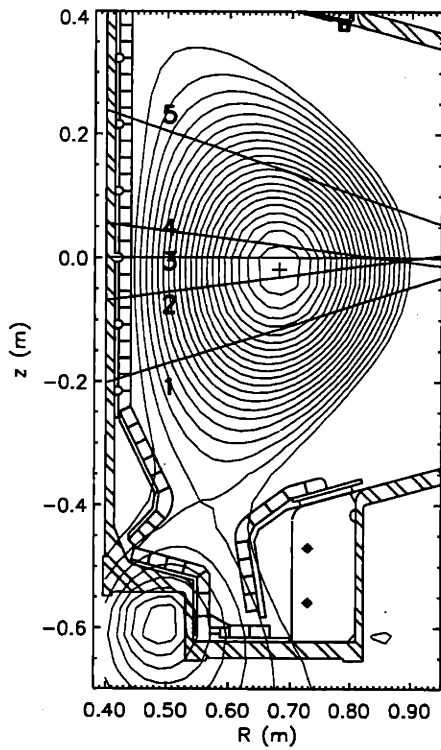
Figure 5-16: HIREX viewing chord locations during Alcator C-Mod discharge 941221029 from 0.4 s to 0.6 s.

geometry of this discharge and the Hirex viewing chord locations. After the pellet went in, the x-ray signal of the center chord (spectrometer # 2) increased by a factor of 7. The electron temperature, however, decreased dramatically. Given the fact that the x-ray emissivity of helium-like argon was very sensitive to the electron temperature, it would take a lot more argon in the plasma to produce an increased signal level. In fact, the total argon amount in the plasma reached a maximum of 11 times that of the amount before the pellet injection. Exactly why this was so is unclear. Another interesting observation was that while the signal from spectrometer #2 had a large increase after the pellet injection, the increase in signal from spectrometer #1 was much smaller. This suggests that the actual brightness profile fell off quicker at a larger radius following the pellet injection than before the pellet injection. If a spatially constant diffusion coefficient profile was assumed, then the counting rate of the spectrometer # 1 could be predicted by using the argon ion density profiles produced by the MIST code along with the observed counting rate of spectrometer # 2. Figure 5-17 plots the ratio of the predicted counting rate for spectrometer # 1 and the observed counting rate versus time. Before the pellet injection, the ratio was around 2. But during the injection period, the ratio went up to 10. This suggests that the actual density at the outer region of the plasma ($> 8cm$ in this case) was much lower than what was predicted by MIST using a convection velocity profile used for non-pellet shots. (This profile described an inward convection velocity increases linearly with minor radius and is about 3 m/sec at the plasma edge. See Figure 5-20.) To elucidate this further, two more figures are included here. Figure 5-18 shows the brightness profile calculated using V profiles for normal shots before the lithium pellet injection at 0.45 second with observed brightness overplotted on it. Figure 5-19 shows the brightness profile calculated using the same constant V profile at .55 second shortly after the lithium pellet injection at 0.505 second. In this case the observed brightness was much lower than the calculated value at 8 cm.

To address this problem, the the convective velocity (V) profile is altered along with diffusion coefficient (D) profile in an effort to produce an argon density profile which fell off quickly as the radius increases. It is found that the same argon density

115
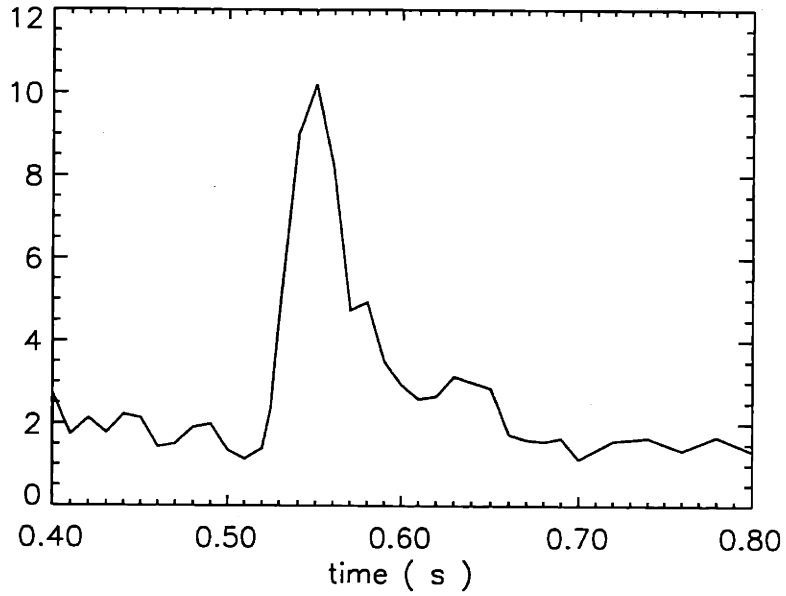
Figure 5-17:   Ratio between predicted counting rate for spectrometer # 1 and the observed counting rate for a Alcator C-Mod lithium pellet shot.
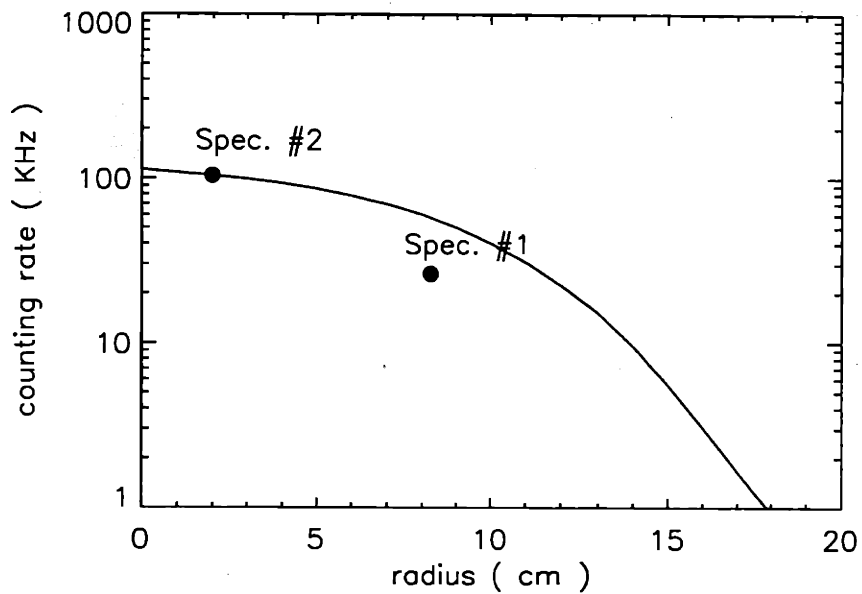
Figure 5-18:   Brightness profile calculated with V modification for the Alcator C-Mod lithium pellet shot before the pellet injection at 0.45 second. The solid line is the brightness profile. Solid dots are the observed brightness.
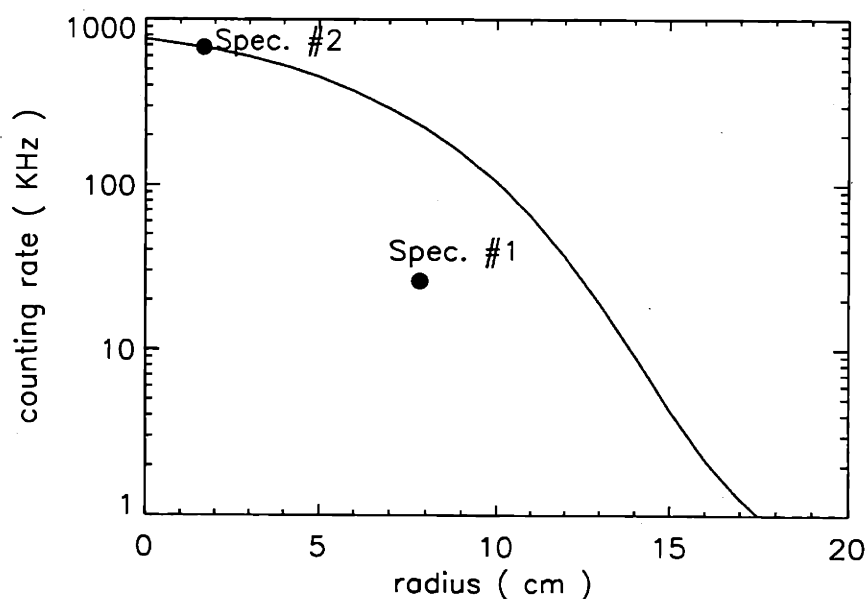
Figure 5-19:   Brightness profile calculated with no V modification for the Alcator C-Mod lithium pellet shot at 0.55 second, 45 ms after the lithium pellet injection. Solid line is the brightness profile. Solid dots are the observed brightness.

profile could be produced by varying either V or D alone, or by varying both at the same time. To isolate the real cause of the argon density peaking, time histories of imaginary scandium injections were produced with MIST code in a time dependant mode. It was found that variation of the D profile would lead to long impurity rise time ($\sim 50ms$), which was much longer than what is observed ($\sim 10ms$) in the experiments. This suggests that varying the V alone should explain the peaking of argon density. Figure 5-20 plots the V profiles needed to produce a brightness profile consistent with the measurements. Figure 5-21 shows the argon density profiles resulted from such D and V profiles. Figure 5-22 shows the brightness profile calculated using this V profile at 0.55 second shortly after the pellet injection. The difference between the observed brightness for spectrometer # 1 and the calculated brightness was the same as that before the pellet injection. See Figure 5-18 for comparison. Though the V profile used in obtaining this result was highly simplified, it offered strong evidence of the existence of a very large convection velocity during the pellet injection.
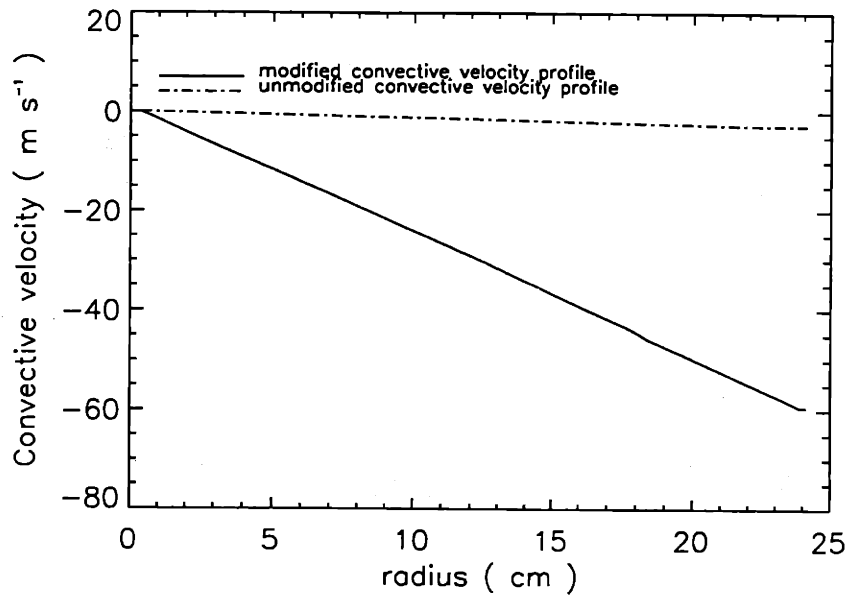
Figure 5-20: Convective velocity profile modified to produce lower argon density at the outer region. Also shown in the dashed line is the unmodified convective velocity profile.
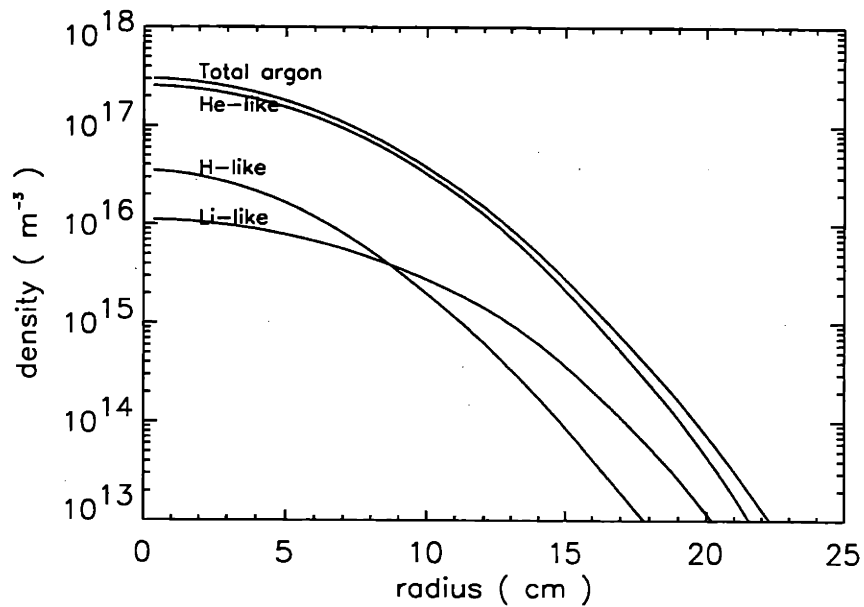
Figure 5-21: Density profiles for H-like, He-like and Li-like argon ions calculated using modified D and V profiles for the Alcator C-Mod lithium pellet shot.
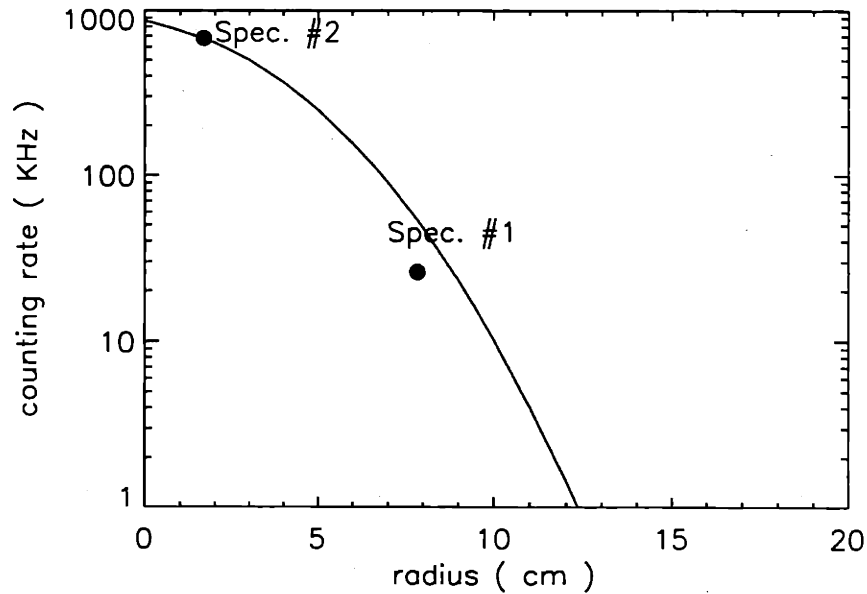
Figure 5-22: Brightness profile calculated with no D or V modification for the Alcator C-Mod lithium pellet shot at 0.55 second. Solid line is the brightness profile. Solid dots are the observed brightness.

5.3.2 Uncertainty Analysis

Much of the error analysis in Section 5.2.2 can also be applied here. However, the TCI measurement of the electron density is known to be wrong during the pellet injection period. The actual electron density profile is much more peaked in the center than that is indicated by the TCI measurement. (Ref. [50]) The actual peaked electron density can be as much as twice the TCI value. (Ref. [36]). This would reduce the discrepancy between the observed brightness taken by spectrometer #1 and the theoretically predicted brightness by a factor of 2. Electron temperature and spectrometer sensitivity contribute another 20% in uncertainties. However, the combined effect of the uncertainties can not fully explain the large discrepancy between the observed brightness taken by spectrometer #1 and the theoretically predicted brightness. A strongly peaked argon density profile must be at least part of the explanation.

5.4 Impurity Transport During H-mode

During H-mode, the transport coefficients can change quite substantially compared to L-mode conditions. (Ref. [51] and [52]) A few experiments to study the impurity particle transport characteristics of H-mode were carried out in the past on various machines. On JET (Ref. [53]), nickel was injected using the laser blow-off technique. Transport simulations were run to find the best fit for the observed data. It was found that the radial profile of the diffusion coefficient, D, increases in the outer part of the plasma. During H-modes, D decreased to about 1/8 of L-mode value in the outer part of the plasma and only a slight decrease was found in the plasma center. The increase of D in the outer plasma was needed to explain the observed hollowness of the emissivity profile of the central species. A large inward convection velocity ($V = 50$ m/s compared to 6 m/s for L-mode) was also needed to explain the behavior of the edge species during H-mode. On DIII-D (Ref. [54]), the MIST code was used with constant transport parameters and an evolving density profile to simulate the evolution of intrinsic nickel impurity signals during giant ELMs. It was found that a large spatially invariant $D = 1$ m^2/s and a convection velocity profile of the form $V = 3D\frac{\partial \ln n_e(r)}{\partial r}$ could produce satisfactory simulation results. Since the electron density profile was found to remain flat during H-mode with large gradients in the edge on DIII-D, this V formula implied that the convection was only significant at the edge. Laser blow-off injection of cobalt was also studied and the results were consistent with that of the intrinsic impurity transport study. On ASDEX (Ref. [55]), an edge transport barrier existed inside the separatrix with a width of ≤ 3 cm. The electron diffusivity was found to be 1/6 of L-mode value within a radial zone of $\simeq 3$ cm inside the LCFS. An earlier study (Ref. [56]) presented a transport scaling:

$$D(r) = 0.4\chi_e(r) = 0.4C_0 q(r)B_T(R)^{-1} \quad cm^2/s \ ,$$
$$V(r) = -0.5D(r)\frac{\partial \ln T_e}{\partial r} \quad cm/s \ , \tag{5.3}$$

where $C_0 = 2.5 \times 10^5$ for H-mode and $C_0 = 6.2 \times 10^5$ for L-mode; R is the major radius.

On JT-60U (Ref. [57]), evidence suggested that an internal transport barrier exists during its "High-β_p H-mode". However, the cause of the barrier was not found.

In general, H-mode results in enhanced particle confinement. However, the actual behavior of the transport parameters varies from tokamak to tokamak. Therefore it is of interest to study the transport characteristics of H-mode in Alcator C-Mod. In this section, results from H-mode transport studies on Alcator C-Mod are presented.
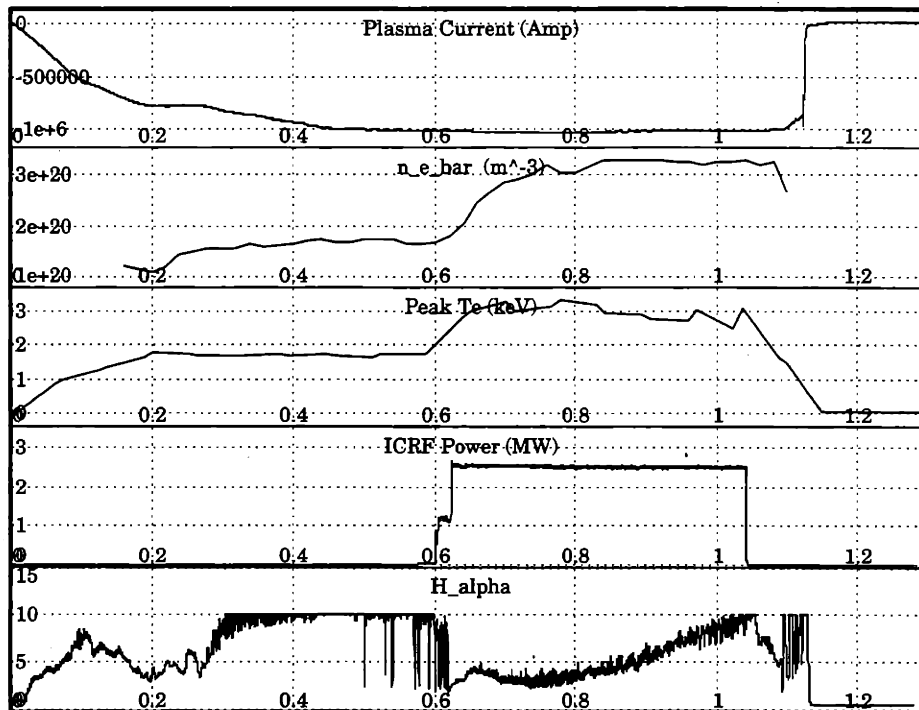
Figure 5-23: Plasma parameters for H-mode scandium injection experiment.

Quasi-static, ELMy and ELM free H-mode plasmas have been achieved in Alcator C-Mod , (see Figure 5-23), enabling the transport study in the Alcator C-Mod tokamak. Scandium was injected during H-mode phase in one experiment. The time history studies on both helium-like scandium x-ray emission and lithium-like VUV emission enabled the determination of the transport coefficients. The HIREX x-ray spectrometers and the McPherson VUV spectrometer were scanned on a shot-to-shot basis for a series of almost identical shots to provide the brightness profile measurements. (Figure 5-24) The brightness profiles of helium-like scandium and lithium-like scandium emission offered further constraints on the transport coefficient profiles de-

121

rived. The plasma parameters were as follows: $I_p = 1.0MA$, $\bar{n}_e \simeq 1.7 \times 10^{20}$ m^{-3} (Ohmic) and $\bar{n}_e \simeq 3.5 \times 10^{20}$ m^{-3} (H-mode), ICRF power of 2.5 MW was applied in 0.45 second long pulses in addition to ~ 0.6 MW Ohmic power, $\kappa \simeq 1.6$. (Also see Figure 5-23.) ELMy H-modes were achieved during the ICRF heating phase, from 0.6 sec to 1.05 sec. Scandium was injected at 0.7 sec using the laser blow-off technique. The subsequent evolution of the helium-like scandium signals was shown in Figure 5-24. The evolution of the central chord helium-like scandium and lithium-like scandium signals are given in Figure 5-25 and 5-26, respectively. (Simulated fits and the typical L-mode time history of those signals are also plotted on the two figures.)
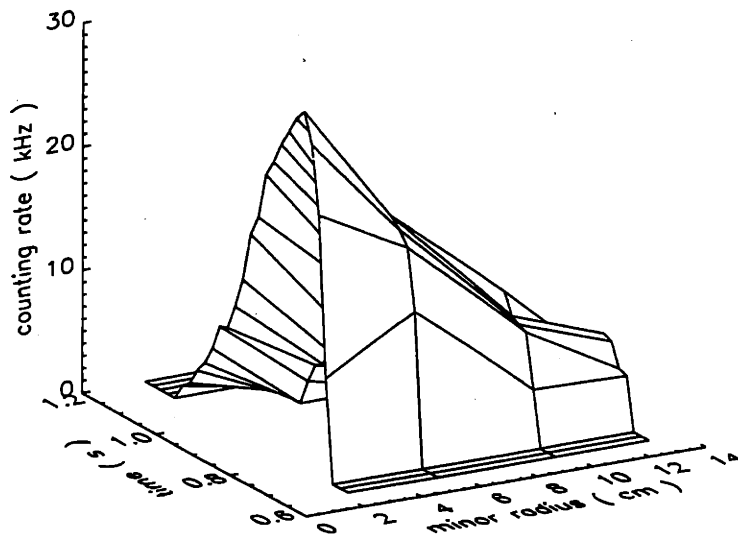
Figure 5-24:   X-ray Brightness profile of helium-like scandium. Spectrum of the resonance w line is used. Time resolution is 20 ms.

The time histories of x-ray and VUV emissions show that the impurity confinement time was an order of magnitude longer than that of L-mode phase, confirming the increased particle confinement characteristics of H-mode as observed on other machines. It was also shown clearly that a change in transport takes place between 0.85 second and 0.90 second. The impurity particle confinement became noticeably poorer after the transport change. (See Section 5.5 for more discussions.) However, the impurity confinement time after the transport change was still a factor of three
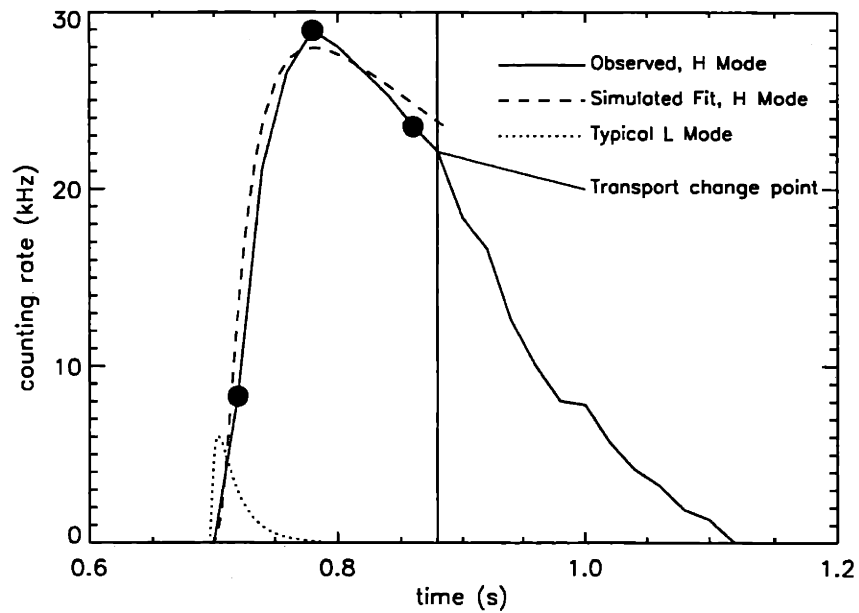
Figure 5-25: Central chord scandium x-ray time history during ELMy H-mode. The solid line is the time history observed by HIREX. Spectrum of the resonant w line is used. Signals are digitized every 20 ms. The dashed line is the simulated fit. Notice that the transport apparently changes to the right of the vertical line. Also plotted in a dotted line is the time history of a typical L-mode scandium injection. The solid dots represent the time for which the comparisons of the observed and simulated radial brightness profiles of helium-like scandium w line x-ray emission are made in Figure 5-32.

Figure 5-26: Center chord scandium VUV time history during ELMy H-mode. The solid line is the time history observed by the McPherson spectrograph. Spectrum of the $1s^2 2p_{j=3/2}$ − $1s^2 2s$ line at $281.8\mathring{A}$ was used. The dashed line is the simulated fit. Notice that the transport apparently changed to the right of the vertical line. Also plotted in a dotted line is the time history of a typical L-mode scandium injection. The solid dots represent the time for which the comparisons of the observed and simulated radial brightness profiles of lithium-like scandium VUV emission are made in Figure 5-33.

longer than L-mode impurity confinement time. Figure 5-24 shows that the helium-like radial brightness profile remained peaked throughout the the whole injection, even after the transport change point, in contrast with the hollow profile observed in JET.

Diffusion coefficient

Convection velocity
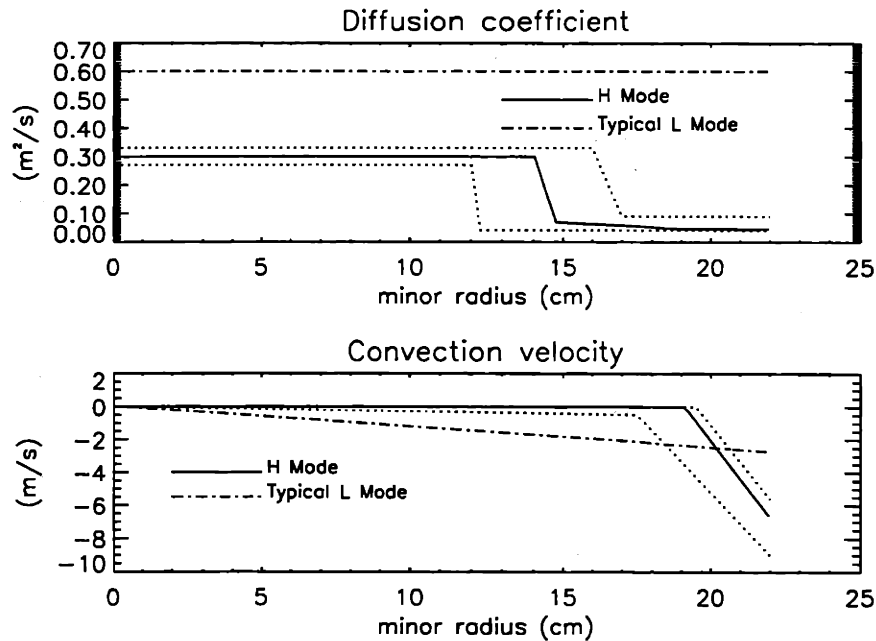
Figure 5-27: Radial transport coefficient profiles during H-mode. The two dashed lines on each figure shows the range of the transport profiles. Also plotted are the typical L-mode transport coefficient profiles.

The MIST code was used to simulate the time histories of the scandium x-ray and VUV signals before the transport change point. Four sets of observation data were available for the simulation: the radial profile and time history of the brightness of the central species — helium-like scandium; and the radial profile and time history of the brightness of the edge species — lithium-like scandium. Detailed study using a wide range of the transport coefficient profiles was done to find the best fit for these four sets of data. It was found only a D profile that decreases substantially at the edge and a large inward convection influx could fit all four sets of data simultaneously. Figures 5-28 to 5-31 show some of the other transport coefficient profiles that had been tested. The transport coefficients for the best fit are shown in Figure 5-27. In the center, the diffusion coefficient was lower than, but still comparable to, that

of L-mode plasma. However, D decreased substantially at the edge to an order of magnitude lower than L-mode value. A large inward convection velocity was found in the edge, within several centimeters of the separatrix.

It should be noted that the there is not one unique set of solutions for the transport coefficient profiles. Figure 5-27 uses two dashed lines to mark the range within which the transport coefficient profiles can be varied while they still produce good fits.
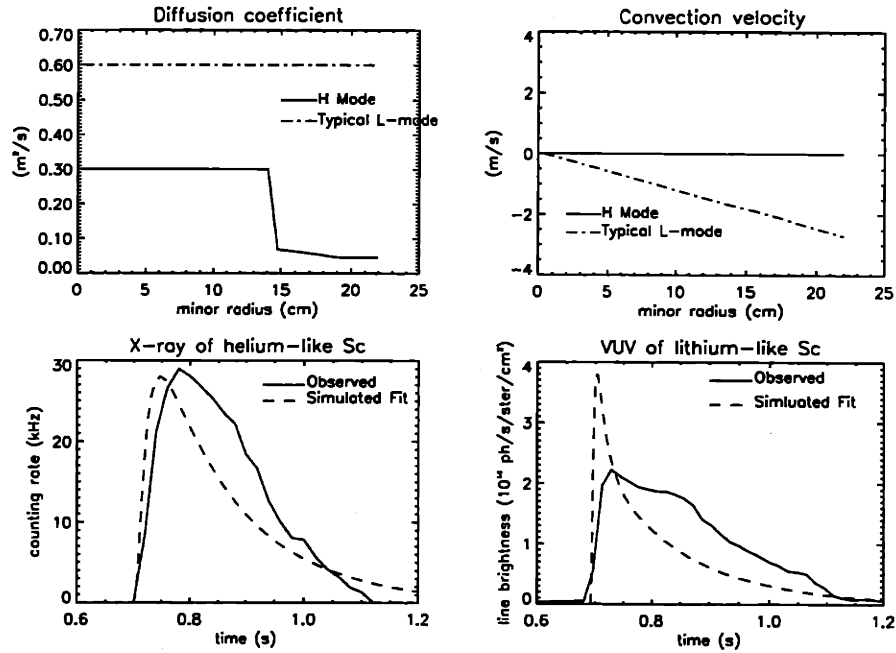
Figure 5-28: A set of transport efficient profiles tested for fitting H-mode x-ray and VUV signals. This set shows that the edge species' signal cannot be fitted correctly without inward convection at the edge.

Figures 5-25 and 5-26 show the simulated central chord time histories of helium-like and lithium-like scandium signals in comparison to the observed data. Figures 5-32 and 5-33 show the simulated radial profiles of helium-like scandium and lithium-like scandium brightness along with the observed profiles at three different time points. The simulations agree well with the observations.

In the toroidal devices as the tokamaks, some particles are trapped by the magnetic mirror effect between the high field regions of a helical field line. The guiding centers of these trapped particles trace out banana-shaped orbits. As a particle makes collisions, it becomes trapped and untrapped successively and moves from one banana
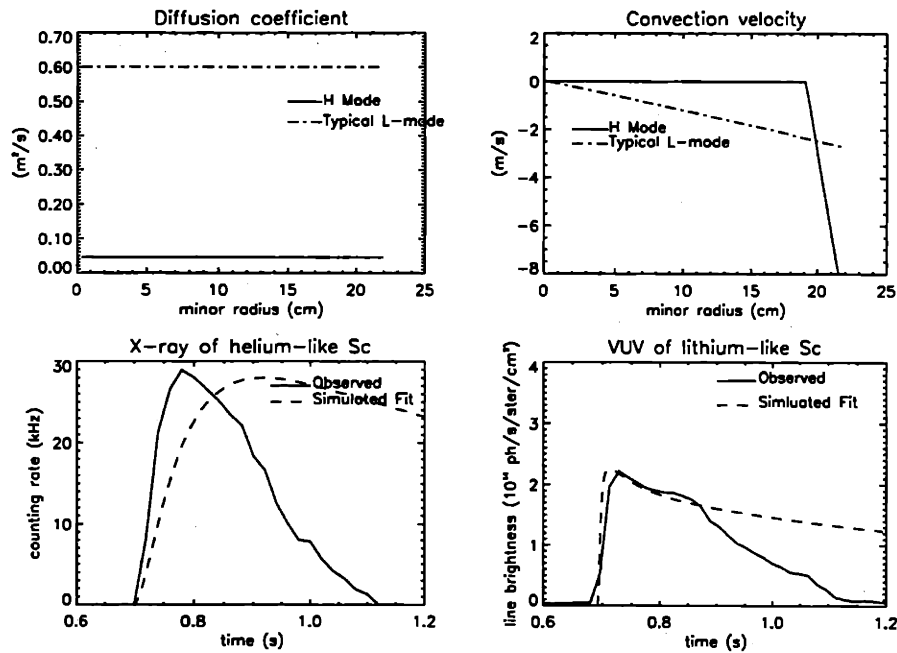
Figure 5-29:   A set of transport efficient profiles tested for fitting H-mode x-ray and VUV signals. This set shows that the central species' signal cannot be fitted correctly without higher diffusion coefficient in the center.
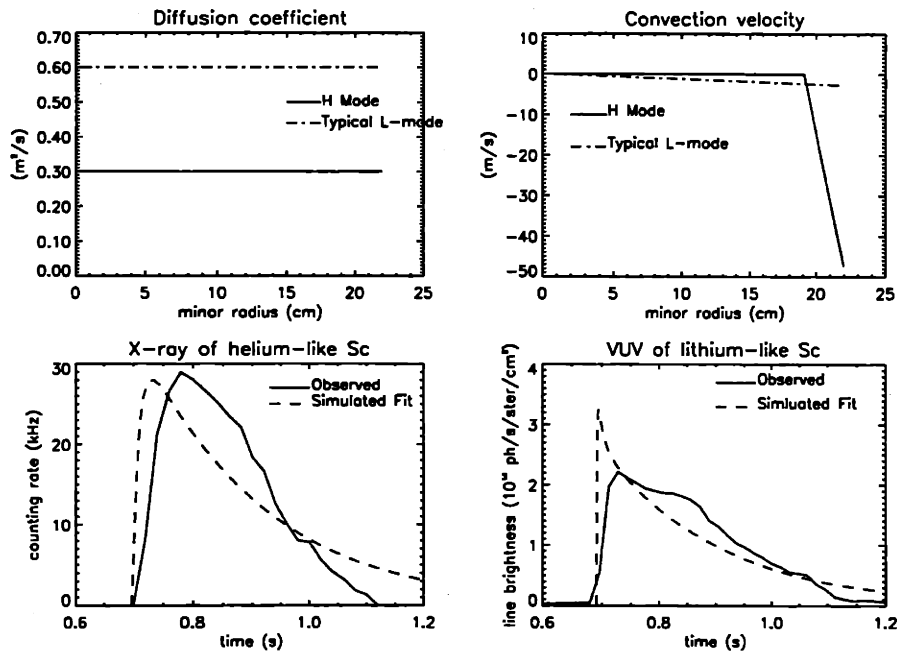
Figure 5-30:   A set of transport efficient profiles tested for fitting H-mode x-ray and VUV signals.   This set shows that a large edge inward convection velocity alone cannot produce satisfactory fits for both the the edge species and the central species' signals.
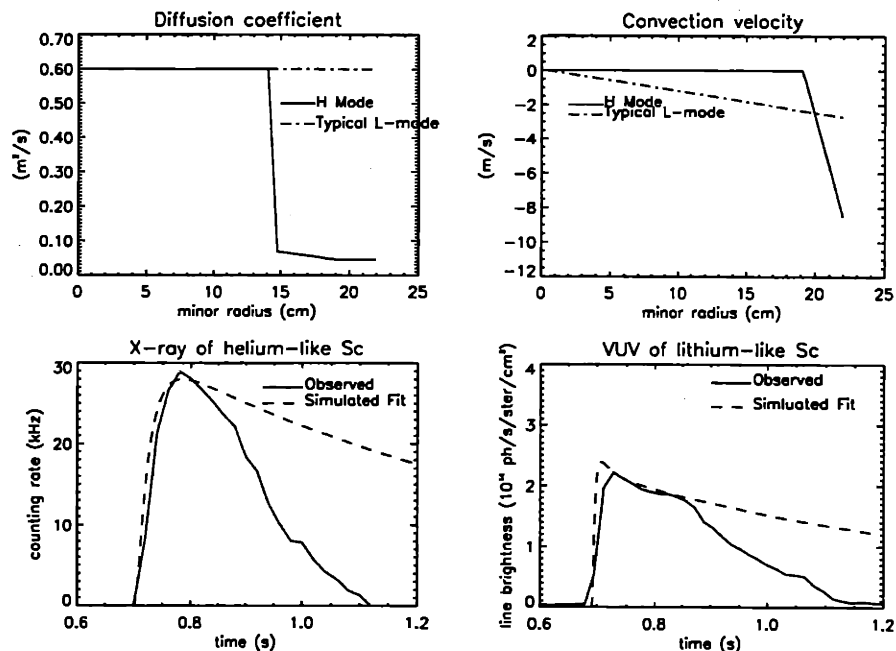
Figure 5-31: A set of transport efficient profiles tested for fitting H-mode x-ray and VUV signals. The fits are sensitive to the magnitude of the inward convection velocity. This set shows that a 50% larger convection velocity would not produce correct fit for the central species' signals despite a factor of 2 increase of the central diffusion coefficient.
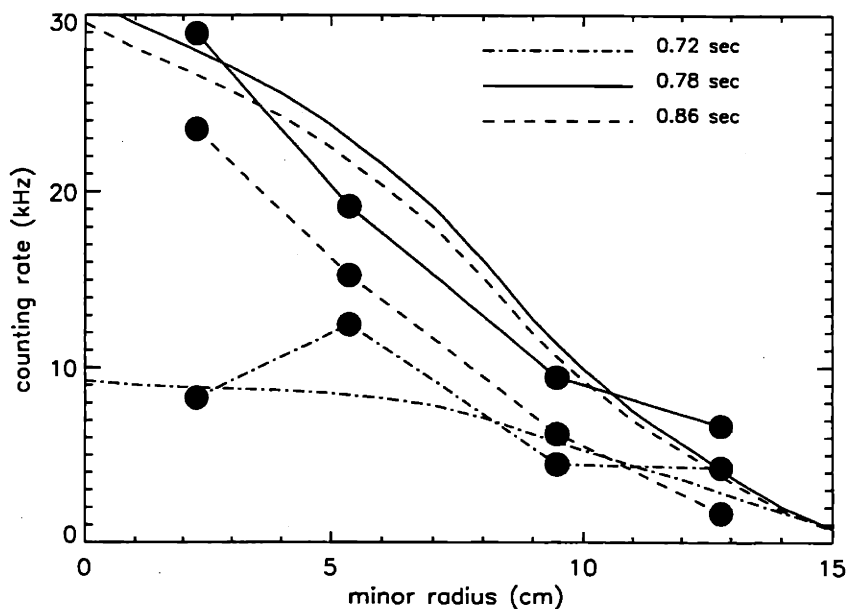
Figure 5-32: Comparison of the observed and simulated radial brightness profiles of helium-like scandium w line x-ray emission. Each set of the lines corresponds to a time point represented by a solid dot in Figure 5-25. The lines with solid dots are the observed radial brightness profile. The ones without dots are the simulated profiles.
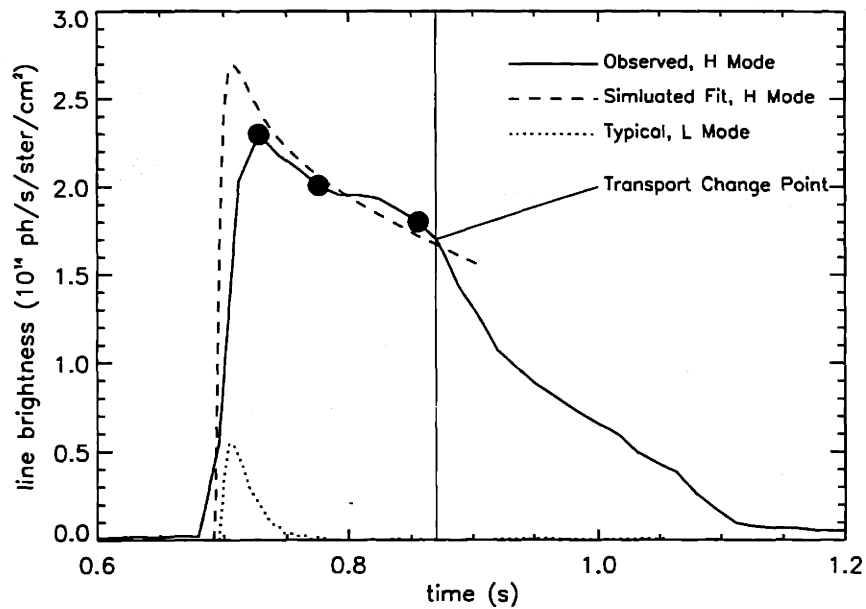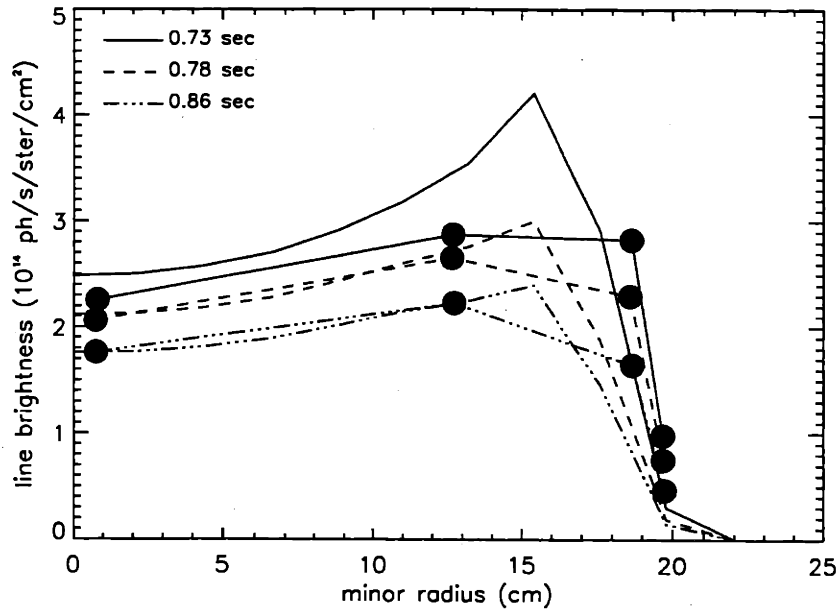
Figure 5-33: Comparison of the observed and simulated radial brightness profiles of lithium-like scandium VUV emission. Each set of the lines corresponds to a time point represented by a solid dot in Figure 5-26. The lines with solid dots are the observed radial brightness profile taken with the McPherson spectrograph. The ones without dots are the simulated profiles.

orbit to another, therefore contributes to the so called "neoclassical transport". The neoclassical transport coefficients are taken in Ref. [58] as:

$$D = \frac{4}{3}\sqrt{2\pi}\rho_b^2 e^4 \frac{\ln \Lambda}{\sqrt{m_b}}(1 + \gamma q^2)T_b^{-3/2}n_b \ ,$$

$$V = \frac{4}{3}\sqrt{2\pi}\rho_b^2 e^4 \frac{\ln \Lambda}{\sqrt{m_b}}(1 + \gamma q^2)T_b^{-3/2}[\frac{Z_j}{Z_b}\frac{\partial n_b}{\partial r} - \frac{n_b}{T_b}\frac{\partial T_b}{\partial r}] \ , \tag{5.4}$$

$$\tag{5.5}$$

where all terms are in cgs units except that T_b is in eV. Here, b denotes the background ion species, j denotes the jth charge state of the impurity, q is the safety factor, ρ is the ion gyroradius, γ is on the order of unity for trace impurities, $\ln \Lambda$ is the Coulomb logarithm, m_b is the mass of the background species atom, T_j is assumed to be the same as T_b. When calculating the neoclassical transport coefficients, the n_b is taken as the same as the n_e for deuterium plasmas and the T_b is taken as:

$$T_b = 3000[1 - (\frac{r}{22.5})^2]^{1.5} \; eV \; , \qquad\qquad (5.6)$$

where r is the minor radius in cm.

Comparisons between the deduced transport coefficients and the neoclassical transport coefficients were also made. Figure 5-34 shows the comparisons between the deduced H-mode transport coefficients and the neoclassical transport coefficients calculated using the electron temperature profile obtained with ECE and the electron density profile obtained with the TCI. Also shown are the typical transport coefficient profiles of L-mode plasmas. It shows that during H-mode, the diffusion coefficient in the plasma center was still comparable in magnitude to the anomalous diffusion coefficient during L-mode. At the edge, i.e. $r/a > 0.7$, H-mode diffusion coefficient decreased to the same level of the neoclassical diffusion coefficient. H-mode convection velocity remained insignificant within $r/a < 0.85$. A large (compared to L-mode) inward convection velocity existed in the region $r/a > 0.85$. This was consistent with the neoclassical convection velocity profile. However, the neoclassical convection velocity was an order of magnitude larger than H-mode convection velocity.

Figure 5-35 shows the fits for the x-ray and the VUV signals generated with the neoclassical transport coefficients. The simulated rise time was too long for the x-ray signals due to the small diffusion coefficient in the center. This suggested that a set of transport coefficients completely in the neoclassical form would not be consistent with the experimental observation. Figure 5-36 shows the fits for the x-ray and the VUV signals generated with the neoclassical convection velocity, anomalous diffusion in the center and neoclassical diffusion at the edge. The rise time of the simulated x-ray signals was close to the experimental value. But the decay time of the simulated x-ray signals was still much larger than the experimental value due to the very large inward neoclassical convection velocity. This suggested that convection velocity in the neoclassical form would not be consistent with the experimental observation. The convection velocity had to be an order of magnitude smaller than the neoclassical value to explain the time evolution of the x-ray and VUV signals.

The analysis of the scandium injections has provided a good understanding of D

Diffusion coefficient

Convection velocity
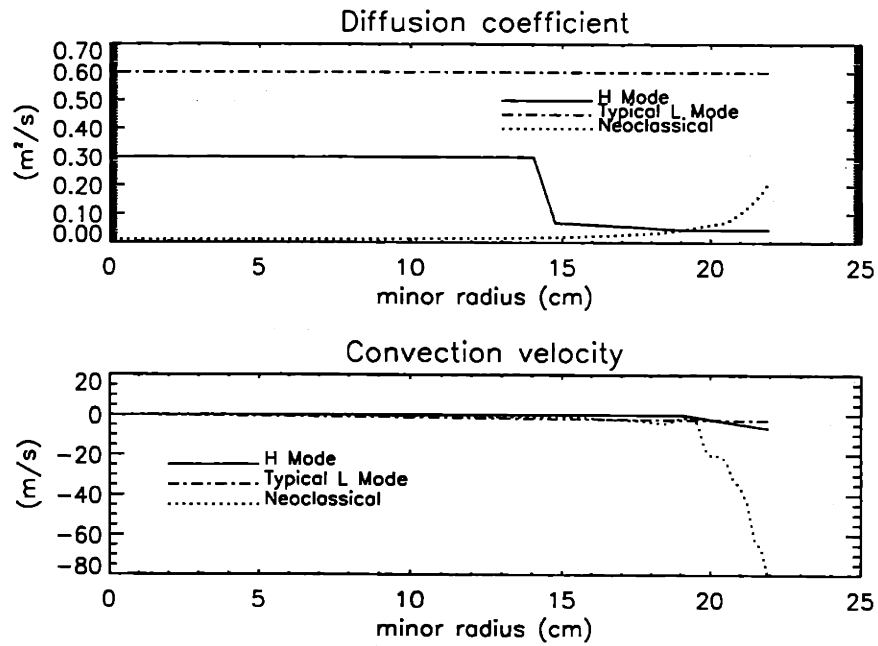
Figure 5-34: Comparison of the deduced H-mode transport coefficients and the neoclassical transport coefficients. Also plotted are the typical L-mode transport coefficient profiles.

Diffusion coefficient

Convection velocity

X-ray of helium–like Sc

VUV of lithium–like Sc
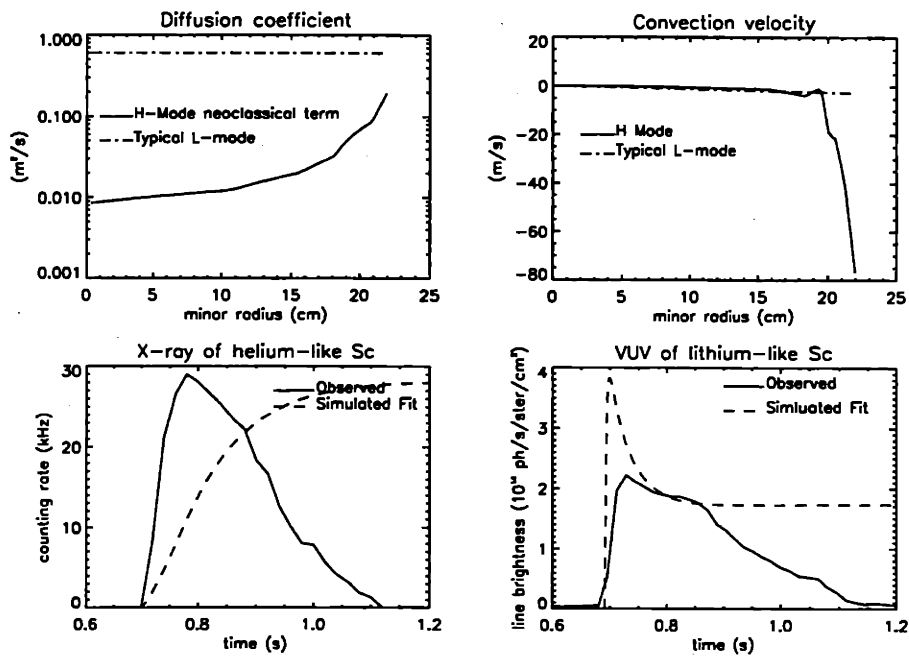
Figure 5-35: X-ray and VUV fits produced using neoclassical transport coefficients.
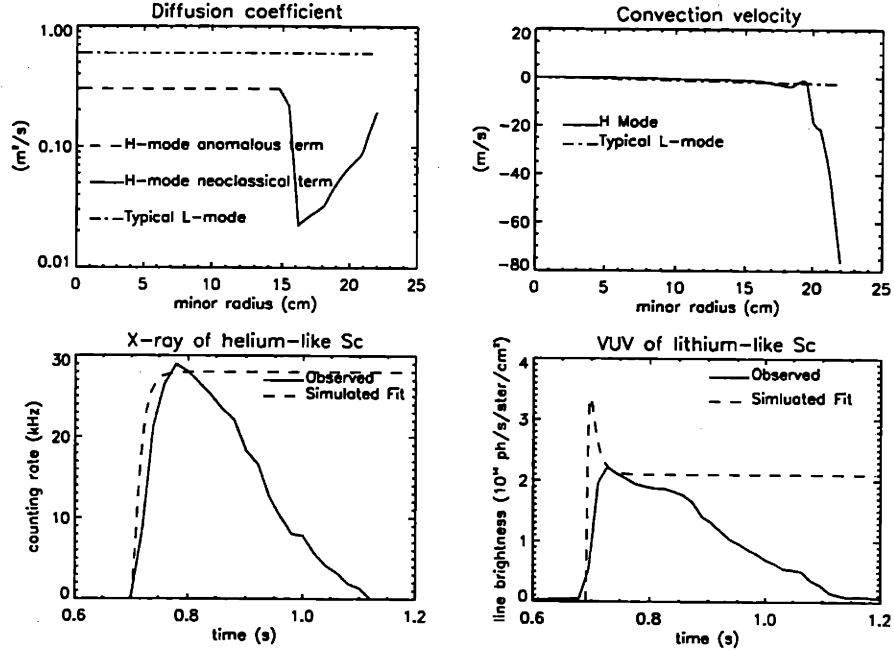
Figure 5-36: X-ray and VUV fits produced using neoclassical convection velocity, anomalous diffusion in the center and neoclassical diffusion in the edge.

and V during H-mode. D and V obtained from scandium injection can then be used to analyze the argon injection data.

In a separate H-mode experiment, argon was injected at 0.3 sec using 20 ms long pulses. The HIREX spectrometers were also scanned on a shot-to-shot basis during a series of almost identical shots. The plasma parameters are the following: $I_p = 1.1MA$, $\bar{n}_e \simeq 1.5 \times 10^{20}\ m^{-3}$ (Ohmic) and $\bar{n}_e \simeq 4 \times 10^{20}\ m^{-3}$ (H-mode), ICRF power of 2 MW were applied in 0.4 second long pulses in addition to ~ 1 MW Ohmic power, $\kappa \simeq 1.6$. ELMy H-modes were achieved during the ICRF heating phase. See Figure 5-37.

Since the w and z line spectra were suspected to be saturated during the H-mode due to high counting rate, the brightness of the intercombination lines: x and y line, were used in the analysis. The transport coefficient profiles inferred from the scandium injection experiment discussed earlier in this section were used in the MIST code to produce fit for the combined brightness profile of x and y lines. The synthetic brightness profile is shown in Figure 5-38, along with the observed brightness. The good agreement between the synthetic profile and the observed one supports the

132
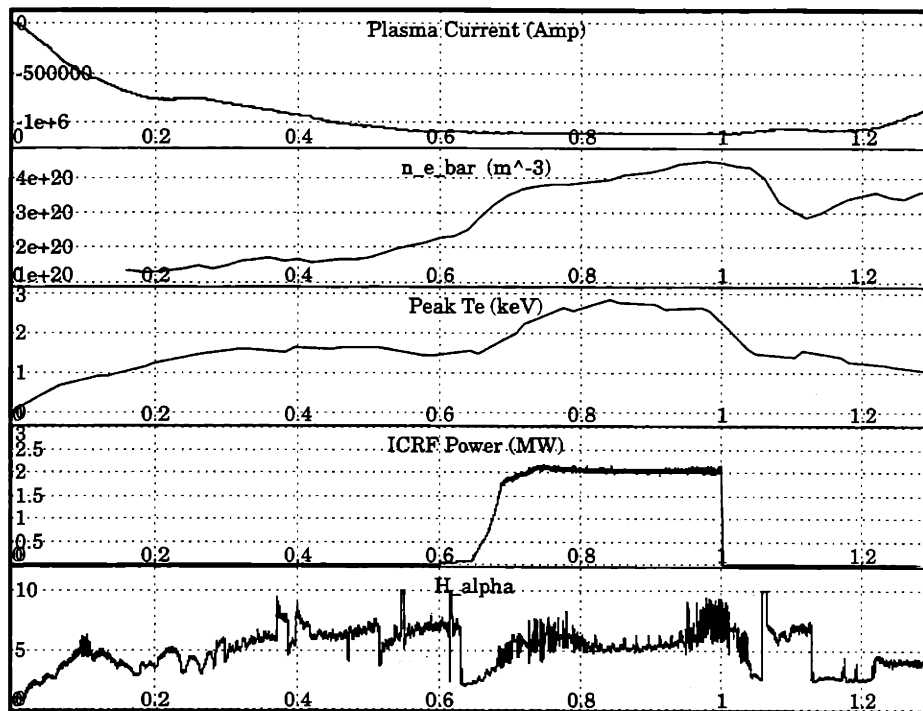
Figure 5-37:   Plasma parameters for H-mode argon injection experiment.

transport coefficient profiles inferred from the scandium injection experiment.

5.5   Change of the Impurity Transport Characteristics during H-mode

In the previous section it was mentioned that the impurity transport changed during H-mode. The impurity particle confinement became noticeably poorer after the change. This phenomenon was observed for all discharges (ELMy and ELM free) of the scandium injection H-mode experiment. Therefore it is worth studying the possible causes that lead to this transport change. Analysis was done for both ELMy and ELM free plasmas.

It was observed that in the ELMy plasmas the impurity particle transport change point coincided with the drop in the plasma stored energy. (See Figures 5-39 and 5-40.) Study of the ELMy H-mode discharges showed that the total radiated power at the transport change points were all at $\sim 1.4\ MW$. (See Table 5.1.) This suggest

133
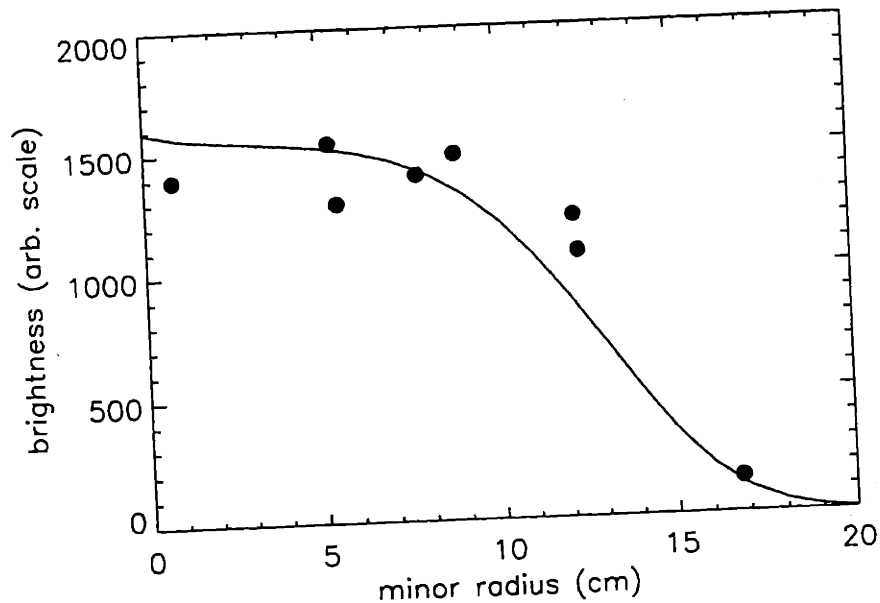
Figure 5-38: Comparison of the combined brightness profile of the intercombination lines and the observed one. It shows a good agreement between the two. Brightness values were integrated over 50 ms intervals.

that 1.4 MW was a threshold over which the energy confinement as well as the impurity particle transport changes in the ELMy H-mode plasmas. The scaling of this threshold is worth studying in the future when the total stored energy, the total input power, etc. are scanned.

In the ELM free plasmas the impurity particle transport change points were observed to follow the drop in the plasma stored energy. (See Figures 5-41 and 5-42.) It suggests that the energy transport change occurred before the impurity particle transport change in the ELM free H-mode plasmas. The drop in the stored energy was also much bigger for the ELM free H-mode than for the ELMy H-mode plasmas, suggesting a bigger change in the energy transport and possibly impurity particle transport. Study of the ELM free H-mode discharges showed that the total radiated power at the transport change points were all at ~ 2.2 MW, as compared with ~ 1.4 MW for the ELMy plasmas. (See Table 5.1.) This suggests that 2.2 MW was a threshold over which the energy confinement changes in the ELM free H-mode plasmas. Like that for the ELMy plasmas, the scaling of this threshold is not currently
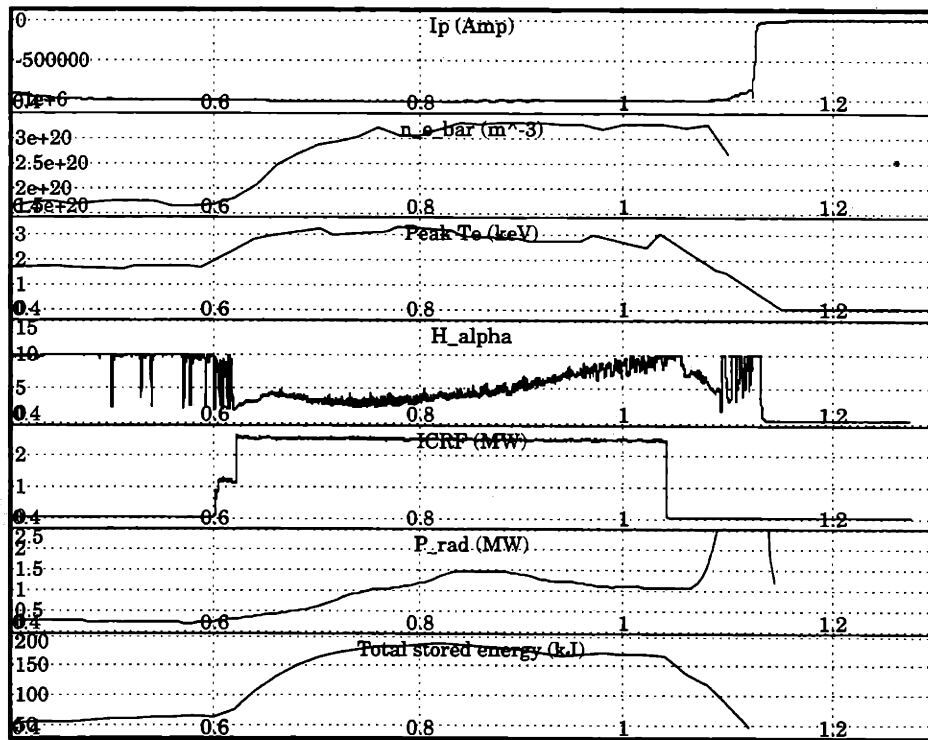
Figure 5-39:   Typical plasma parameters for the ELMy H-mode plasma in H-mode scandium injection experiment discussed in the last section. Notice the spike-like H_α signals which characterize ELMy H-mode.
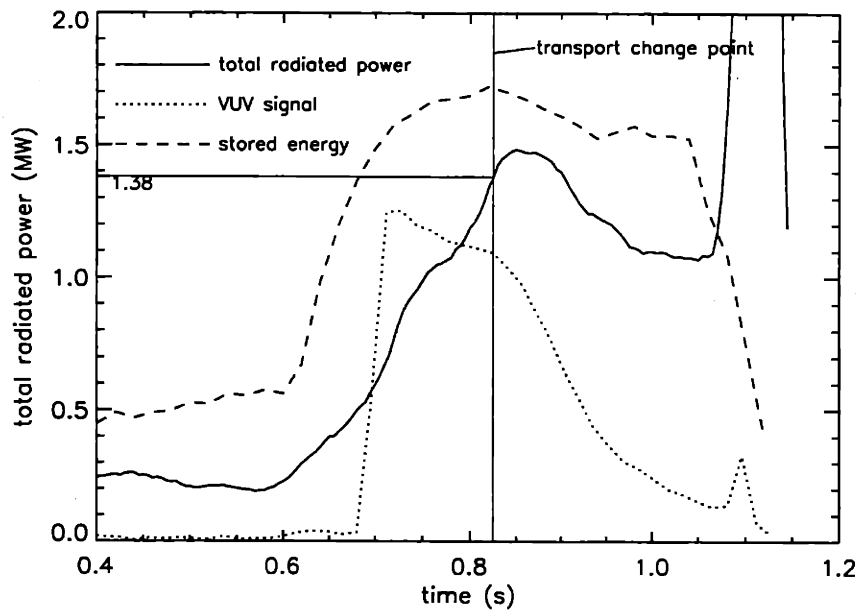
Figure 5-40: Illustration of the impurity transport characteristics change during the ELMy H-mode. The y axis shows the units for the the total radiated power. The traces for the VUV signals and the stored energy are normalized to the scale of the total radiated power in order to compare their time evolution. The vertical line shows the time when the transport change occurred.
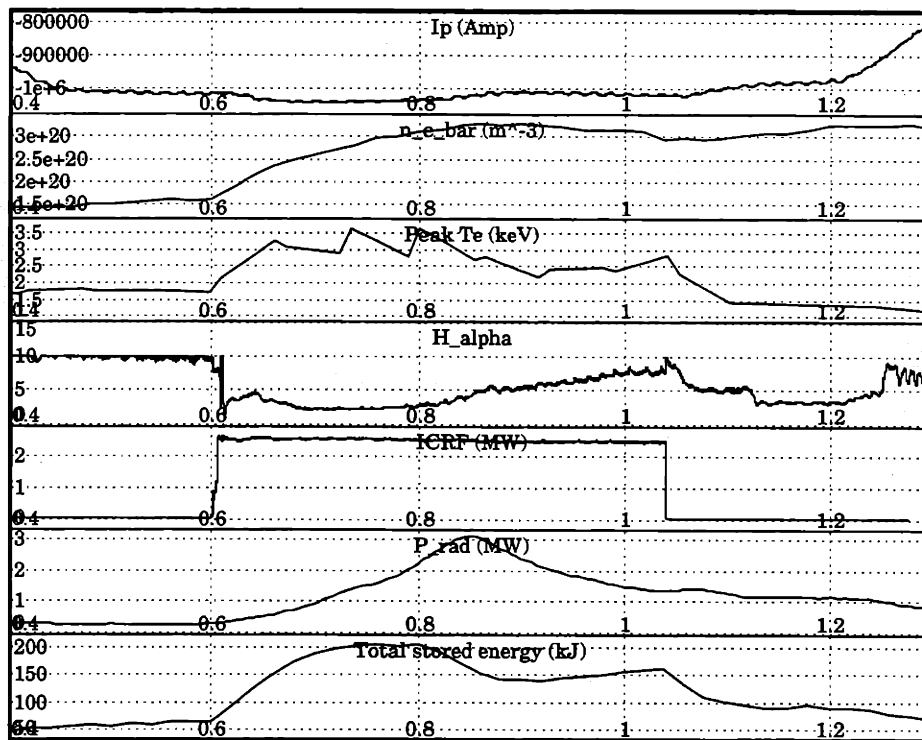
Figure 5-41: Typical plasma parameters for the ELM free H-mode plasma in H-mode scandium injection experiment discussed in the last section. Notice that the H_α signals are relatively free of the ELM spikes.

P_{rad} at the transport change point (MW)	Stored energy (kJ)	P_{in} (MW)	ELMy or ELM free
1.49	183.	3.18	ELMy
1.38	186.	3.22	ELMy
1.46	200.	3.18	ELMy
1.46	190.	3.21	ELMy
2.26	203.	3.10	ELM free
2.21	182.	3.18	ELM free
2.22	200.	3.12	ELM free

Table 5.1: Thresholds of the energy transport change during H-mode.

measured but can be done in the future when more H-mode experiments are carried out.
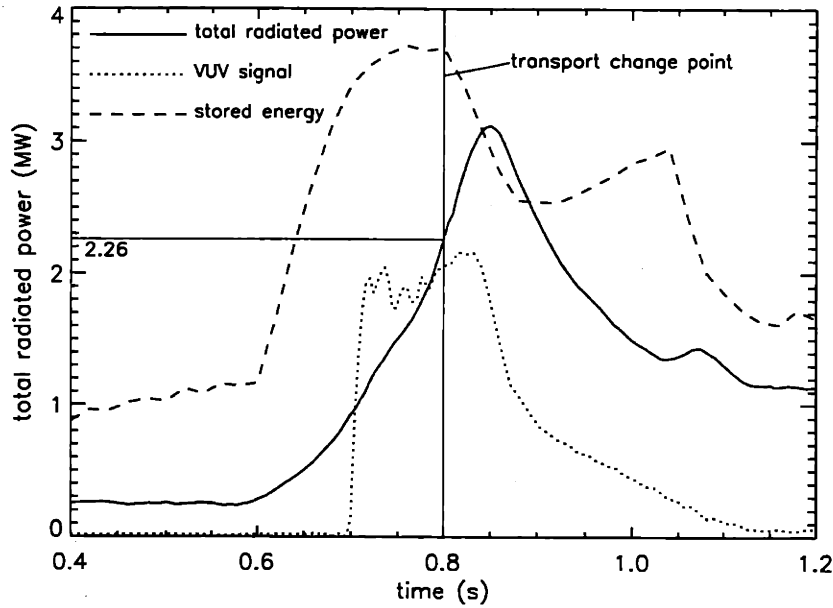
Figure 5-42: Illustration of the impurity transport characteristics change during the ELM free H-mode. The y axis shows the units for the the total radiated power. The traces for the VUV signals and the stored energy were normalized to the scale of the total radiated power in order to compare their time evolution. The vertical line shows the time when the transport change occurred.

Comparisons between the edge electron temperature at the energy transport change point and at the impurity particle transport change point showed that neither the edge electron temperature nor the gradient of the edge electron temperature had a strong corelation with the transport change.

5.6 Discussion

In Section 5.2.1, analysis of the brightness profile of shot 931014005 showed that the synthetic spectra could fit the observed ones by varying the diffusion coefficient and convective velocity at the edge. It is important to verify this in some way. Figure 5-14 shows the argon ion density profiles produced with the MIST code using the non-spatially-constant diffusion coefficient profile along with the argon ion densities produced using a constant diffusion coefficient. Comparison of those two sets of profiles shows that beyond 17 cm, the lithium-like argon density using the non-constant D profile is over 10 times higher than that produced using constant D. This drastic increase of lithium-like argon over the level predicted by a constant D profile can be verified by the McPherson spectrography looking at $2s \rightarrow 2p$ transitions of the lithium-like argon. The atomic modeling is discussed in Section 3.3. Since the $\Delta n = 0$ lithium-like argon ion line emissivity only depends weakly on the electron temperature (see Figure 3-13), the region where the lithium-like argon density is higher contributes more to the line brightness. For a normally hollow lithium-like argon density profile, the outer region of the plasma contributes the most to the lithium-like argon line brightness for the viewing chord that passes near the plasma center. For this reason the McPherson spectrometer measurements provide information about the lithium-like argon density in the outer region. The experiment discussed in Section 4.2 provides evidence that the lithium-like argon density is much higher in some cases (in this case, factor of 4) than that predicted assuming a constant diffusion coefficient. Though this discrepancy might be accounted for by the error ranges of the HIREX and the McPherson measurements, the direction of the discrepancy was consistent with the analysis in Section 5.2.1 and provides evidence that the diffusion coefficient is not spatially constant, in at least some Ohmic cases.

It should be noted, though, that there is another possible cause for the edge concentration of impurities. An up-down asymmetry has been observed on Alcator C-Mod due to a drift in the opposite direction of the ion $B \times \bigtriangledown B$ drift. It is also possible the edge impurity concentration was a result of this asymmetry.

H-mode transport studies done on other tokamaks had shown that while the D behavior varied both quantitatively and qualitatively over a wide range from machine to machine, an inward convection, mainly significant at the edge, was found in most of the studies. The results from the two H-mode experiments discussed in this chapter also confirm this finding. Of the past transport experiments, the one carried out in JET was the closest to the experiments in Alcator C-Mod in terms of experimental methods and data analysis techniques. The JET experiment clearly identified the existence of a large inward convection velocity in a thin layer at the edge. As for the diffusivity, the two machines differed significantly. The Alcator C-Mod D profile decreased at the outer part of the plasma, deduced from a peaked impurity brightness profile. The JET D profile increased at the outer part of the plasma, deduced from a hollow impurity brightness profile. This shows the machine-dependence of the transport process. However, despite the difference in D profiles between Alcator C-Mod and JET, most of the transport changes between L-mode and H-mode occurred at the edge, not the center, for both machines. This suggests that it's the edge parameters, rather than the central ones that change the most in H-mode.

H-mode remains of great interest to the fusion community and the theories are still under development to explain it. The leading hypothesis for the cause of H-mode is that it is due to the development of a radially narrow edge transport barrier with high flow shear which suppresses edge microturbulence driven transport. (Ref. [59] and [60].) This would imply that the diffusion coefficient at the edge would be much reduced from L-mode level of the anomalous diffusion, while stays close to L-mode level in the core where the microturbulence is unsuppressed. The findings of the H-mode experiments in Alcator C-Mod were consistent with that implied by this hypothesis. In fact, it was found that the edge H-mode diffusion coefficient decreased to the neoclassical level. The change in the impurity particle transport and in the energy transport as H-mode evolved was another interesting finding. It seemed that when the radiated power exceeded a certain threshold, the energy and particle confinement became worse. This might be explained by the possibility that the radiation loss reduced the edge flow shear and hence reduced the suppression of the edge mi-

croturbulence driven transport. It would be worth studying the edge flow shear using diagnostics that measures rotations, and correlating the change in the edge flow shear with the transport changes.

5.7 Conclusion

Radial profiles of the impurity transport coefficients (D and V) were studied in this chapter. It was found that the ohmic diffusion coefficient D was spatially variant in the case studied. Though the limited number of viewing chords available prevented the detailed mapping of the D spatial profile, in one of the cases studied, the spatial variation of D was essential for the explanation of the argon x-ray brightness profile. For that case, D was found to decrease as the radius increases. One implication of the profile was that the lithium-like argon should increase by an order of magnitude as compared with that produced with a spatially constant D profile. This was confirmed by the comparison of the VUV and x-ray spectra.

After pellet injection, the argon density profile was found to peak strongly in the center. Further analysis with the MIST code showed that this resulted from a large inward convection velocity, rather than a spatially variant D. A greatly enhanced particle confinement was inferred by the analysis.

A very long impurity particle confinement time during H-mode was found in H-mode studies for both ELMy and ELM free plasmas. In the scandium injection experiment, it was found that when the total radiated power reaches $\sim 1.4 \ MW$ for the ELMy plasmas and $\sim 2.2 \ MW$ for the ELM free plasmas, the energy transport abruptly increased. The point of energy transport change coincided with the point of the impurity transport change for the ELMy H-mode but preceded the impurity transport change point for the ELM free plasma. Even after the transport change which increased both the energy and the impurity particle transport, the impurity particle confinement was still significantly better than that of L-mode, while the energy confinement was not. The transport coefficient profiles were deduced for the period before the transport change point by using the MIST code to simulate the

brightness profiles and the time evolution histories of the central species (helium-like scandium) and the edge species (the lithium-like scandium). It was found that a large inward convection flux exists at the plasma edge ($r/a \geq 0.85$) during H-mode. This finding was consistent with the findings on the other machines. The diffusion coefficient D was found to decrease slightly in the center during H-mode compared to L-mode. But D decreased by an order of magnitude compared to L-mode value in the outer part ($r/a \geq 0.7$) of the plasma, to close to the neoclassical level. The lack of change of the central transport coefficients during H-mode was consistent with the findings on JET and other tokamaks (Ref. [53] — [57]). Argon was injected during another H-mode experiment. Transport coefficient profiles obtained in the scandium injection experiment produced good agreements between the simulated helium-like argon brightness profile and the observations. This provided further support for the findings in the scandium injection experiment.

Impurity transport studies for the Alcator C-Mod H-mod suggested that the edge transport parameters change substantially during H-mode compared to L-mode, while the central transport parameters remained close to L-mode levels.

Chapter 6

Summary and Future Work

6.1 Future Work

Some important questions remain unanswered. In the next two sections, some preliminary studies are presented in hope that they would point out the direction of future research on the subject of impurity screening. Section 6.1.1 presents several types of argon x-ray time histories, suggesting the existence of a "reservoir" for the injected gas somewhere in the vacuum chamber. Section 6.1.2 discusses the need for neutral argon temperature and density measurements from the modeling's point of view.

6.1.1 Argon X-ray Signal Time Histories

Since only several percent of the argon injected reside in the main plasma, the whereabout of the rest of argon is worthy of further study. Evidence from some shots seemed to suggest that there was a "reservoir" for the injected gas somewhere in the vacuum chamber. Time histories of the argon x-ray signal are studied in this section to provide the evidence.

Technique described in Section 3.5 is used in this section to analyze the time history of argon x-ray signals. During a plasma discharge, argon is typically injected by a single square wave pulse at the early part of the discharge ($< 0.5 sec$). The amount of argon in the tokamak is fixed for the rest of the discharge. Figure 6-1

shows a typical time history of the x-ray signal obtained by Hirex scalers, along with time histories of some important plasma parameters. It normally takes around 50 ms for the x-ray signal to start rising after the initialization of the argon pulse. That's when the argon starts diffusing into the center of the plasma where the temperature is high enough to produce a significant amount of helium-like argon emission. The delay is also partially due to a delay time for the gas to get to the edge of the plasma from the injection valve. For a non-recycling impurity, the impurity eventually diffuses out of the plasma and is deposited on the walls. If there is no new injection, the signal will decay nearly to zero. Figure 6-2 is a time history of the x-ray signal of a scandium injection. It takes around 50 ms for the x-ray signal to decay from the maximum to nearly zero. For a recycling impurity like argon, however, the impurity ions diffusing out of the plasma recombine into neutrals on or near the wall and re-enter the plasma. This is equivalent to having a constant source. So the x-ray signals for argon normally reach a steady-state level, remaining approximately constant as long as the plasma density and temperature also remain constant, as illustrated in the trace titled "Central chord He-like argon x-ray" in Figure 6-1 between 0.5 sec and 1.0 sec. This is also demonstrated in Figure 6-3.

However, in some cases, the x-ray signal doesn't remain constant. Figure 6-4 and Figure 6-6 illustrate two opposing cases. Figure 6-4 shows a discharge during which the x-ray signal kept rising until the ramping-down phase while $\bar{n}_e$ and T_e remained approximately constant. Figure 6-5 shows that the central argon density kept increasing during the current flat-top, even when the slight decrease in the electron density and slight increase in the electron temperature as time increased are taken into account. Figure 6-6 shows a discharge during which the x-ray signal steadily decreased after reaching a maximum while $\bar{n}_e$ and T_e remained approximately constant. (Also see Figure 6-7) This suggests that the argon density in the plasma does not stay the same in some cases. There are two explanations for the changes in the argon density in the plasma. One is that the argon screening changed with time in these cases, so out of a fixed amount of available argon, more and more got into the plasma in cases represented by Figure 6-4 while less and less got into the plasma

144

Figure 6-1: Scope plot for steady state argon x-ray signal time history. The scale for the x axis is time in second for all five traces. For the plasma current, the y axis is in Amp. For the $\bar{n}_e$, the y axis is in m^{-3}. for the central T_e, the y axis is in keV. For the x-ray signal, the y axis is the counting rate in kHz. For the argon inject pulse, the y axis is the voltage applied to the pulsed valve in 10 volts.

Figure 6-2: A time history of the helium-like scandium x-ray signals for a scandium injection. Taken with the spectrometer # 4

Figure 6-3: Time history of central argon density for Alcator C-Mod discharge 950127023. The argon injection pulse is also shown. The central argon density remained relatively steady from 0.4 − 1.0 second.

in cases represented by Figure 6-6. Another possible reason for the changing argon density is that there was not a fixed amount of argon in the vacuum vessel. The walls might pump away a certain amount of argon. The argon signal is lower in the first argon shot during each run day because the walls are clean of argon. But as the walls get saturated with absorbed argon, it is assumed that they no longer pump the argon in the region between the walls and the LCFS and all the argon injected remains in the vacuum vessel as potential source of impurity. But this is not necessarily true. In the case of Figure 6-4, it seemed that argon was constantly being added into the vacuum vessel. Since no argon was injected from the external source after the argon pulse at 0.3 second, the extra argon must came from within the tokamak itself. The possibilities were that either the walls were releasing the argon it absorbed earlier or some of the argon injected in the 0.3 second pulse was stored in some location without contributing to the impurity penetration at first. Unfortunately, there was no measurement of the spatial distribution of the argon density to provide verification for either speculation. This problem calls for direct measurement of the spatial neutral argon density distribution.

For the case of Figure 6-6, similar speculations arise. The walls might have already released some of the argon they absorb between shots and were no longer saturated. Wall pumping during the shot reduced the total amount of free argon and hence the x-ray signal. Also it was possible that the argon was constantly pumped to a certain part of the tokamak other than the walls, e. g. the divertor area. To verify these speculations, direct measurement of the spatial argon density distribution is also required.

Similar question was also raised in DIIID experiments([61]). In DIIID, neon was injected using a long pulse ($\sim 1s$) while a cryo-pump provided pumping at a known rate in the divertor region. Neon density profile in the plasma were measured by a neutral beam diagnostic. Neutral (not just neutral neon) pressure were measured both in the private flux region and midplain. The neon pumping rate was also measured. It was found that the sum of the total amount of neon in the main plasma and the total amount of neon pumped out was smaller than the injected amount in the early
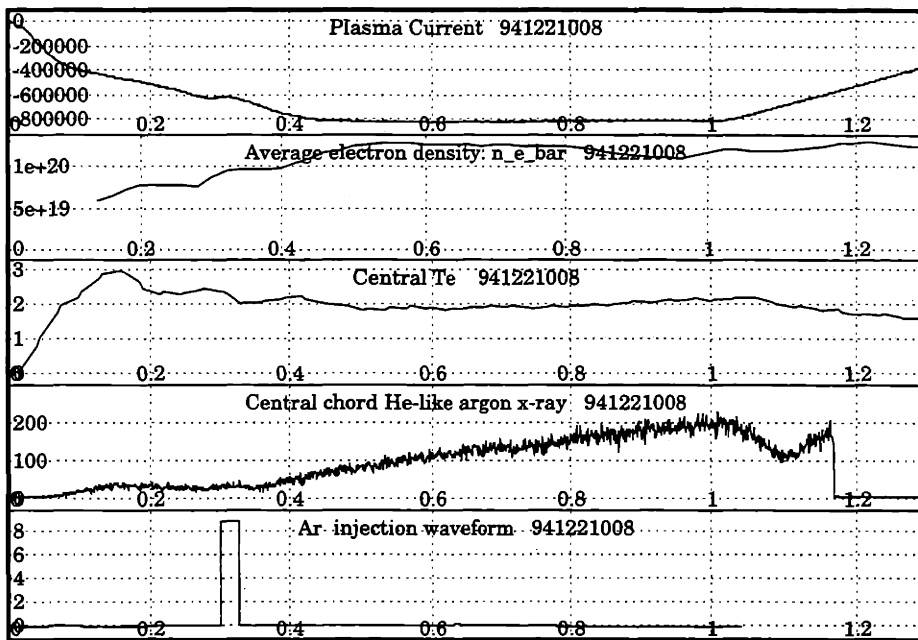
Figure 6-4: Scope plot for rising argon x-ray signal time history. The scale for the x axis is time in second for all five traces. For the plasma current, the y axis is in Amp. For the $\bar{n}_e$, the y axis is in m^{-3}. for the central T_e, the y axis is in keV. For the x-ray signal, the y axis is the counting rate in kHz. For the argon inject pulse, the y axis is the voltage applied to the pulsed valve in 10 volts.
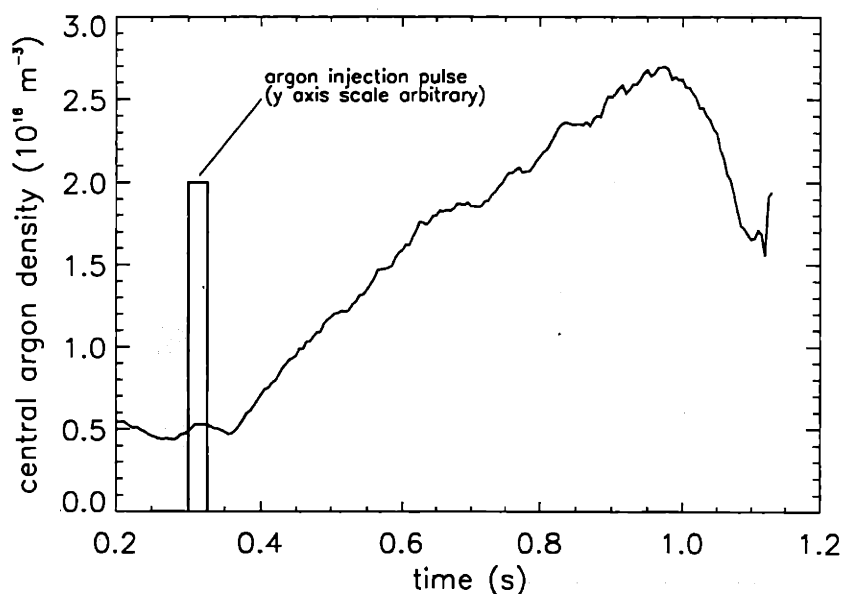
Figure 6-5: Time history of central argon density for Alcator C-Mod discharge 941221008. The argon injection pulse is also shown. The central argon density increased steadily until 0.95 second.

phase of the injection. Neon could not be completely accounted for even if all the neutrals outside of plasma were taken to be neutral neons. However, in the later phase of the injection, all injected neon could be accounted for. This suggested some kind of storage mechanism also existed for gaseous impurities in DIIID.

6.1.2 Modeling's Need for Neutral Argon Temperature and Density Measurements

Two of the assumptions the simple model makes are that 1) all the injected argon exists either in the plasma as impurity ions or in the vacuum chamber surrounding the plasma as neutral gas, and that 2) the neutral argon gas is evenly distributed in density and temperature throughout the vacuum chamber. These assumptions are of course not necessarily correct. It has been observed that the first discharge during a day's operation with argon injection normally shows lower argon density in the plasma than the subsequent discharges. This phenomenon cannot be explained by a lower penetration, since mostly the first plasma discharge with argon injections normally is
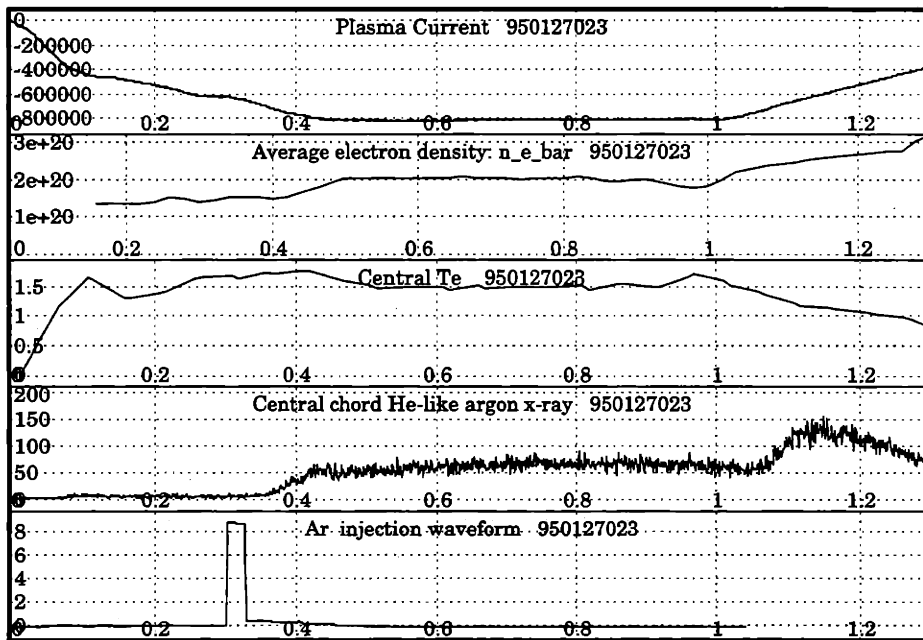
149
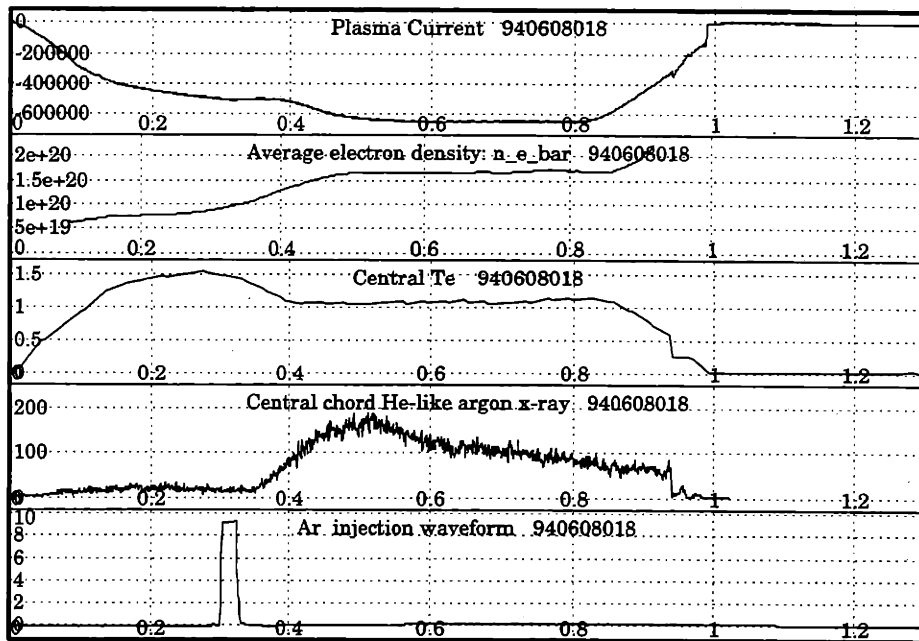
Figure 6-6: Scope plot for decaying argon x-ray signal time history. The scale for the x axis is time in second for all five traces. For the plasma current, the y axis is in Amp. For the $\bar{n}_e$, the y axis is in m^{-3}. for the central T_e, the y axis is in keV. For the x-ray signal, the y axis is the counting rate in kHz. For the argon inject pulse, the y axis is the voltage applied to the pulsed valve in 10 volts.
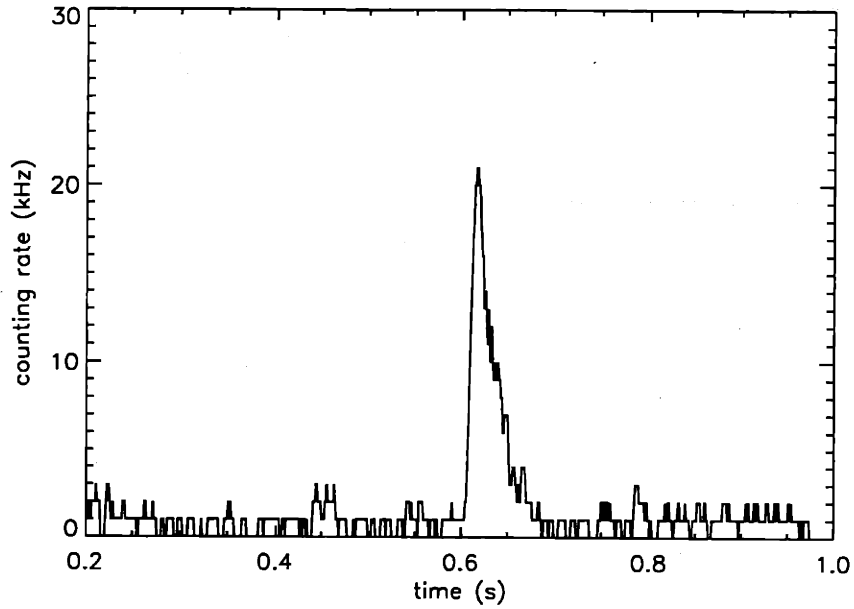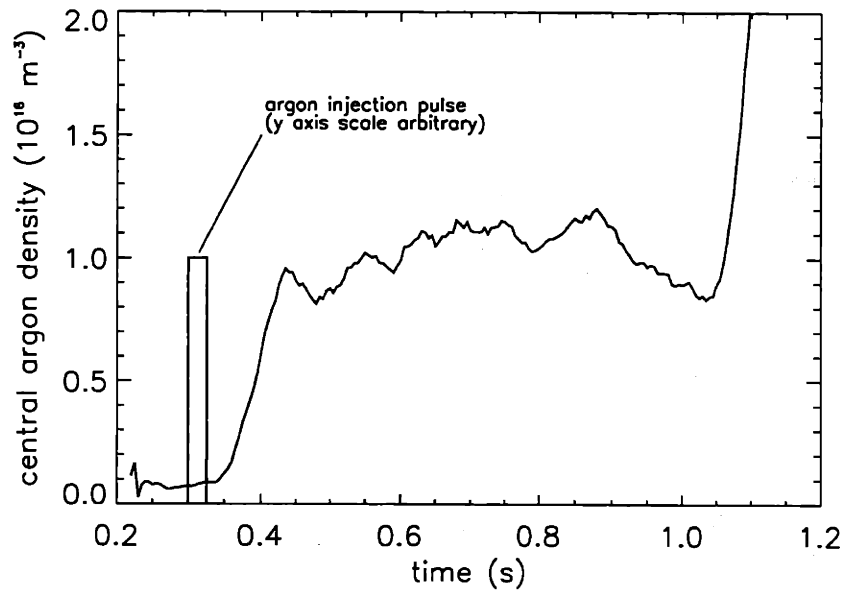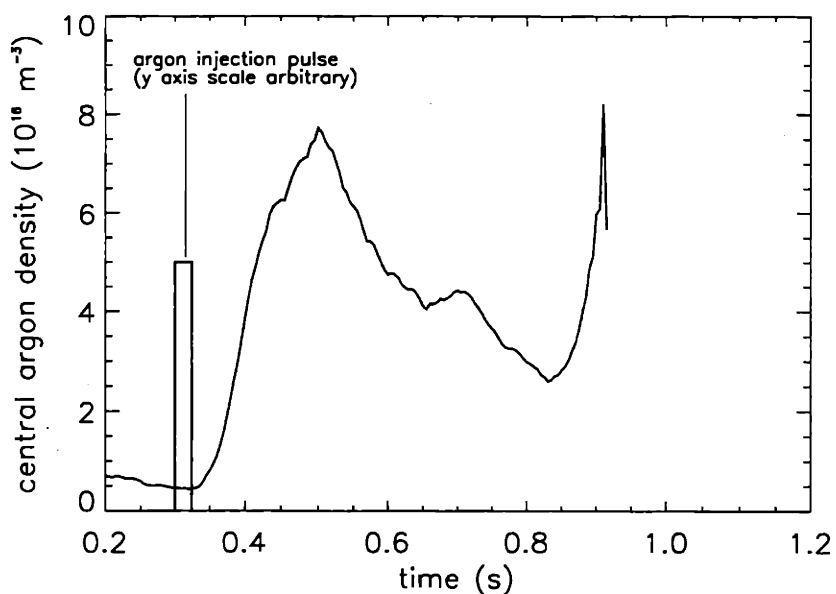
Figure 6-7: Time history of central argon density for Alcator C-Mod discharge 940608018. The argon injection pulse is also shown. The central argon density decreased after reaching a maximum at 0.5 second.

not very different from other discharges. One possible explanation may be the effects of wall pumping, which reduces the amount of argon in the form of neutral gas. For the subsequent discharges, the wall is assumed to be saturated with the argon from the first discharge with argon injection and hence comes the first assumption. But this might not be true. The wall may lose some of the argon adhering to it between discharges and therefore part of the argon injected is lost due to wall pumping in every discharge, albeit not as much as the first one. Also, if the continuously decaying time history in Figure 6-6 is caused by the wall pumping, then the argon is not 100% recycling as previously thought. So in order to further test the validity of not only this model, but in fact any model, measurement of actual neutral argon gas density is necessary.

The second assumption, which assumes the uniformity of the neutral argon gas, is less plausible. One would naturally expect the neutral argon density to be higher in the divertor region, similar to the behavior of neutral deuterium. If a significant amount of argon penetrates into the plasma from a place other than in the vicinity

of the divertor region, it is important to know how the neutral argon is distributed in order to model it correctly. This again suggests that, in the future, measurement of the argon density in various locations should be done.

Another unknown in the model is the temperature of the neutral argon. The higher the temperature, the higher the velocity of the incident neutral particles and therefore the higher the chance that they penetrate into the core plasma. It would be of great help to the modeling of the impurity screening if the neutral impurity's temperature and density are measured.

6.1.3 Conclusion

Experimental results suggested that certain storage mechanism for gaseous impurities existed in the vacuum chamber. Measurements (possibly with laser florescence) of the spatial distribution of the neutral impurities are therefore needed to study the impurity screening problem further. Moreover, from the modeling's point of view, the neutral argon's temperature and density strongly affect the penetration efficiency. Experimental measurements of these quantities are needed for further studies on impurity penetration modeling.

6.2 Summary

In this thesis, two aspects of the impurity transport problem in tokamaks were discussed. 1) transport coefficient (D) and (V), 2) impurity screening. Simulations of the brightness profile and/or the brightness time history were done using the MIST transport code to find the transport coefficients that produced the best fits. It was found that, in at least some cases, the diffusion coefficient, D, was spatially variant for ohmic plasmas. For the case studied, D decreased as the radius increases. One implication of this D profile was the one-order-of-magnitude increase of lithium-like argon density at the edge compared to that calculated with a spatially constant D. This was consistent with the observation of four times higher signal on the VUV spectrometer, which took lithium-like argon spectrum, than what would have been if

the density profile deduced using x-ray spectrometer data and MIST-produced profile with a constant D. Following the injection of pellets, a large inward convective velocity V was also found.

Scandium was injected during long H-mode period. Brightness profile and time history of both helium-like scandium and lithium-like scandium were simulated using the MIST code. It was found that the impurity particle confinement improved substantially during the H-mode. D was found to drop by a factor of 2 in the inner part of the plasma ($r/a \leq 0.7$) and by an order of magnitude in the outer part to the neoclassical level. A large inward convection flux was also found to exist at the edge ($r/a \geq 0.85$). Transport coefficients obtained from the argon injection experiments were consistent with that obtained from the scandium injection.

In one H-mode experiment, it was found that when the total radiating power reaches ~ 1.4 MW for the ELMy plasmas and ~ 2.2 MW for the ELM free plasmas, the energy transport abruptly increased. The point of energy transport change coincided with the point of the impurity transport change for the ELMy H-mode but preceded the impurity transport change point for the ELM free plasma. Even after the transport change which increased both the energy and the impurity particle transport, the impurity particle confinement was still significantly better than that of the L-mode.

The transport studies results suggested that the edge transport parameters changed substantially during the H-mode compared to the L-mode while the central transport parameters remained at the L-mode level. This showed the importance of the edge processes to the H-mode.

Due to the complexity of the geometry of the diverted plasmas, this thesis tried to study the impurity screening problem on two fronts: through empirical scaling and through modeling. The divertor-versus-limiter studies were carried out by toggling the plasmas between limited on the inner wall and diverted at several plasma densities. The studies showed that at various densities argon penetration in the diverted plasmas was significantly lower than that in the limited plasmas, due to the higher edge electron density and temperature as measured by the Fast Scanning Probe. This

confirmed one advantage of the divertor concept. For diverted plasmas, divertor target plate strike point scan and outer gaps scan were carried out and the argon penetration showed no dependence on divertor target plate strike point locations or outer gaps. Data were also compared for ohmic heated plasma and for plasmas when ICRF heating were applied. The study showed that argon penetration was also independent of the heating modes (ICRF versus ohmic). An argon penetration scaling was found to be in the form of $p \propto 1/\bar{n}_e$ for Ohmic and L-mode plasmas. The total amount of argon within the LCFS during the H-mode was found to be a factor of 5 higher than that during the L-mode. But after taking into account of the one-order-of-magnitude increase of the impurity particle confinement time during the H-mode, the screening ability of the SOL did not change significantly during the H-mode. The higher impurity content was mostly due to the longer impurity particle confinement time during the H-mode. The 1-D model developed in Section 4.2.2 was an attempt to provide some insight into the physical mechanism responsible for the observed behavior. A formula (Equation 4.14) relating the argon penetration with the plasma edge parameters was developed. Results calculated using this model were consistent with the experimental observations. Study of the model also suggested the need for direct measurement of the spatial distributions of the neutral argon temperature and density.

Appendix A

Calibration for HIREX and the Argon Injection System

A.1 HIREX Calibration

For each individual spectrometer of the high resolution x-ray spectrometer array, wavelength and line of sight location were calibrated. The calibration process is described in this section.

The wavelength was calibrated by setting the crystal at the built-in home position, at which the Bragg angle is known. A laser beam was then shined from the entrance slit at the center of the crystal. The exit arm was moved so that the reflected laser beam was positioned at the exact middle of the detector. The voltage at the attached potentiometer was recorded as a reference. Then the exit arm was moved to various positions. The voltage and the corresponding step numbers made by the stepper motor were recorded. The voltage versus position and number of steps versus position information were then converted to voltage versus wavelength and number of steps versus wavelength. When wavelength change is needed, present wavelength information is obtained by reading the voltage. Then the number of steps needed to reach the new wavelength is calculated and sent to a pulse generator which sends a series of pulses to the stepper motor controller which controls the stepper motor to make the exact number of steps required.

Vertical position was calibrated by putting a screen where the plasma center is supposed to be and shining a laser beam from the center of the detector to the center of the crystal then through the slit onto the screen. Voltage was recorded from the potentiometer attached to the mounting plate of the spectrometer. The rest of the calibration process is similar to that for the wavelength setting.

A.2 Argon Injection System Calibration

Argon is normally injected through a pulse gas valve. The number of atoms injected into the plasma was deduced by calibrating the injection valve. The calibration was done by connecting the valve to a vacuum chamber of known volume. The flow rate was calculated by measuring the pressure change after an argon pulse. In Figure A-1 the flow rate is plotted versus the plenum pressure for three different voltages applied to the valve.
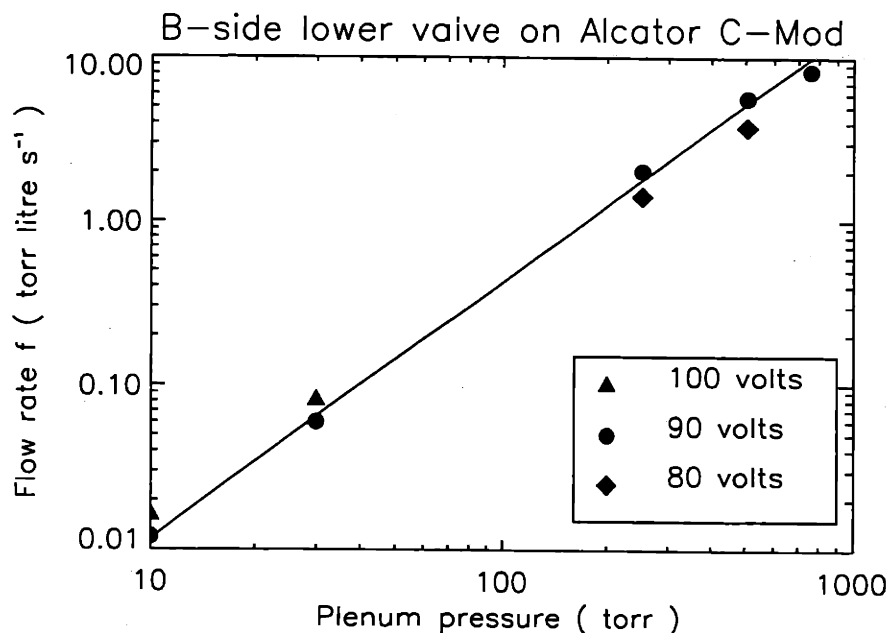
Figure A-1: Flow rate versus plenum pressure for the valve used in argon injection experiments on Alcator C-Mod

The relation between the flow rate f through the valve and the plenum pressure p is found as follows:

$$f = 3.2 \times 10^{-4} p^{1.56} \ \ torr \cdot l \cdot s^{-1} \ , \tag{A.1}$$

where p is in *torr*.

This relation is obtained for 90 volts, which is the normal voltage used in Alcator C-Mod operations, applied to the pulsed valve. To calculate the flow rate of the valve when a voltage other than 90 volts is applied to it, the following formula can be used:

$$\frac{df}{dv} = 9.5 \times 10^{-6} p^{1.6} \ \ torr \cdot l \cdot s^{-1} \cdot volt^{-1} \ . \tag{A.2}$$

See Figure A-2. Thus:

$$f(v) = f(90 \ volts) + 9.5 \times 10^{-6} p^{1.6} (v - 90) \ , \tag{A.3}$$

where v is the voltage applied to the valve expressed in volts.
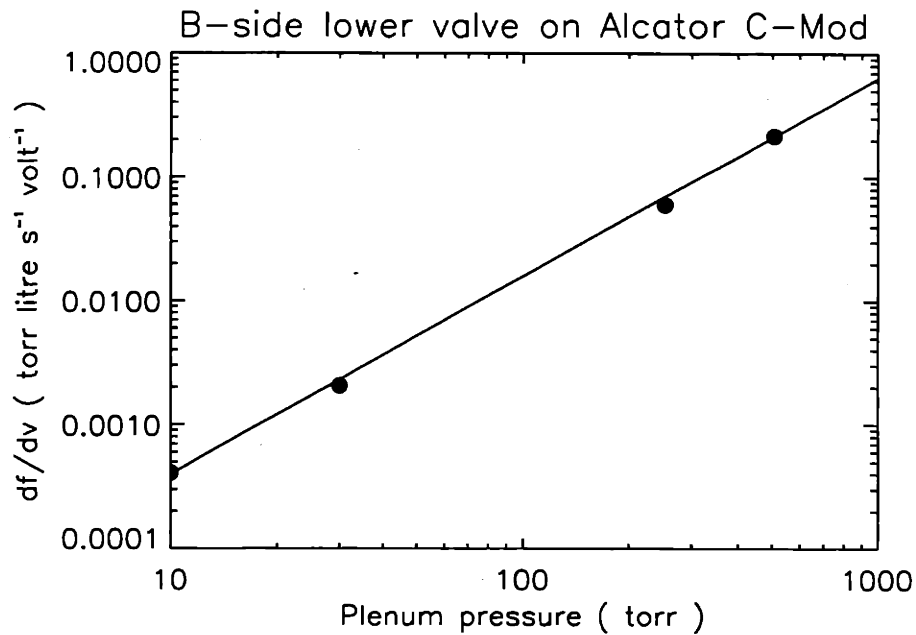
Figure A-2: $\frac{d(flow\ rate)}{d(voltage)}$ versus plenum pressure for the valve used in argon injection experiments on Alcator C-Mod

The number of argon atoms can be deduced from the flow rate of the valve and the pulse length.

Appendix B

Rate coefficients for major population mechanisms

The rate coefficients for major population mechanisms for the helium-like argon are described in this chapter. For more detailed description of the helium-like rate coefficients of some other elements, refer to Ref. [23].

Collisional Excitation

The rate coefficient for excitation by electron impact from ground level g to higher level k with excitation energy of E_{gk} is, ([23]);

$$
\begin{aligned}
S_{gk} &= (\frac{8kT_e}{\pi m_e})^{1/2} y^2 \frac{\pi a_0^2 E_H}{w_g E_{gk}} \int_1^\infty \Omega(U) e^{-yU} dU \\
&= 8.00 \times 10^{-14} \bar{\Omega}(y) T_e^{-1/2} e^{-y} \ m^3 s^{-1} ,
\end{aligned}
\tag{B.1}
$$

where

$$
\bar{\Omega}(y) = y e^y \int_1^\infty \Omega(U) e^{-yU} dU .
\tag{B.2}
$$

Here $y = E_{gk}/T_e$; T_e is the electron temperature in eV; a_0 is the first Bohr radius of the hydrogen atom; m_e is the electron rest mass; E_H is the hydrogen atom ionization energy (13.6eV); w_g is the statistical weight of the initial level; $U = E/E_{gk}$ is the initial energy of the impinging electron in terms of the excitation energy; $\bar{\Omega}(y)$ is the

Element	Z	$a_{gm'}$	$a_{g1'}$	a_{gm}	$a_{g2} = a_{g1} = a_{g0}$
Ar	18	0.498	0.454	0.553	0.496
Sc	21	0.478	0.433	0.534	0.473

Table B.1: Screening numbers for excitation from the ground state of helium-like ions of argon and scandium.

average of the collision strength, $\Omega(U)$, over the Maxwellian distribution of electron energy. $\bar{\Omega}(y)$ can be approximated by an empirical formula ([23]) in the form of;

$$\bar{\Omega}(y) = A + (By - Cy^2 + Dy^3 + E)f(y) + (C + D)y - Dy^2 , \qquad \text{(B.3)}$$

where f is defined as;

$$f(y) = e^{-y}E_1(y) , \qquad \text{(B.4)}$$

and $E_1(y)$ is defined as;

$$E_1(y) = \int_1^\infty z^{-1}e^{-yz}dz . \qquad \text{(B.5)}$$

f can be approximated as;

$$f(x) = \ln(\frac{x+1}{x}) - \{0.36 + 0.03(x + 0.01)^a\}(x + 1)^{-2} , \qquad \text{(B.6)}$$

in which $a = 0.5$ $(x \geq 1)$ or $a = -0.5$ $(x < 1)$.

The coefficients A, B, C, D and E are taken from Table 1. of Ref. [62]. In that table, these coefficients are given in the form of $A^* = Z_{gk}^2 A$, $B^* = Z_{gk}^2 B$, $C^* = Z_{gk}^2 C$, $D^* = Z_{gk}^2 D$, $E^* = Z_{gk}^2 E$, where $Z_{gk} = Z - a_{gk}$ is the effective charge number of the ion for transition $g \to k$. The screening numbers, a_{gk}, are given in Table B.1 for argon and scandium.

Cascade effects. When the contributions from cascading from higher($n > 2$) excited levels following excitation from the ground state are taken into account, we find the total excitation coefficients with the cascade effect taken into account as:

$$S'_{g1'} = 1.05 S_{g1'} \; , \tag{B.7}$$

$$S'_{gm'} = 1.11 S_{gm'} \; , \tag{B.8}$$

$$S'_{gk} = 1.065 S_{gk} \; (k = 0, 1, 2) \; , \tag{B.9}$$

$$S'_{gm'} = S_{gm} + 0.4(S_{g2} + S_{g1} + S_{g0})e^{-0.16\chi_z/T_e} \; , \tag{B.10}$$

where χ_z is the ionization energy given by:

$$\chi_z = 13.6 n_z^{-2}(Z - a_i)^2 \; eV \; . \tag{B.11}$$

n_z is the principle quantum number of the outer electron shell. $n_z = 1$ for helium-like ions; a_i is an effective screening number; $a_i = 0.593$ for argon [23] and 0.573 for scandium.

Collisional excitation and de-excitation between $n = 2$ excited states

The formula of the rate coefficients for collisional excitation $i \to k$ is given in Ref. [23] as;

$$S_{ik}^e = 9.28 \times 10^{-13}(Z - 1)^{-2}T_e^{-1/2}[a_{ik} + b_{ik}f(y_{ik})]e^{-y_{ik}} \; m^3 s^{-1} \; , \tag{B.12}$$

where

$$y_{ik} = E_{ik}/T_e = 8.62 \times 10^{-5}c_{ik}/T_e \; , \tag{B.13}$$

and $f(y_{ik})$ is defined by Equation 3.22. $a_{m'1'} = 4.6$, $b_{m'1'} = 3.2$, $b_{m0} = 0.33$, $b_{m1} = 0.96$, $b_{m2} = 1.7$ are suitable for both argon and scandium. The other values of a_{ik} and c_{ik} are listed in Table B.2, T_e is in eV.

The expression for the rate coefficients by proton impact excitation and α-particles impact excitation is taken from Ref. [23] as;

$$S_{ik}^x = A_x \exp(-B_x/T_x)S_{ik}^e(T_e = T_x) \; , \tag{B.14}$$

160

Element	Z	a_{m2}	a_{m1}	a_{m0}	$c_{m'1'}$	c_{m2}	c_{m1}	c_{m0}	A_p	B_p/Z
Ar	18	5.7	2.2	-0.04	1.748^5	2.567^5	2.251^5	2.176^5	4.80	9.48^1
Sc	21	5.1	1.6	0.20	2.291^5	3.349^5	2.734^5	2.602^5	5.08	8.97^1

N. B. Superscript indicate the power of 10 by which the appropriate number should be multiplied. e. g. $1.748^5 = 1.748 \times 10^5$, etc.

Table B.2: Parameters for excitation between $n = 2$ levels in the helium-like argon and scandium ions.

where the symbol x denotes either protons as p or α-particles as α; T_p and T_α are the kinetic temperatures of the protons and the α-particles. The coefficients for protons used in Equation B.14 are listed in Table B.2. Those for the α-particles are approximated ([23]) by:

$$A_\alpha = 0.152(Z-1)^{1.056}, \quad B_\alpha = 1.11 \times 10^2 (Z-1)^{1.073} . \tag{B.15}$$

Therefore the total excitation rate is:

$$S_{ik} = S_{ik}^e + \frac{N(H^+)}{N_e} S_{ik}^p + \frac{N(He^{++})}{N_e} S_{ik}^\alpha . \tag{B.16}$$

For each collisional excitation process $i \rightarrow k$, there is a collisional de-excitation process $k \rightarrow i$, whose rate coefficient is given as a function of the collisional excitation rate coefficient as;

$$S_{ki} = (w_i/w_k) S_{ik} \exp(E_{ik}/T_x) , \tag{B.17}$$

where $x = e$, p, or α; w_i and w_k are the statistical weights of levels (i) and (k), E_{ik} is the transition energy of the transition $i \rightarrow k$ in eV.

Radiative transitions

Rate coefficients A_{ki} for spontaneous transitions $k \rightarrow i$ are listed in the Table B.3 for argon and scandium. At the density of interest, the radiative induced transitions between levels play insignificant roles and therefore are ignored here.

Radiative recombination The total rate coefficients for radiative recombination to level (k) is;

Element	Z	$A_{m'g}$	$A_{1'g}$	A_{mg}	A_{2g}	A_{1g}	$A_{1'm'}$	A_{2m}	A_{1m}	A_{0m}
Ar	18	4.04^8	1.10^{14}	4.81^6	3.14^8	1.65^{12}	9.50^7	3.41^8	2.66^8	2.43^8
Sc	21	9.35^8	2.09^{14}	2.32^7	1.23^9	5.94^{12}	1.90^8	6.07^8	3.26^8	2.95^8

Table B.3: Spontaneous radiative transition probabilities for $n = 2$ levels of helium-like ions.

$$\alpha^{r\,'}_{ck} = \alpha^r_{ck} + \Delta\alpha^r_{ck} \,, \tag{B.18}$$

where α^r_{ck} is the direct recombination rate and $\Delta\alpha^r_{ck}$ is from cascading from higher levels ($n > 2$). The expressions for α^r_{ck} and $\Delta\alpha^r_{ck}$ are given in Ref. [23] as (expressed in $m^3 s^{-1}$);

$$\alpha^r_{cm} = 1.4 \times 10^{-20} z^{1.8} T_e^{-0.4},$$
$$\Delta\alpha^r_{cm} = 3.6 \times 10^{-20} z^{2.2} T_e^{-0.6} \,, \tag{B.19}$$

$$\alpha^r_{ck} = 5.1 \times 10^{-20} (w_k/9) z^{2.4} T_e^{-0.7},$$
$$\Delta\alpha^r_{ck} = 2.2 \times 10^{-20} (w_k/9) z^{2.8} T_e^{-0.9} \,, \tag{B.20}$$

$$\alpha^r_{cm'} = 5.0 \times 10^{-21} z^2 T_e^{-0.5},$$
$$\Delta\alpha^r_{cm'}/\alpha^r_{cm'} \simeq \Delta\alpha^r_{cm}/\alpha^r_{cm} \,, \tag{B.21}$$

$$\alpha^r_{c1'} = 1.1 \times 10^{-20} z^{2.52} T_e^{-0.76},$$
$$\Delta\alpha^r_{c1'}/\alpha^r_{c1'} \simeq \Delta\alpha^r_{ck}/\alpha^r_{ck} \,, \tag{B.22}$$

where the index k denotes the three P levels 2^3P_k (for argon, $w_k = 5,\ 3,\ 1$ for $k = 2, 1, 0$, respectively; for scandium, $w_k = 4.5,\ 3.6,\ 0.9$ for $k = 2, 1, 0$, respectively; Ref. [62]); $z = Z - 1$; T_e is in eV.

Dielectronic recombination The rate coefficients for the dielectronic recombination for all $n = 2$ levels of helium-like ions are taken from Ref. [23] and expressed in $m^3 s^{-1}$ as:

$$\alpha_{cm}^{d'} = 5.17 \times 10^{-20} Z^4 T_e^{-3/2} \left[\frac{9}{1 + 7 \times 10^{-5} Z^4} \exp(-6.80(Z + 0.5)^2 / T_e) \right.$$
$$\left. + \frac{27}{1 + 8 \times 10^{-5} Z^4} \exp(-8.78 Z^2 / T_e) + \frac{380(1 + p)^{-1}}{1 + 5 \times 10^{-3} Z^3} \exp(-10.2 Z^2 / T_e) \right] ,$$

$$\text{(B.23)}$$

$$\alpha_{cm'}^{d'} = 5.17 \times 10^{-20} Z^4 T_e^{-3/2} \left[\frac{3}{1 + 3 \times 10^{-6} Z^4} \exp(-6.80(Z + 0.5)^2 / T_e) \right.$$
$$\left. + \frac{0.5}{1 + 2.2 \times 10^{-5} Z^4} \exp(-8.78 Z^2 / T_e) + \frac{6.3}{1 + 5 \times 10^{-3} Z^3} \exp(-10.2 Z^2 / T_e) \right] ,$$

$$\text{(B.24)}$$

$$\alpha_{ck}^{d'} = 5.17 \times 10^{-20} (w_k/9) Z^4 T_e^{-3/2} \left[\frac{18}{9.5} \exp(-6.80(Z + 0.5)^2 / T_e) \right.$$
$$\left. + \frac{54}{1 + 1.9 \times 10^{-4} Z^4} \exp(-8.78 Z^2 / T_e) + \frac{380}{1 + 5 \times 10^{-3} Z^3} \frac{p}{1 + p} \exp(-10.2 Z^2 / T_e) \right] ,$$

$$\text{(B.25)}$$

$$\alpha_{cl'}^{d'} = 5.17 \times 10^{-20} Z^4 T_e^{-3/2} \left[\frac{12}{1 + 6 \times 10^{-6} Z^4} \exp(-6.80(Z + 0.5)^2 / T_e) \right.$$
$$\left. + \frac{18}{1 + 3 \times 10^{-5} Z^4} \exp(-8.78 Z^2 / T_e) + \frac{69}{1 + 5 \times 10^{-3} Z^3} \exp(-10.2 Z^2 / T_e) \right] ,$$

$$\text{(B.26)}$$

where w_k is the statistical weight of the $2p$ triplet levels; and

$$p \simeq 2.0(Z - 1)^{0.6} T_e^{-0.3} . \qquad \text{(B.27)}$$

Appendix C

Calculation of the Fractional Abundance of Argon Ions Using Coronal Equilibrium

Coronal equilibrium assumes that all the upward transitions are collisional and all the downward transitions are radiative. This describes the condition in the center of the tokamak plasma well. For argon (z=18), in the electron temperature region of interest (a few hundred eV to several keV), the argon ions are predominantly in the form of fully-striped, hydrogen-like, helium-like and lithium-like (as will be proven later in this chapter.) So it is assumed that the lowest ionization stage is Ar^{13+}. For an ionization equilibrium, i.e. the fractional abundance do not vary with time, a set of equations can be written as:

$$n_{Ar^{18+}} n_e \alpha_{Ar^{18+}} = n_{Ar^{17+}} n_e S_{Ar^{17+}} \; , \tag{C.1}$$

$$n_{Ar^{17+}} n_e \alpha_{Ar^{17+}} + n_{Ar^{17+}} n_e S_{Ar^{17+}} = n_{Ar^{18+}} n_e \alpha_{Ar^{18+}} + n_{Ar^{16+}} n_e S_{Ar^{16+}} \; , \tag{C.2}$$

$$n_{Ar^{16+}} n_e \alpha_{Ar^{16+}} + n_{Ar^{16+}} n_e S_{Ar^{16+}} = n_{Ar^{17+}} n_e \alpha_{Ar^{17+}} + n_{Ar^{15+}} n_e S_{Ar^{15+}} \; , \tag{C.3}$$

$$n_{Ar^{15+}} n_e \alpha_{Ar^{15+}} + n_{Ar^{15+}} n_e S_{Ar^{15+}} = n_{Ar^{16+}} n_e \alpha_{Ar^{16+}} + n_{Ar^{14+}} n_e S_{Ar^{14+}} \ , \qquad \text{(C.4)}$$

$$n_{Ar^{14+}} n_e \alpha_{Ar^{14+}} + n_{Ar^{14+}} n_e S_{Ar^{14+}} = n_{Ar^{15+}} n_e \alpha_{Ar^{15+}} + n_{Ar^{13+}} n_e S_{Ar^{13+}} \ , \qquad \text{(C.5)}$$

$$n_{Ar^{13+}} n_e S_{Ar^{13+}} = n_{Ar^{14+}} n_e \alpha_{Ar^{14+}} n_{Ar^{13+}} + n_{Ar^{14+}} + n_{Ar^{15+}} + n_{Ar^{16+}} + n_{Ar^{17+}} + n_{Ar^{18+}} = n_{Ar} \ ,$$
$$\text{(C.6)}$$

where $n_{Ar^{z+}}$ denotes the density of Ar^{z+}, n_{Ar} denotes the total argon density, $\alpha_{Ar^{z+}}$ denotes the recombination rate coefficient from Ar^{z+} to $Ar^{(x-1)+}$, $S_{Ar^{z+}}$ denotes the collisional ionization rate coefficient of Ar^{z+}.

This set of equations can be solved to give the fractional abundance of argon ions in various ionization stages.

$$\frac{n_{Ar^{18+}}}{n_{Ar}} = \frac{1}{C} \ , \qquad \text{(C.7)}$$

$$\frac{n_{Ar^{17+}}}{n_{Ar}} = \frac{\frac{\alpha_{Ar^{18+}}}{S_{Ar^{17+}}}}{C} \ , \qquad \text{(C.8)}$$

$$\frac{n_{Ar^{16+}}}{n_{Ar}} = \frac{\frac{\alpha_{Ar^{17+}} \alpha_{Ar^{18+}}}{S_{Ar^{16+}} S_{Ar^{17+}}}}{C} \ , \qquad \text{(C.9)}$$

$$\frac{n_{Ar^{15+}}}{n_{Ar}} = \frac{\frac{\alpha_{Ar^{16+}} \alpha_{Ar^{17+}} \alpha_{Ar^{18+}}}{S_{Ar^{15+}} S_{Ar^{16+}} S_{Ar^{17+}}}}{C} \ , \qquad \text{(C.10)}$$

$$\frac{n_{Ar^{14+}}}{n_{Ar}} = \frac{\frac{\alpha_{Ar^{15+}} \alpha_{Ar^{16+}} \alpha_{Ar^{17+}} \alpha_{Ar^{18+}}}{S_{Ar^{14+}} S_{Ar^{15+}} S_{Ar^{16+}} S_{Ar^{17+}}}}{C} \ , \qquad \text{(C.11)}$$

$$\frac{n_{Ar^{13+}}}{n_{Ar}} = \frac{\frac{\alpha_{Ar^{14+}} \alpha_{Ar^{15+}} \alpha_{Ar^{16+}} \alpha_{Ar^{17+}} \alpha_{Ar^{18+}}}{S_{Ar^{13+}} S_{Ar^{14+}} S_{Ar^{15+}} S_{Ar^{16+}} S_{Ar^{17+}}}}{C} \ , \qquad \text{(C.12)}$$

where the constant

$$C = 1 + \frac{\alpha_{Ar^{18+}}}{S_{Ar^{17+}}} + \frac{\alpha_{Ar^{17+}}\alpha_{Ar^{18+}}}{S_{Ar^{16+}}S_{Ar^{17+}}} + \frac{\alpha_{Ar^{16+}}\alpha_{Ar^{17+}}\alpha_{Ar^{18+}}}{S_{Ar^{15+}}S_{Ar^{16+}}S_{Ar^{17+}}} +$$
$$\frac{\alpha_{Ar^{15+}}\alpha_{Ar^{16+}}\alpha_{Ar^{17+}}\alpha_{Ar^{18+}}}{S_{Ar^{14+}}S_{Ar^{15+}}S_{Ar^{16+}}S_{Ar^{17+}}} + \frac{\alpha_{Ar^{14+}}\alpha_{Ar^{15+}}\alpha_{Ar^{16+}}\alpha_{Ar^{17+}}\alpha_{Ar^{18+}}}{S_{Ar^{13+}}S_{Ar^{14+}}S_{Ar^{15+}}S_{Ar^{16+}}S_{Ar^{17+}}} \ . \qquad (C.13)$$

Ionization rates

The rate coefficients for ionization by electron impact are given by ([63]):

$$S_{Ar^{z+}} = 3.01 \times 10^{-12} \zeta_z \chi_z E_1(x_z) \ m^3 s^{-1} \ , \qquad (C.14)$$

where χ_z is the ionization energy of the ground state of the x times ionized atom given by:

$$\chi_z = 13.6 n_z^{-2}(Z - a_i)^2 \ eV \ , \qquad (C.15)$$

where Z is the atomic number, $Z = 18$ in the case of argon, $i = Z - x$ is the number of electrons left, a_i is the effective screening number, ζ_z is the total number of electrons in the outer shell with principal quantum number, n_z. Further,

$$x_z = \chi_z/T_e = 13.6 n_z^{-2}(Z - a_i)^2 T_e^{-1} \ , \qquad (C.16)$$

where T_e is the electron temperature in eV. And the exponential integral $E_1(x) = \int_1^\infty z^{-1} e^{-xz} dz$ can be approximated very well by:

$$E_1(x) = e^{-x} f(x) \ , \qquad (C.17)$$

with

$$f(x) = \ln(\frac{x+1}{x}) - \{0.36 + 0.03(x + 0.01)^a\}(x+1)^{-2} \ , \qquad (C.18)$$

where $a = 0.5 \ (x \geq 1)$ or $a = -0.5 \ (x < 1)$. Numerical values for a_i, ζ_z and n_z taken from Table 1 in Ref. [23] are listed in Table C.1 for argon. Scandium data can be interpolated from data given in Table 1 of Ref. [23] and are also listed in Table C.1.

166

		i	1	2	3	4	5	
		ζ_z	1	2	1	2	3	
Element	$Z = z + i$	n_z	1	1	2	2	2	
			$-a_1$	a_2	a_3	a_4	a_5	a_6
Ar	18		0.040	0.593	1.568	2.139	2.908	0.801
Sc	21		0.063	0.573	1.543	2.115	2.881	0.781

Table C.1: Screening numbers a_i for ionization.

Recombination rates

The total recombination rate coefficients α_z is the sum of the radiative recombination rate α_z^r and the dielectronic recombination rate α_z^d:

$$\alpha_z = \alpha_z^r + \alpha_z^d \ . \tag{C.19}$$

The rate coefficients for radiative recombinations towards a hydrogen-like ($z = Z \rightarrow z = Z - 1$) or a helium-like ion ($z = Z - 1 \rightarrow z = Z - 2$) were given by Ref. [64] as:

$$\alpha_z^r = 3.86 \times 10^{-19} z^{2.4} T_e^{-0.7} \ m^3 s^{-1} \ , \tag{C.20}$$

where T_e is in eV. For $z = Z - 2, Z - 3, Z - 4$ the formula was given by Ref. [65] as:

$$\alpha_z^r = 1.92 \times 10^{-19} T_e^{-1/2} z^2 x_{z-1} f(x_{z-1}) g_{z-1} n_{z-1}^{-1} \ m^3 s^{-1} \ , \tag{C.21}$$

where x_{z-1} is defined by Equation C.16, n_{z-1} is the principal quantum number of the outer shell of the recombined ion ($z - 1$), $f(x_{z-1})$ is given by Equation 3.22, g_{z-1} is a numerical factor accounting for the recombinations to excited levels. g_{z-1} can be approximated by:

$$g_{z-1} \approx 1 + 0.37 n_{z-1} + 0.25 x_{z-1}^{0.43} n_{z-1}^{1.36} \ . \tag{C.22}$$

The dielectronic recombination coefficients α_Z^d and α_{Z-5}^d are $\equiv 0$. ([23]) The rate coefficients for other ionization stages are given by Ref. [23]:

$$\alpha_z^d = 8.00 \times 10^{-16} T_e^{-3/2} \sum_{i=1,2} \alpha_i Z^{\beta_i} \exp(-0.862 \gamma_i z^{\delta_i} / T_e) \ m^3 s^{-1} \ ,$$

z	α_1	β_1	γ_1	δ_1	α_2	β_2	γ_2	δ_2
$Z-1$	0.32	2.183	35	1.652	0.82	2.272	30	1.643
$Z-2$	10.5	0.963	45	1.584	16	1.216	37	1.591
$Z-3$	0.8(Ar) 0.36(Sc)	2.362	6.8	1.625	1.5	1.03	3.5	0.795
$Z-4$	6(Ar) 1.8(Sc)	1.807	7.8	1.597	5.8	0.975	8.7	0.685

Table C.2: Dielectronic recombination rate parameters

where the parameters: α_i, β_i, γ_i and δ_i for argon and scandium are given in Table C.2.

The fractional abundance of argon ions densities can be calculated using the rate coefficients given above. Figure C-1 plots the fractional abundance of argon ions as functions of electron temperature. It shows that argon is predominantly in the four highest ionization stages at temperature above 500 eV. This validates ignoring the ion population with ionization level lower than 13+ in calculating the fractional abundance of argon ions.
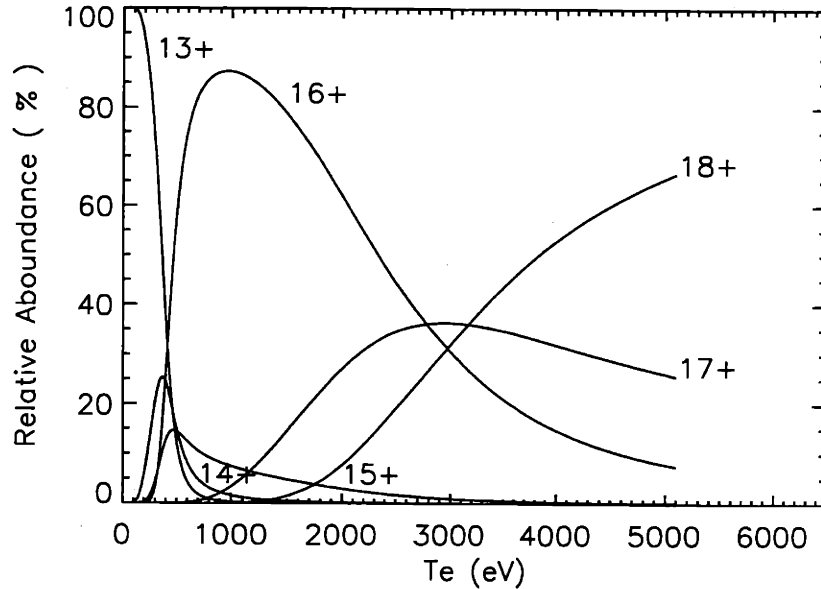

Figure C-1: Fractional abundance of argon ions in various ionization stages versus electron temperature; Coronal equilibrium assumed for the calculation.

Appendix D

Testing of the simple model

Experimental data have been used to test the validity of the simple impurity density model developed in Section 4.2.2. Equation 4.6 can be simplified by using:

$$\Phi_{in}(a) = \frac{1}{4}\frac{N}{V_{tot} - V_p}v_0 A_p \ . \tag{D.1}$$

The reason for such simplification is that good edge T_e and n_e profiles are hard to obtain, while T_e and n_e values at the LCFS is relatively easy to obtain. Using Equation D.1, Equation 4.13 can be simplified to:

$$n_{imp}(a) = \frac{1}{4}\frac{N}{(V_{tot} - V_p)D_\perp}\frac{v_0^2}{\overline{\sigma v_i}(a)n_e(a)}e^{-\frac{\lambda_n \overline{\sigma v_i}(a)n_e(a)}{v_0}} \ . \tag{D.2}$$

It is noticed that, with little modification, Equation D.2 can also be applied to majority ion species, which is usually deuterium in the case of Alcator C-Mod. Equation D.3 is the formula for deuterium density in the plasma:

$$n_D(a) = \frac{1}{4}\frac{n_D^{neutral}}{D_\perp}\frac{v_0^2}{\overline{\sigma v_i}(a)n_e(a)}e^{-\frac{\lambda_n \overline{\sigma v_i}(a)n_e(a)}{v_0}} \ , \tag{D.3}$$

where $n_D^{neutral}$ is the neutral deuterium density outside of the plasma; $D_\perp$ may be different for deuterium than for impurities.

The following test was done to verify the validity of the model. First, a group of shots, during which argon was injected and the edge parameters were measured with the fast scanning probe, was selected. The T_e and n_e at the LCFS were used in the

simple model to calculate the argon density in the plasma. The argon neutral gas temperature was adjusted to equate the predicted argon density to the experimentally observed density obtained by HIREX data. It turned out that the argon temperature is an order of magnitude higher than the wall temperature. It was then assumed that argon neutrals are in thermal equilibrium with the neutral deuterium gas outside of the plasma. So the deuterium gas had the same temperature as the neutral argon gas. The value of $n_D^{neutral}$ was measured on the mid-plane of the tokamak by a neutral gauge ([66]). The gauge actually measured the pressure of the gas but the result was given in the form of density with the assumption that the neutral gas was in thermal equilibrium with the machine walls, i.e. the gas temperature was around $300°$ K. The gauge was located somewhat remotely so the neutral gas in the gauge was in thermal equilibrium with the wall. But because the pressure is balanced for the neutral gas, the same pressure existed near the LCFS where the temperature of the neutral gas was an order of magnitude higher than the wall temperature. Thus the actual neutral density was an order of magnitude lower than that indicated by the neutral gauge.

D.1   The Argon Temperature Determination

Evidence suggested that it was not possible for the neutral argon gas outside of the plasma to be in thermal equilibrium with the machine walls. Figure D-1 plots argon penetration versus the argon gas temperature, according to Equation 4.14, for a set of typical plasma parameters. It shows that the argon penetration becomes comparable to the observed value only after the argon temperature is above $1000°$ K. Calculations using the same plasma parameter set gave $p = 6.5 \times 10^{-7}$ for an argon temperature of $300°$ K, five orders of magnitude lower than the typical observed value, which is around a few percent. Although p also depends strongly on the values of both $n_e(a)$ and $T_e(a)$, changes to $n_e(a)$ and $T_e(a)$ within the normal operation range cannot make the calculated p value agree with the observed ones. Therefore we conclude that the argon temperature is above the wall temperature, in the 10^3 $°$ K range, or a few tenths of an eV.
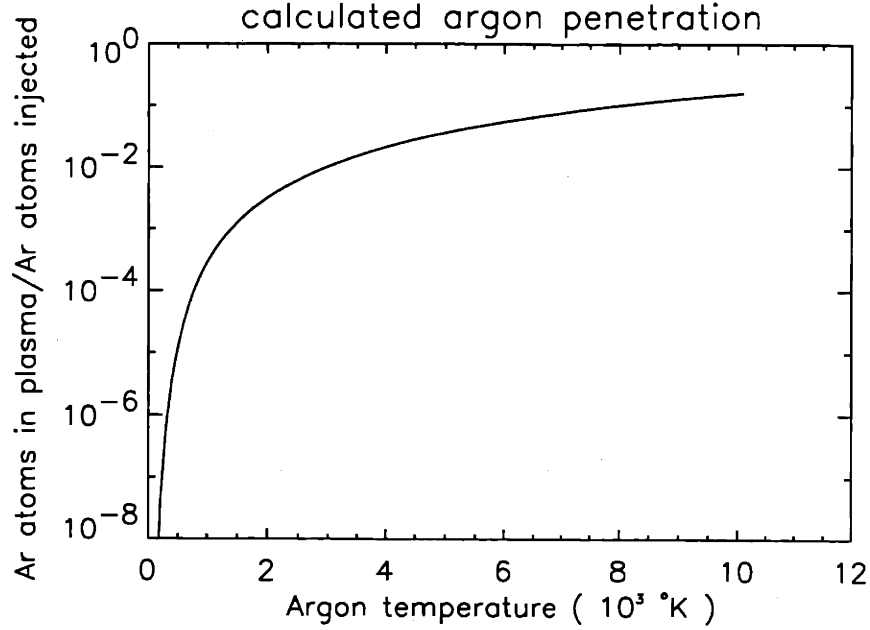
170

Figure D-1: Argon penetration calculated using Eq. D.2 vs. neutral argon temperature; $T_e(a) = 40\ eV$; $n_e(a) = 4 \times 10^{19}\ m^{-3}$; $D_\perp = 0.5\ m^2 s^{-1}$; $\lambda_n = 0.005\ m$.

Figure D-2 plots the neutral argon temperature deduced from T_e and n_e at the LCFS measured by the fast scanning probe for shots during Alcator C-Mod run 950426 and 950519 versus the n_e at the LCFS. There was no obvious dependance of neutral argon temperature on n_e at the LCFS. And as predicted, the neutral argon temperature was within the range of $10^3\ ^\circ K$.

The implication that the neutral argon temperature is at least one order of magnitude higher than the wall temperature is in contradiction with the intuitive belief that the neutral gas, in close contact with the wall, should also be in thermal equilibrium with it. The question then becomes, what heats the neutral argon gas? One possibility is that the neutral particles collide with the plasma ions in the SOL and gain energy from the collision. Another possibility is that when the argon atoms ionized in the SOL and the argon ions diffusing out of the plasma are swept by the frictional force along with the fuel ions into the limiter or divertor target plate and recombine into neutrals, they don't lose all their kinetic energy during the recombination process. It is reasonable to assume that argon ions within the SOL have kinetic energy of the same temperature as the edge electron temperature, which is of
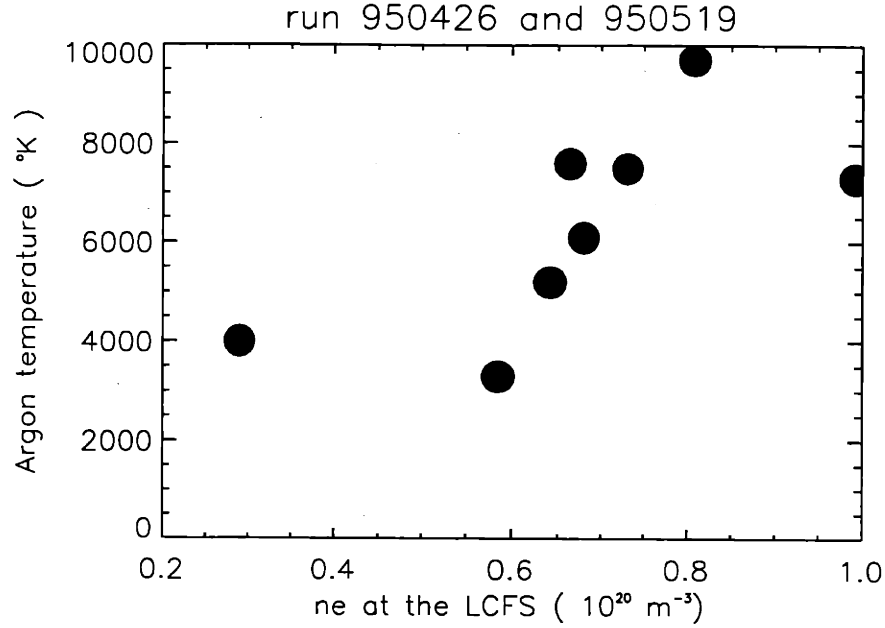
Figure D-2: Neutral argon gas temperature versus n_e at the LCFS for shots from Alcator C-Mod runs 950426 and 950519. $D_\perp = 0.5\,m^2s^{-1}$, $\lambda_n = 0.005\,m$.

the order of magnitude of tens of eVs. The neutral argon temperature is found to be $0.01\,eV - 0.1\,eV$. It's quite possible that the argon ions retain around 1% of their kinetic energy after the recombination.

D.2 Deuterium Density Prediction

With the assumption that the neutral deuterium gas is in thermal equilibrium with the neutral argon gas, the edge deuterium density is readily obtainable from the measurement of neutral deuterium density by a neutral gauge mounted on J-port (Ref. [66]) of Alcator C-Mod . A crude assumption is made that the edge deuterium density is the same as the $\bar{n}_e$. Figure D-3 plots the ratio between the $\bar{n}_e$ predicted by the above model and the measured $\bar{n}_e$, versus $\bar{n}_e$. The predicted average electron densities $\bar{n}_e^{predicted}$ were of the same order of magnitude as the measured average electron densities. Recall that the deuterium density and hence the $\bar{n}_e$ depend strongly on the edge n_e, T_e (with exponential dependence) and the neutral deuterium temperature. Small deviations in edge n_e, T_e or the neutral deuterium temperature could

cause several order of magnitude of change in the predicted $\bar{n}_e$. Thus it was not a coincidence that $\bar{n}_e$ predicted by the simple 1-D model turns out to be the same order of magnitude as the measured $\bar{n}_e$. It suggested that the most important parameters and processes involved in the problem of impurity screening/penetration were accounted for correctly in this model and the model represented, at least qualitatively, the correct relationships between these parameters.
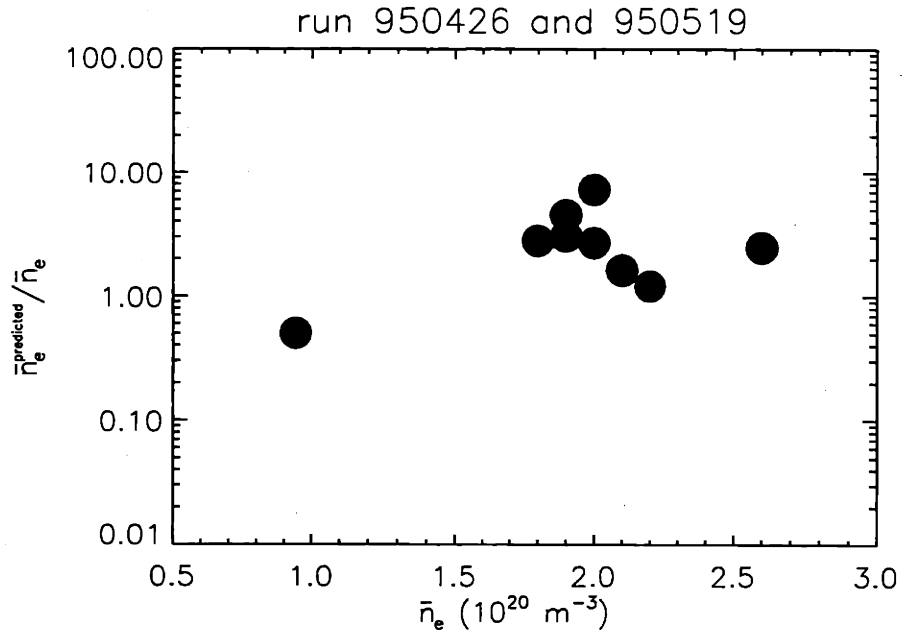

Figure D-3: $\bar{n}_e^{predicted}/\bar{n}_e$ versus $\bar{n}_e$ for Alcator C-Mod run 950426 and 950519. $D_\perp = 0.2\ m^2s^{-1}; \lambda_n = 0.005\ m$.
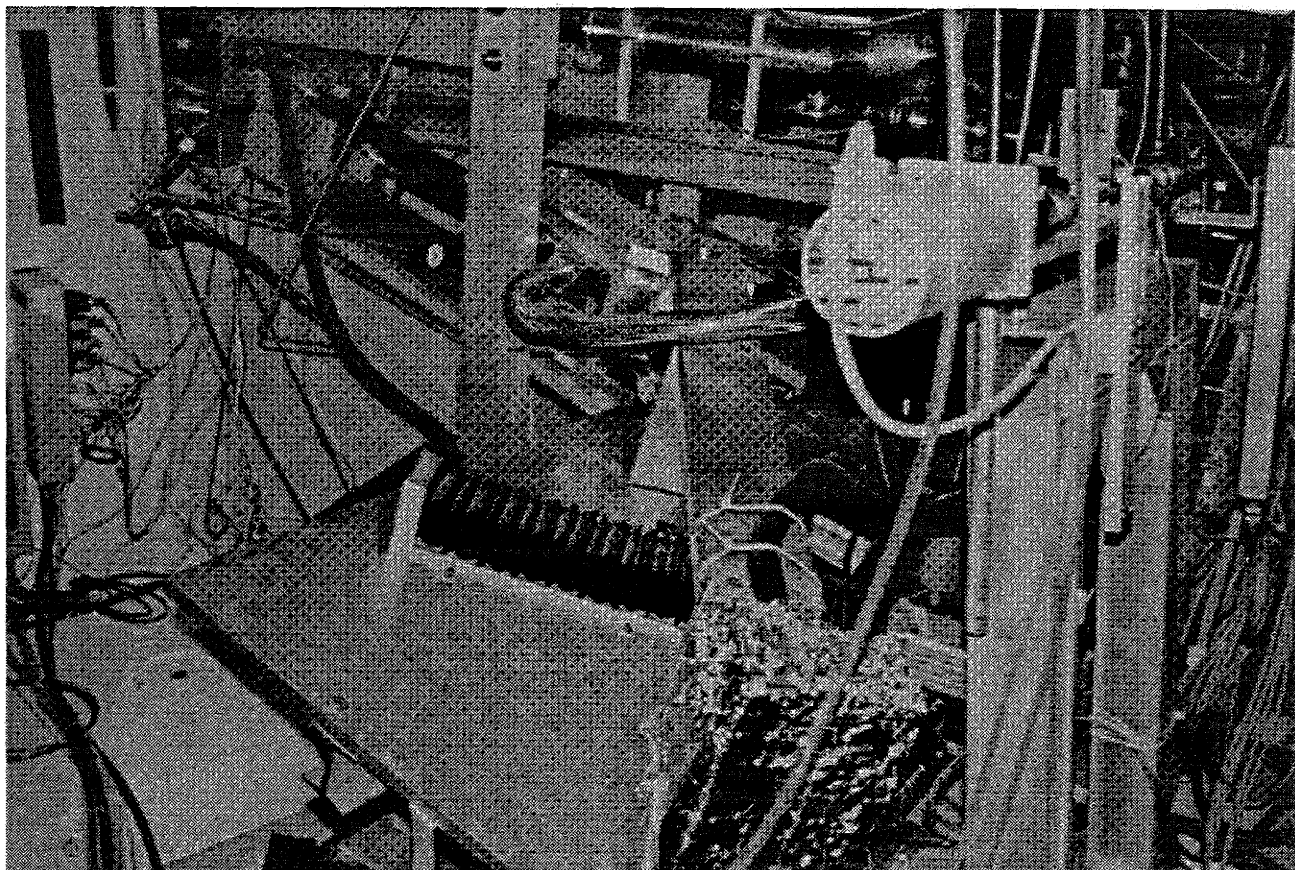
Appendix E

Pictures of HIREX

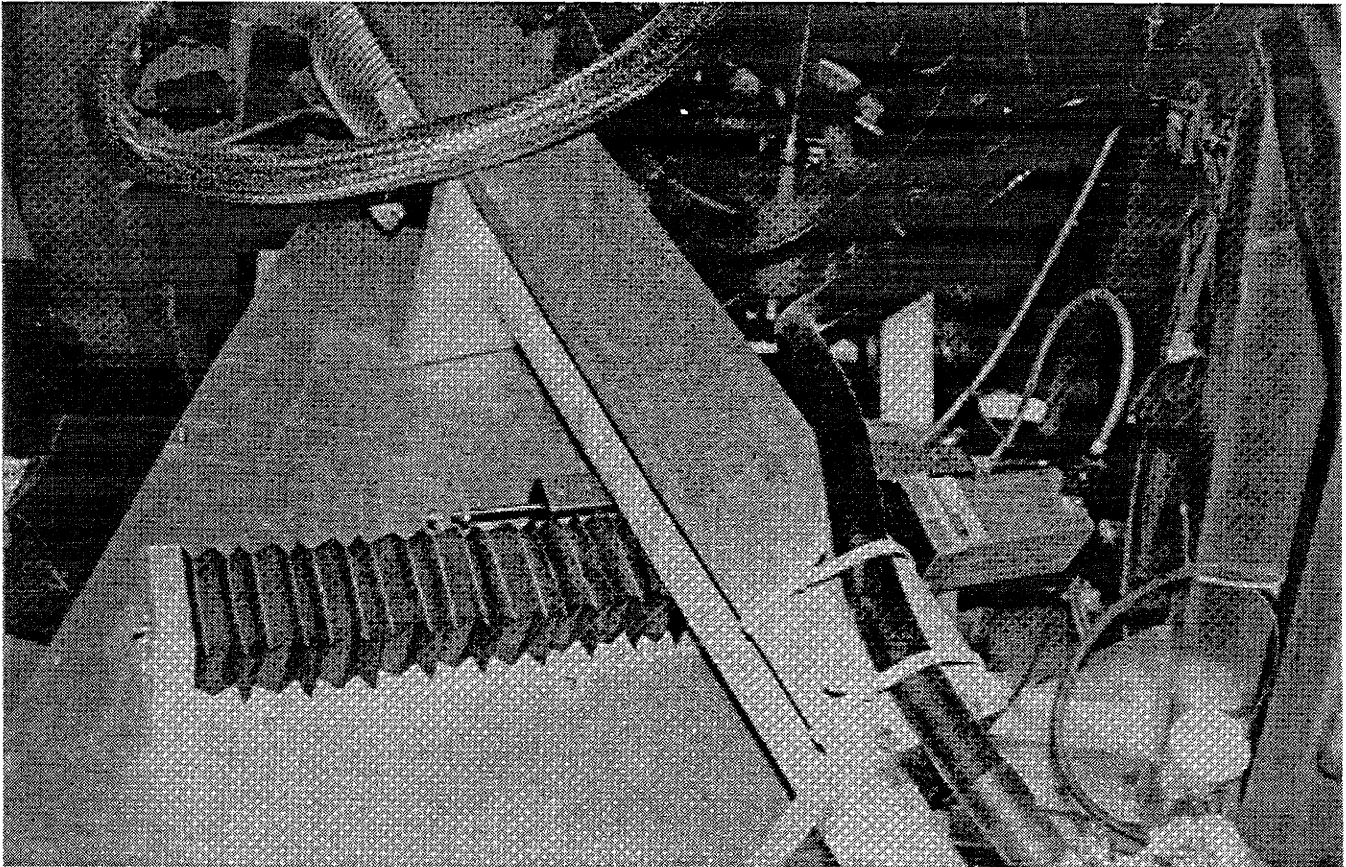Figure E-1: An individual spectrometer.

Figure E-2: Close view of the wavelength scanning mechanism of spectrometer #4. In the upper left corner is the bellow. The exit arm of the spectrometer is visible under the metal strip going from the upper left corner to the lower right corner. Horizontally in the middle of the picture is the lead screw used to drive the spectrometer and the stepper motor is at its right end. In the lower right corner, stripped onto the metal strip is the metal conduit through which the cables to the detector go.

Bibliography

[1] J. D. Lawson, Proc. Phys. Soc. **B 70**, 6 (1957)

[2] M. Greenwald et al Physc. Rev. Lett. , **53**, 352 (1984)

[3] H. L. Manning, Technical Report PFC/RR-86-14, Plasma Fusion Center, 1986

[4] R. V. Jensen, D. E. Post, W. H. Grasberger, et al., Nucl. Fusion **17**, 1187 (1977)

[5] P. H. Rebut, M. Brusati, Plasma Phys. Controll. Fusion **28**, 113 (1986)

[6] D. E. Roberts, Nucl. Fusion **23**, 311 (1983)

[7] T. Hirayama, H. Shirai, K. Shimizu, et al., J. Nucl. Mater. **145-147**, 854 (1987)

[8] F. Troyan, R. Gruber, H. Saurenmann, et al., Plasma Phys. Controll. Fusion **26**, 209 (1984)

[9] J. Rice, E. Marmar, E. Källne, and J. Källne, Phys. Rev. A **35**, 3033 (1987)

[10] F. Wagner, G. Becker, K. Behringer et al., Phys. Rev. Let. **49**, 1408 (1982)

[11] I. H. Hutchinson et al, Technical Report PFC/RR-88-11, Plasma Fusion Center, 1988

[12] L.L. Lao et al, Nucl. Fusion **25**, 1611 (1985)

[13] T. C. Hsu et al. , Proc. 8th Joint Workshop on ECE and ECRH IPP III/186, 409 (1993)

[14] J. H. Irby et al. , Rev. Sci. Instrum. **59**, 1568 (1988).

[15] B. Labombard et al, Rev. Sci. Instru.

[16] J. Rice et. al., Rev. Sci. Instrum. ,**66**(1), 752 (1995).

[17] von Hámos, Annalen der Physik, **5**. Folge, Band 17, 716 (1933)

[18] E. Källne, J. Källne, L. G. Atencio, J. Chmielewski, G. Idzorek and C. L. Morris, Rev. Sci. Instrum. **58**, 1077 (1987)

[19] Product sold by EG&G Reticon, Salem, MA 01742

[20] M. Graf, PhD thesis, Massachusetts Institute of Technology, 1995

[21] J. Urbahn, PhD thesis, Massachusetts Institute of Technology, 1994

[22] S. Cohen, J. Cecchi, and E. Marmar, Phys. Rev. Let. **35**, 1507 (1975)

[23] R. Mewe, and J. Schrijver, Astron. Astrophys. **65**, 99 (1978)

[24] R. K. Janev, Phys. Rev. A **28**, 1293 (1983)

[25] TFR Group and F. Bombarda, Phys. Rev. A **32**, 2374 (1985)

[26] F. Bely-Dubau, J. Dubau, P. Faucher, Mon. Not. R. Astr. Soc. **201**, 1155 (1982)

[27] L. A. Vainshtein and U. I. Safronova, Atom. Data and Nucl. Data Tables Vol. **21**, 49 (1978)

[28] R. A. Hulse, Nucl. Tech. /Fus. **3**, 259 (1983)

[29] D. G. Whyte et al, In *Bulletin of the American Physical Society*, (1994)

[30] G. M. McCracken et al, Nucl. Fusion **33**, 1409 (1993)

[31] R. Wood et al, In *Bulletin of the American Physical Society*, (1995)

[32] G. M. McCracken, P. C. Stangeby, Plasma Phys. Controll. Fusion **27**, 1411 (1985)

[33] J. Terry, private communication

[34] J.S. Bakos, I.B. Foldes, P.N. Ignacz and G. Kocsis, J. Appl. Phys. **69** (3), 1231 (1991)

[35] I. H. Hutchinson, Principles of Plasma Diagnostics, Press Syndicate of the University of Cambridge.

[36] P. Stek, private communication

[37] P. O'Shea, private communication

[38] B. C. Stratton, A. T. Ramsey, F. P. Boody et al., Nucl. Fusion **27**, 1147 (1987)

[39] A. Hubbard, private communication

[40] S. L. Milora, W. A. Houlberg, L. L. Lengyel, V. Mertens, Nucl. Fusion **35**, 657 (1995)

[41] E. J. Synakowski et al., Nucl. Fusion **29**, 311 (1989)

[42] G. Fussmann et al., in Pellet Injection and Toroidal Confinement (Proc. Tech. Comm. Mtg, Gut Ising, 1988), IAEA-TECDOC-534, IAEA, Vienna, 159 (1989)

[43] M. Greenwald et al., in Pellet Injection and Toroidal Confinement (Proc. Tech. Comm. Mtg, Gut Ising, 1988), IAEA-TECDOC-534, IAEA, Vienna, 153 (1989)

[44] R. Petrasso et al., Phys. Rev. Lett. **57**, 707 (1986)

[45] E. J. Synakowski et al., ibid., p. 181.

[46] K. Wenzel, D. Sigmar, Nucl. Fusion **30**, 1117 (1990)

[47] W. Feneberg et al., in Controlled Fusion and Plasma Physics (Proc. 14th Eur. Conf. Madrid, 1987), Vol. 11D, Part I, European Physical Society, Geneva, 339 (1987)

[48] R. Hulse et al., in Pellet Injection and Toroidal Confinement (Proc. Tech. Comm. Mtg, Gut Ising, 1988), IAEA-TECDOC-534, IAEA, Vienna, 99 (1989)

[49] K. Behringer et al., in Pellet Injection and Toroidal Confinement (Proc. Tech. Comm. Mtg, Gut Ising, 1988), IAEA-TECDOC-534, IAEA, Vienna, 167 (1989)

[50] E. Marmar, private communication

[51] M. Keilhacker, B. balet, J. Cordey et al., ibid., p. 231

[52] G. Becker, in Controlled Fusion and Plasma Heating (Proc. 15th Eur. Conf. Bubrovnik, 1988), Vol. 12B, Part I, European Physical Society (1988)211

[53] D. Pasini, R. Giannella, L. Lauro Taroni, et al., Plasma Phys. Controll. Fusion **34**, 677 (1992)

[54] M. Perry, N. Brooks, D. Content, R. Hulse, M. Mahdavi, H. Moos, Nucl. Fusion **31**, 1859 (1991)

[55] E. Holzhauer, et al., Plasma Phys. Controll. Fusion **36**, A3 (1994)

[56] ASDEX Team, Nucl. Fusion **29**, 1959 (1989)

[57] Y. Koide et al., Plasma Phys. Controll. Fusion **36**, A195 (1994)

[58] R. Hawryluk, S. Suchewer, S. Hirshman, Nucl. Fusion **19**, 607 (1979)

[59] K. Burrell et al., Plasma Phys. Controll. Fusion **34**, 1859 (1992)

[60] R. J. La Haye, T. Osborne, C. Rettig, C. Greenfield, A. Hyatt, J. Scoville, Nucl. Fusion, **35**, 988 (1995)

[61] M. Schaffer, DIIID, private communication

[62] R. Mewe, J. Schrijver, and J. Sylwester, Astron. Astrophys. **87**, 55 (1980).

[63] W. Lotz, Z. Phys. **232**,101 (1970)

[64] M. Seaton, Mon. Not. R. Astr. Soc. **119**, 1959 (1959)

[65] G. Elwert, Z. Naturforsch. **7a**, 432 (1952)

[66] A. Niemczewski, B. Lipschultz, B. LaBombard, G. M. McCracken, Rev. Sci. Instrum. **66**, 360 (1995)